Form from Function: Generalized Anisotropic Inverse Mechanics for Soft Tissues

A DISSERTATION
SUBMITTED TO THE FACULTY OF THE GRADUATE SCHOOL
OF THE UNIVERSITY OF MINNESOTA
BY

Ramesh Raghupathy

IN PARTIAL FULFILLMENT OF THE REQUIREMENTS
FOR THE DEGREE OF
DOCTORATE OF PHILOSOPHY

Victor H Barocas, Adviser

August 2011

Acknowledgments

First and foremost I would like to acknowledge the contribution of my parents. If not for their support, this academic journey would not have been possible. Their patience and encouragement provided much comfort in realizing that I was in the right path. My sister and her family have been equally important in supporting my decisions and have helped me each step of the way. I'm deeply thankful to my adviser, Professor Victor Barocas, for being the fantastic person that he is. I consider myself fortunate to have been his student. His infectious enthusiasm and passion for knowledge have made my time with him deeply enriching. He is both a friend and mentor whose experience, guidance and encouragement have been vital to my success as a researcher.

I would also like to thank my PhD committee members, Dr. Susan Mantell, Dr. Allison Hubel and Dr. Perry Leo for their valuable help and support. Dr. Mantell has been a wonderful mentor to me ever since I joined the Mechanical Engineering Department at University of Minnesota. Her support was critical in facilitating my joining the fabulous research group under Dr. Barocas. I'm also grateful to Dr. Subbiah Ramalingam who was another pillar of support for me. I've thoroughly enjoyed my experience as a teaching assistant for numerous courses under him. I also thank Dr. Narendra Simha, Dr. Barney Klamecki and Dr. Frank Kelso for the teaching opportunities under them. I consider my teaching experience to be a factor critical to my success. The many hours spent in helping students and clarifying their doubts have helped my critical thinking and problem solving skills. Many thanks go out to Dr. Henryk Stolarski for the numerous conversations we have had on finite element theory and for his passion in teaching the same. I thank the Departments of Mechanical and Biomedical Engineering for the financial assistance by way of research and teaching appointments.

I'm thankful to all the Barocas lab group members who have made my PhD experience very enjoyable. The camaraderie that our group shared, and support that we lent each other were instrumental in making research a fun experience. A special thanks to the members with whom I have worked the most: Colleen Witzenburg, Spencer Lake, Ed Sander, Julie Whitcomb, Tina Nagel, Maggie Thomas, Rouzbeh Amini, Sara Jouzdani, Ram Balachandran, Faisal Hadi, Victor Lai and Masano Sugiyama.

I also like to acknowledge my friends Kalyan Pamarthy and Vijay Subramanian for their support and the fun times we shared. Many other friends have provided much mirth and good times, and they are: Pradeep Mohan, Ragavendra Natarajan, Neeraj Mishra, Arvind Gururajan, Sudheer Raghavendran, Kailash Ramanathan, Ananth Sundareshwar and Venkat Raju.

Last but not the least, I thank the many gifted film composers whose music was a constant companion. In particular, I thank composers Ennio Morricone and Georges Delerue for their inspiring music, the former enthralling me with his creativity, and the latter with his gift for melody. Nothing in this world can be frustrating with their music around.

Abstract

Elastography, the imaging of soft tissues on the basis of elastic modulus has gained popularity in the last few decades and holds promise for application in many medical areas. Most of the attention has focused on heterogeneous materials that are locally isotropic, the intent being to detect a stiff tumor within a compliant tissue. Many tissues of mechanical interest, however, are anisotropic, so a method capable of determining material anisotropy would be attractive. This work presents a method, named GAIM (Generalized Anisotropic Inverse Mechanics), to determine the mechanical anisotropy of heterogeneous, anisotropic tissues, by directly solving the finite-element representation of the stress balance in the tissue. GAIM divides the sample into subdomains assumed to have uniform properties and determines the material constants in each subdomain. Use of a linear material model led to rapid computation with statistical confidence levels as performance metrics. Multiple tests, asymmetric loading and strain heterogeneity are needed to address the ill-posedness of the inverse problem, and represent a paradigm shift in the testing of soft tissues.

Simulated experiments of fibrous soft-tissues demonstrated the ability of the method to capture anisotropy qualitatively even though only a linear model is used. Results from the tests on soft-tissue analogs demonstrated the success in identifying regional differences in anisotropy based on full-field displacements and boundary forces obtained from multiple biaxial extension tests. The method's success in capturing regional anisotropic changes associated with growth and remodelling in fibroblast-populated cruciforms is a significant achievement, and holds promise for determining structural information of tissues from the mechanical response, since the structural and mechanical anisotropy are correlated. The linear GAIM model can be extended by a second step for nonlinearity with a fiber-based constitutive model. A closed-form solution for the latter was developed and provides rapid results for nonlinear regression. In summary, this work has built a novel exploratory tool to extract region-specific anisotropic properties on intact tissue samples. GAIM can be applied to provide information on the mechanical function of healthy tissue subjected to complex physiologic loads, identify regions within a tissue that exhibit irregular mechanical behavior (possibly due to disease or damage), and provide structural information from the mechanical function of tissues that are not amenable to structural tests.

Contents

List of Tables

List of Figures

Chapter 1

Introduction

1.1 Motivation for Research

Load-bearing tissues (e.g., ligament, heart valve leaflet) are dependent on their underlying structures for proper function. In fibrous soft tissues, the structural anisotropy of collagen fibers in the extracellular matrix is a major determinant of the tissue's mechanical response. When that structure is altered, as in disease or injury, the tissue's mechanical performance and functionality are diminished. Although the importance of microstructure in controlling tissue function is well known, how a tissue's precise composition and structure gives rise to its functionality, and how that functionality is affected by alterations in that structure from disease and damage, remain difficult questions to answer. Part of that difficulty lies in simultaneously characterizing a tissue's mechanical behavior and obtaining sufficient microstructural information. Both pieces of information are essential for understanding how regional variation in extracellular matrix composition and organization contributes to the coordinated response of the tissue to mechanical loads, and for analyzing the large variability in the response of tissues in terms of basic principles. Thus, a method to extract region-specific anisotropic material properties on intact tissue samples would afford several advantages:

- It could provide direct information on the mechanical function of healthy tissue subjected to complex physiologic loads, such as the supraspinatus tendon of the

rotator cuff [1].

- It could identify regions within a tissue that exhibit irregular mechanical behavior in comparison to healthy tissue, allowing more accurate assessment of the injury or disease state (similar to isotropic elastography for tumor detection, [2, 3]).
- Because of the relationship between structural and mechanical anisotropy (e.g., [4]), it could serve as a surrogate for structural measurement in tissues that are not amenable to standard structural tests.

In addition, many mechanically important tissues (e.g., heart valve leaflet [5, 6], facet capsule ligament [7], and rat ventricular wall [8]) are small enough that dissection and testing of different sections of the sample would be difficult if not impossible. Therefore, a technique to analyze tests on a larger specimen and extract complex mechanical information about its different regions would be extremely valuable. The class of problems relating to the extraction of material properties from the response to mechanical tests is termed as inverse mechanics, and is described in the next section.

1.2 Inverse Mechanics and Parameter Extraction

1.2.1 Forward and Inverse Problems, Well-Posed and Ill-Posed Problems

Classical physics definitions of forward and inverse problems are based on the cause-effect sequence and its reversal [9]. Forward problems are directed at computing the consequences of given causes; the corresponding inverse problem consists in finding the unknown causes of known consequences. Solution of the forward problem constitutes a transition from a physical quantity with a certain information content, to another with smaller information content. Hence, in transiting from cause to effect, there is a loss of information. Two other classifications based on mathematical qualities of uniqueness, existence and continuity are that of well-posed and ill-posed problems. A problem satisfying the properties of uniqueness, existence and continuity are called well-posed, and are typically motivated by physical reality. All problems that are not well-posed are said to be ill-posed. Because of the cause-effect sequence, forward problems are well-posed while inverse problems are ill-posed [9, 10].

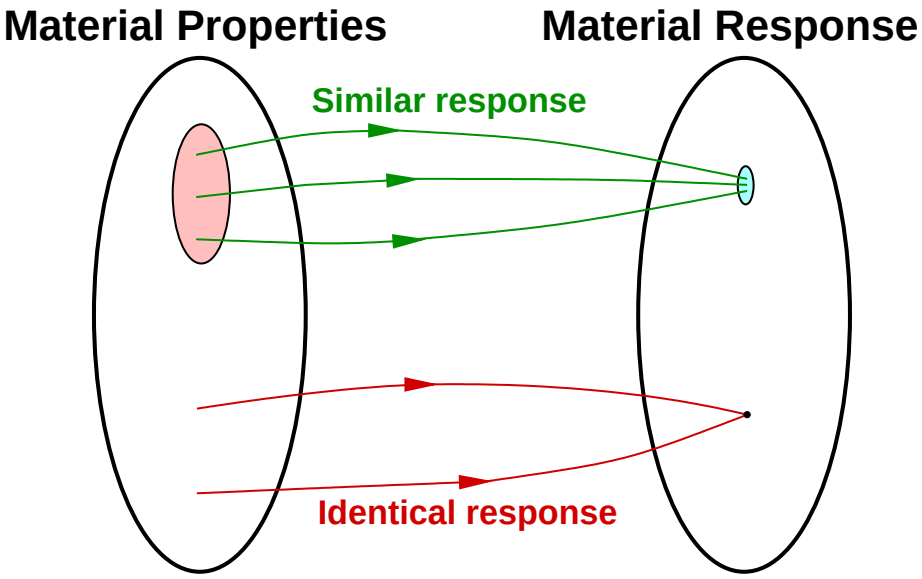

Figure 1.1: Representation of mapping relationship between material properties (cause) and material response (effect). The forward problem is the determination of material response from known material properties. The corresponding inverse problem is the determination of material properties from material response.

The relationship between forward and inverse problems in the context of material properties (cause) and material response (effect) is illustrated by the mapping in Fig. 1.1. Solution of the forward problem is the operator that maps the property to the response. While each material property set produces a single response, an identical response may be produced by a different property that is distant to the former in a metric-space as shown in the figure. Hence the mapping from response to properties is non-unique. Similar responses can also be produced by multiple objects which are distant from each other. Therefore the problem of determining the material properties from material response is ill-posed due to the intrinsic loss of information. System noise can lead to response that is outside the range of the operators on properties, thus representing non-existent or non-physical properties. In the solution of an inverse problem with noisy data, the true physical properties are not a solution to the problem but only an approximation. Therefore, the guideline for solving inverse problems is based on seeking approximate solutions which satisfy additional constraints of the physics. The provision of constraints is termed as regularization.

1.3 Literature Study

Elastography, the imaging of soft tissues on the basis of elastic modulus has been actively studied in the recent years (reviewed in [11]). Since cancerous tissue is stiffer than normal tissue, elastography affords the potential to identify a tumor within the surrounding healthy tissue. The primary goal of most elastographic studies to date has been the identification of high-stiffness, potentially cancerous regions within a tissue [12–15]. This inverse problem of estimating mechanical properties from imaging and displacement data holds promise for broad application in medical diagnosis and biomedical research.

While most of the focus has been in cancer detection, elastography has the potential to assess not just the stiffness but also the anisotropy of tissue. In load-bearing tissues like tendons and blood vessels, the underlying anisotropic structure of the tissue is distinctive and necessary for proper function. In diseased or damaged tissue, this structure is altered. Hence elastography affords the potential to be used as a tool to quantify relative changes not just in stiffness but also anisotropic properties such as degree and direction of alignment.

Depending on the type of imaging, inverse methods can be classified into two types-dynamic [16–18] and static [19–21]. In the dynamic method, a stimulus is applied to the tissue and the equations of motion are solved. In the static method, loads or displacements are applied and the force balance equations are solved.

Iding *et al.* [19] and Kavanagh & Clough [20] contain some of the earliest descriptions of the inversion method. Iding *et al.* used the inverse boundary value problem with experimental data to characterize the stress constitutive function for a nonlinear elastic solid. The domain was assumed to be homogeneous and incompressible. A Newton-Raphson method was used for the iterations. The displacement information was available only at certain discrete points, and it was found that the least squares solution using the known displacements was very sensitive to noise.

Kavanagh & Clough [20] outlined a number of strategies for identification of the anisotropic properties of a homogeneous solid. For the case of the stiffness matrix being a linear function of the material parameters, they obtained a direct solution

through the re-ordering of variables. An alternate form of solution was to express the material parameter matrix as a sum of linearly independent matrices thereby reducing the problem to that of determining the coefficients of those matrices iteratively. The latter was found to be more stable than directly solving for the material parameters. However, in order to guarantee convergence it was required that the initial guess was within 10% of the true value, or if the force matrix is not mostly zero. It was also found that by solving a largely over-determined problem, the effects of noise were reduced. The same work was extended in scope to nonlinear materials by using a constitutive equation that was a linear function of nonlinear invariants-based functions. Consideration of anisotropy, inhomogeneity and nonlinear constitutive models [22] further increase both the number of parameters to be optimized and the number of iterations to be performed, making this method computationally expensive. In these methods, the solution accuracy is often sensitive to the accuracy of the initial guess [16].

Newer imaging methods like ultrasound and dynamic MRI [23, 24] enable the full 3D reconstruction of displacement fields inside tissues from multiple slices of 2D displacement information, caused in response to harmonic excitations. The inversion of the resulting dynamic wave propagation problem to determine the constitutive parameters is complex, with recent advances reviewed by Park and Maniatty [25]. Most of approaches assume isotropy [13, 14, 26, 27], thus reducing the elastic tensor to two scalar constants of which the elastogram of the shear modulus is the most common. Sinkus *et al.* [17] expanded the scalar Young's modulus into a second order tensor with all identical components and inverted the resulting system to find the components of this tensor. Through the principal component analysis of this tensor a qualitative measure of anisotropy was obtained. A later work [24] included the consideration of transversely isotropic symmetry of the elastic tensor however the assumption of negligible gradients in the hydrostatic stress term is not valid in the case of heterogeneous materials (*cf.* [25]).

With most inverse mechanics methods being formulated as a least-squares global minimization problem, Van Houten [18] used the inversion on overlapping subdomains for MR elastography. A similar idea was used by Seshaiyer & Humphrey [28] for the static case with nonlinear constitutive behavior. While these methods are less intensive than the global minimization, they were sensitive to noise and depended on

the initial guess of parameters. In both cases, isotropy was assumed. In particular, Seshaiyer and Humphrey used the inversion for characterizing the hyperelastic behavior of membranes. They used sub-domains consisting of five non-coplanar nodes to match the number of equations with the number of unknowns to solve for. They reported that the relative error in the evaluated parameters increased drastically with experimental noise.

Liu *et al.* [23] have developed a 3D inversion algorithm for the full anisotropic constants in a heterogeneous medium from computed tomography data. They modeled the domain to be piece-wise homogeneous and consisting of interior sub-domains. They assumed that the displacement information was available at all domain boundaries (interior and exterior) and that force information was available at a part of the exterior boundary. Generally for a domain with boundary displacement given, the solution is non-unique unless some part of the stress at the boundary is given [29–31]. While they did not require the full-field displacements, they assumed that it was possible to accurately determine the subdomain boundaries and the displacements there. They reported that their method was sensitive to noise with identifying the boundaries.

Majority of the methods listed earlier are based on the iterative improvement of constitutive parameters by minimizing a merit function. Because the forward problem is solved repeatedly for improved parameters, these methods have the advantage of stability, unlike direct methods, which can be unstable due to their ill-posedness and increased sensitivity to noise. Despite the stability and convergence with iterative methods, they do not provide a measure to assess if the input data had enough information representative of all the phenomena being modeled by the choice of constitutive function. If some of the parameters being extracted were not sensitive to the input data, then multiple solutions may exist, and the final converged values are dependent on the initial guess and the optimization method.

Hence, there is still scope for a general method that determines the regional variation of anisotropic properties without *a priori* knowledge of the heterogeneity, while providing a measure of assessing if enough information was present to capture the pheneomenon that each parameter represents. In the next section we discuss the key

gap in capability and knowledge in the context of soft tissues.

1.4 Key Gap in Knowledge

Our focus in this study is on static methods. By far, the most common approach for static methods consists of four steps:

1. Assume a constitutive equation and distribution of constitutive parameters
2. Solve the forward problem and estimate the displacements that would occur for the known boundary conditions and assumed constitutive parameters
3. Compare the resulting solution to the experimental measurement
4. Return to step (2), repeating until a satisfactory result is obtained

This strategy has proven successful in many cases (summarized in [32, 33]), but it remains limited in scope. Specifically, there are three major improvements that can be made over the standard approach: (1) handling anisotropic media, (2) segmentation of a heterogeneous medium when the partitions are not known *a priori* , and (3) the potential for high computational cost for repeated forward solutions. These issues, along with various recent advances, are discussed in the subsequent paragraphs.

Anisotropy. Most elastographic methods assume isotropy [13, 14, 16], reducing the problem to two constants in the case of a linear elastic material [34]. If one's goal is to find a tumor, this simplification is justified. If, however, one's goal is to characterize load-bearing tissues (e.g., ligament, arterial wall, heart valve), then anisotropy must be considered. Few examples focus on anisotropy, and those either treat the material as homogeneous [35] or prescribe the locations of regions of different properties [17]. For example, Flynn *et al.* [35] estimated the tangent anisotropic properties for non-linear materials from biaxial tests with each sample assumed to be homogeneous, thus requiring samples from different locations for describing heterogeneity. Pedrigi *et al.* [36] used a heterogeneous, anisotropic model for human lens capsule, but the anisotropy was restricted quantifying the relative stiffnesses in circumferential and meridional directions for prespecified regions.

Heterogeneity. For materials with known segmentation, the problem of heterogeneity can be handled by assigning each unit different properties. For example, Girard *et al.* [37] segmented the posterior scleral shell into peripheral and peripapillary domains and evaluated anisotropic properties for them. Liu *et al.* [23] used segmentation boundary information from 3D computed tomography data, and identified anisotropic elastic moduli for each segment. In contrast, if the segmentation is not known *a priori* but isotropic linear elasticity is assumed, then the regions of high vs. low modulus can be found [38]. There is, to our knowledge, no scheme that determines heterogeneous anisotropic material parameters when the different regions cannot be prespecified. It is this gap that the present paper seeks to fill.

Speed and Accuracy. While there have been improvements in speed for iterative minimization schemes (see e.g., using local sub-domains [28, 39], using the adjoint method [40]), an additional factor to consider is that inverse problems can take very many forward iterations to solve. When the model is linear, the adjoint method can provide rapid solution [41]. Another issue is that since the inverse problem is often poorly posed [10], the results can be very sensitive to input data or initial guess [42]. A direct solution method could produce rapid results and could, via the theory of linear regression, provide an error estimate for linear models.

Chapter 2

Development of an Inverse Finite Element Model for Soft Tissues

This work was a part of the paper:

Generalized Anisotropic Inverse Mechanics for Soft Tissues
Journal of Biomechanical Engineering, 2010, 132(8)
Raghupathy, R. and Barocas, V.H.

2.1 Introduction

In this chapter we describe the inverse problem that will be solved and develop an inverse finite element framework to identify anisotropic tissue properties and their spatial variation. The spatial variation of properties is modeled by partitioning the sample domain into subdomains and identifying uniform properties for each subdomain. We will describe the algorithm for partitioning the domain and illustrate the how the partition shapes and sizes are determined. Tissue anisotropy variation is represented visually in the form of alignment maps. Various methods in the design of experiments and the subsequent analysis which will improve the parameter extraction are proposed. The model's sensitivity to noise is studied, and a method for assessing the performance of the model is identified. Lastly, we provide a description of all stages in the experimental testing, data processing and analysis, and visualization of results.

2.2 Model Formulation

Consider a body occupying domain Ω with boundary Γ and undergoing elastic deformation (Fig. 2.1). The static equilibrium equation for the body is

$$\sigma_{ij,j} = 0 \tag{2.1}$$

where σ is the Cauchy stress. The body is acted upon by displacement and traction boundary conditions defined by

$$\sigma_{ij}\, n_j = T_i \quad \text{on } \Gamma_t \tag{2.2}$$

$$u_i = g_i \quad \text{on } \Gamma_u \tag{2.3}$$

where g and T are the prescribed displacements and traction vector functions respectively, Γ_u and Γ_t are the complementary portions of the boundary ($\Gamma_u \cup \Gamma_t = \Gamma,\ \Gamma_u \cap \Gamma_t = \varnothing$), and n is the normal vector on boundary Γ_t. For a linear elastic material, the stress σ is related to the strain ε (with linearized strains $\varepsilon_{kl} = \frac{1}{2}(u_{k,l} + u_{l,k})$) by

$$\sigma_{ij} = C_{ijkl}\, \varepsilon_{kl} \tag{2.4}$$

where C is the fourth-order elasticity tensor.

The relevant forward and inverse problems that are of interest to us are stated as follows:

- The *forward problem* is to determine the displacement field u from the boundary conditions (Eqns. 2.2, 2.3), the material constitutive law (e.g., Eqn. 2.4), and the spatial variation of material properties.
- The corresponding *inverse problem* is to determine the form of the material constitutive law and the spatial variation of properties from the boundary conditions (Eqns. 2.2, 2.3) and the displacement u over the whole domain Ω.

The inverse problem applied to the complex tissues which were described in the previous section are challenging to solve due to the regional variation of anisotropic properties. While the determination of the appropriate form of the constitutive behavior

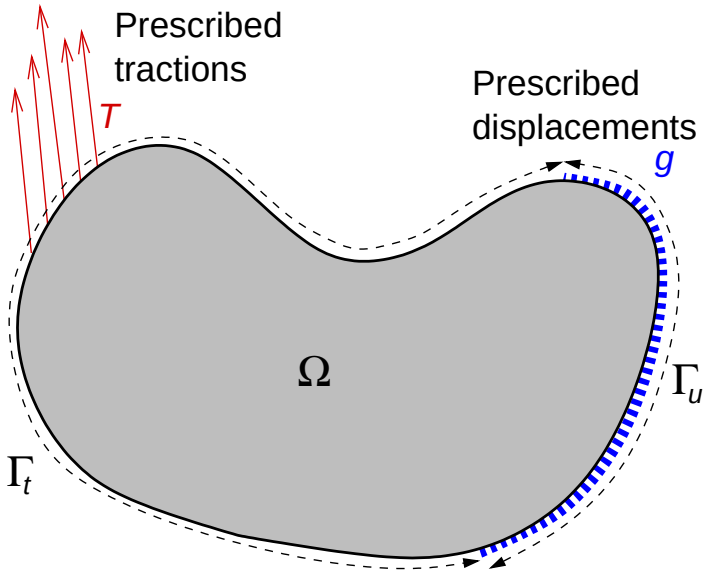

Figure 2.1: Schematic of a body occupying domain Ω and boundary Γ, acted upon by tractions (T) and displacements (g) on the respective parts of boundaries Γ_t and Γ_u.

is certainly invaluable for modeling the tissue response in complex environments, our focus is on identifying regional changes in tissue anisotropy and stiffness. Hence, we will make a simplification to the inverse problem by restricting the constitutive behavior to the simplest form that is sufficient to obtain a description of the regional variation in anisotropy and stiffness. We hypothesize that using the simplest form of anisotropic material constitutive behavior is sufficient to determine these regional changes. We will assume a linear elastic relationship (Eqn. 2.4) for the material behavior and determine all the anisotropic parameters for the elasticity tensor C. In the following subsections we briefly discuss the symmetry of the C tensor and develop the model to determine the C_{ijkl} parameters and identify regional changes in anisotopy and stiffness for the inverse problem.

2.2.1 The Elastic Tensor

The elastic tensor C is of fourth order with major symmetries (due to the quadratic form of the strain energy density) and minor symmetries (due to symmetry of stress and strain)

$$C_{ijkl} = C_{klij} = C_{jikl} = C_{ijlk} \tag{2.5}$$

Thus C has a maximum of 21 independent constants for the general case. In isotropic materials this reduces to the 2 independent Lame constants- λ and μ, which are related to C by

$$C_{ijkl} = \lambda\delta_{ij}\delta_{kl} + \mu(\delta_{ik}\delta_{jl} + \delta_{il}\delta_{jk}) \tag{2.6}$$

Instead of the Lame constants it is common to use two other independent constants- Young's modulus (E) and Poisson ratio (ν) which are related as

$$E = \frac{\mu(3\lambda + 2\mu)}{\lambda + \mu} \tag{2.7}$$

$$\nu = \frac{\lambda}{2(\lambda + \mu)} \tag{2.8}$$

2.2.2 Development of the Inverse Finite Element Matrix System

Using the Galerkin finite element method [43], the weak form of Eqn. (2.1) is

$$\int_\Omega \left(C_{ijkl}\varepsilon_{kl}\right)_{,j} w_i \, d\Omega = 0 \tag{2.9}$$

where w is the test function. Integrating by parts and applying the boundary conditions, we have

$$\int_\Omega C_{ijkl}\varepsilon_{kl}\, w_{i,j}\, d\Omega = \int_{\Gamma_u} C_{ijkl}\varepsilon_{kl}\, w_i\, n_j\, d\Gamma_u + \int_{\Gamma_t} w_i T_i \, d\Gamma_t \tag{2.10}$$

The displacements constraints on Γ_u lead to reaction forces R. We assume for now that R can be determined and discuss the case of unknown R subsequently.

$$\int_\Omega C_{ijkl}\varepsilon_{kl}\, w_{i,j}\, d\Omega = \int_{\Gamma_u} w_i R_i \, d\Gamma_u + \int_{\Gamma_t} w_i T_i \, d\Gamma_t \tag{2.11}$$

The two boundary integrals can be combined into one term

$$\int_\Omega C_{ijkl}\varepsilon_{kl}\, w_{i,j}\, d\Omega = \int_\Gamma w_i F_i \, d\Gamma \tag{2.12}$$

where F is the force on the boundary, and includes both traction and reaction forces. Using Galerkin basis functions N_A for the test functions, we obtain the finite element

discretized form as

$$\sum_e \left(\int_{\Omega^e} C_{ijkl}\varepsilon_{kl}\, N_{A,j}\, d\Omega^e \right) = \sum_e \left(\int_{\Gamma^e} N_A F_i\, d\Gamma^e \right) \tag{2.13}$$

where index A corresponds to the node in the finite element, and Σ denotes assembly over all elements. Equation 2.13 can be understood to be the force balance at node A in the direction corresponding to index i. We seek to estimate the components of the elasticity tensor C_{ijkl} and their variation over the domain Ω. If we assume that C_{ijkl} is constant over each element, then we can re-cast Eqn. (2.13) as a global linear matrix equation of the form

$$K\,\mathcal{C} = \mathcal{F} \tag{2.14}$$

where $\mathcal{C}$ is the column vector of C_{ijkl} parameters of all elements, $\mathcal{F}$ is the assembled column vector of nodal forces (tractions and reactions), and K is a matrix consisting of the terms that remain when the material parameter terms on the left hand side of Eqn. (2.13) are factored out. To illustrate this for the case of two dimensions, consider the integrand on the left hand side of Eqn. 2.13, which can be expanded for the choice of $i = 1, 2$ by using the major and minor symmetries as follows

$$\begin{aligned} C_{1jkl}\varepsilon_{kl}N_{A,j} &= C_{11kl}\varepsilon_{kl}N_{A,1} + C_{12kl}\varepsilon_{kl}N_{A,2} && (2.15)\\ &= C_{1111}\varepsilon_{11}N_{A,1} + C_{1122}\varepsilon_{22}N_{A,1} + C_{1112}(2\varepsilon_{12}N_{A,1} + \varepsilon_{11}N_{A,2}) \\ &\quad + C_{2212}\varepsilon_{22}N_{A,2} + 2C_{1212}\varepsilon_{12}N_{A,2} && (2.16) \end{aligned}$$

$$\begin{aligned} C_{2jkl}\varepsilon_{kl}N_{A,j} &= C_{21kl}\varepsilon_{kl}N_{A,1} + C_{22kl}\varepsilon_{kl}N_{A,2} && (2.17)\\ &= C_{1112}\varepsilon_{11}N_{A,1} + C_{2212}(\varepsilon_{22}N_{A,1} + 2\varepsilon_{12}N_{A,2}) + 2C_{1212}\varepsilon_{12}N_{A,1} \\ &\quad + C_{1122}\varepsilon_{11}N_{A,2} + C_{2222}\varepsilon_{22}N_{A,2} && (2.18) \end{aligned}$$

The values of C_{ijkl} for each element can be represented as a vector $\mathcal{C}^e$

$$\mathcal{C}^e = \begin{bmatrix} C_{1111} & C_{2222} & C_{1212} & C_{2212} & C_{1112} & C_{1122} \end{bmatrix}^T \tag{2.19}$$

The elemental K matrix, denoted by K^e, is given by

$$K^e = \left[\begin{array}{cccc} K_1^e & K_2^e & \cdots & K_{n_{en}}^e \end{array} \right]^T \tag{2.20}$$

where n_{en} is the number of nodes in each element. Each K_A^e matrix is the integral of k_A^e over the element and represents the contribution to node A, with k_A^e obtained from Eqns. 2.16 and 2.18 as

$$k_A^e = \left[\begin{array}{cccccc} N_{A,1}\varepsilon_1 & 0 & N_{A,2}\varepsilon_3 & N_{A,2}\varepsilon_2 & (N_{A,2}\varepsilon_1 + N_{A,1}\varepsilon_3) & N_{A,1}\varepsilon_2 \\ 0 & N_{A,2}\varepsilon_2 & N_{A,1}\varepsilon_3 & (N_{A,1}\varepsilon_2 + N_{A,2}\varepsilon_3) & N_{A,1}\varepsilon_1 & N_{A,2}\varepsilon_1 \end{array} \right]^T \tag{2.21}$$

It is to be noted that we have collapsed the strain terms into a vector ($\varepsilon_1 = \varepsilon_{11}$, $\varepsilon_2 = \varepsilon_{22}$, $\varepsilon_3 = 2\varepsilon_{12}$). The global matrix K and vector $\mathcal{C}$ in Eqn. 2.14 are obtained by the assembly of K^e matrix and $\mathcal{C}^e$ vectors over all elements respectively.

2.3 Solution of the Inverse Matrix System

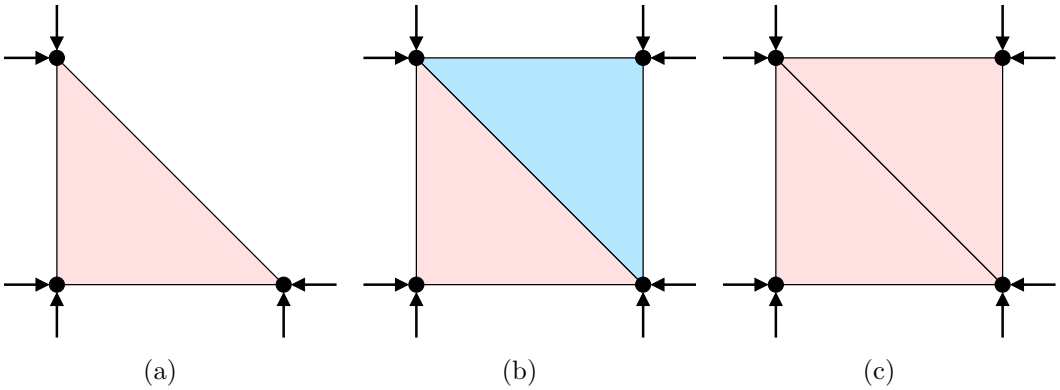

Figure 2.2: Requirement of sufficient equations to solve for unknown parameters (a) Single triangular element has 6 equations for 6 parameters and can be solved, (b) Two triangles of different materials have 8 equations for 12 parameters leading to an under-determined system, (c) If both triangles are assumed to be of the same material then the system is over-determined with 8 equations for 6 parameters.

The nodal force balance (Eqn 2.14) contributes one equation for each spatial dimension for every node. The need to construct a well-posed problem is illustrated by considering the case of a single constant strain triangle finite element (Fig. 2.2(a)).

The assumption of homogeneity yields 6 equations (2 per node $\times$ 3 nodes) for the 6 unknown anisotropy constants, which can be solved if all the nodal forces are known and if the K^e matrix is of full rank. If there are two triangle elements of two different materials (Fig. 2.2(b)) and sharing a common edge, then the system is under-determined with 12 unknown parameters (6 for each element) and 8 equations (2 per node). However, if one assumes that the two elements were of the same material (Fig. 2.2(c)), then an over-determined system results, with 8 equations for 6 unknown parameters. This observation motivates a method for solving the inverse problem by assuming that the sample domain is comprised of homogeneous subdomains. All mesh elements in each subdomain are assumed to have the same material parameters. The result is an over-determined linear system (Eqn. 2.14), which can be solved in a least-squares sense by the pseudo-inverse

$$\mathcal{C} = (K^T K)^{-1}(K^T \mathcal{F}) \tag{2.22}$$

Matrix K is of dimension (m, n), where m is the number of nodal equations (space dimension $\times$ number of nodes) and n is the total number of material parameters for all subdomains (6 $\times$ number of subdomains, for 2D). The over-determined system ($m > n$) has a solution as long as matrix K is of rank n. The evaluated parameters are accepted if the residual force norm is smaller than a pre-set tolerance:

$$\|\mathcal{F} - K\,\mathcal{C}\|_2 < tol \tag{2.23}$$

It was previously assumed that the distributed reaction forces at Γ_u are known. However, the force is not necessarily available on each node of Γ_u. For instance, in uniaxial and biaxial testing of soft tissues, the sample is usually loaded by pulling on sutures or clamps (Fig. 2.3). The force that is measured on each gripping arm is the total force in that region of Γ_u, and in the direction of pull. Hence we only know the integral of the normal component of the nodal forces (in the direction of pull). The corresponding nodal force equations are summed and added to the linear system of equations, and equations involving the individual forces are discarded.

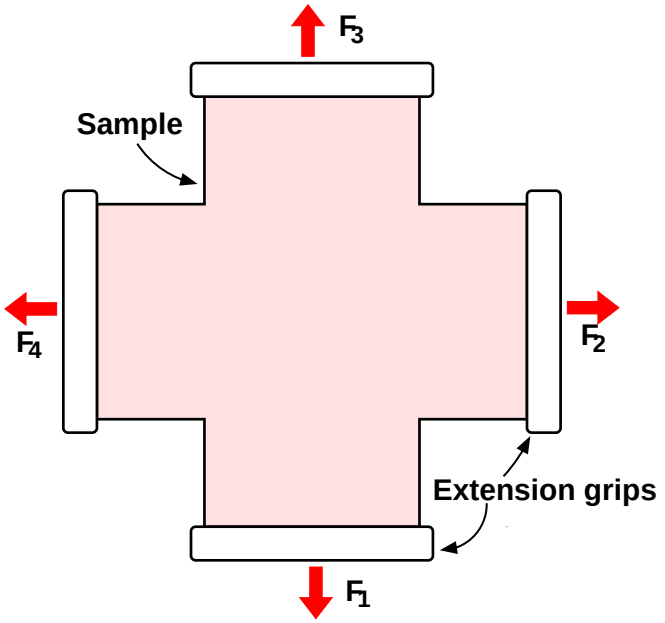

Figure 2.3: Sample is gripped in 4 arms and pulled. Force measured on each arm is the total force on that part of Γ_u in the direction of pull

2.3.1 Domain Partitioning

The parametric inversion described previously is straightforward to implement in the case of a homogeneous specimen, for which all elements have the same elastic constants. The general case however, is of heterogeneous materials in which the regions of material difference may or may not be known, or in which the properties may vary smoothly. If the regions of material difference are known beforehand, then one can partition the mesh accordingly into homogeneous subdomains [23, 37]. Since the equations of nodes at inter-partition boundaries get contributions from all partitions connected to it, the global system of equations is coupled with respect to the different materials. Without foreknowledge of material heterogeneity, we seek to identify the regions of uniform material elastic constants. In static tests, the boundary force information is usually known. Our approach starts at the sample boundary and solves the region near the grips assuming homogeneity. The solution is grown from the boundary to the interior by repeating this step on the unsolved domain that remains. Thus, domain partitioning can be determined dynamically by probing various choices of homogeneous subdomains from the boundary and advancing inwards.

The trial of numerous partition choices and subsequent mesh subdomain manipulation must be performed repeatedly with minimal computational cost. The calculation can be done efficiently by storing the mesh as a graph structure that allows rapid access of mesh entities (node, edge, element) adjacent to a given entity. A mesh data structure (Fig. 2.4) can be developed using `C++` classes for rapid adjacency operations.

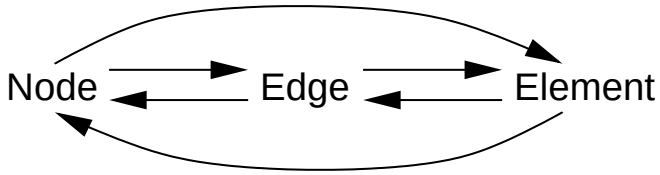

Figure 2.4: Graph structure storage of 2D mesh allows retrieval of adjacencies. The direction of arrows indicate adjacent mesh entitites that can be accessed from a given entity. For instance, given a mesh node, one can access the connected edges and elements; from the connected edges we can determine the neighboring nodes

We employ a three-step scheme outlined as follows:

Step 1: Solving the subdomains on the sample boundary

At regions of the sample boundary with traction or displacement boundary conditions the total applied normal force is known. Various choices of subdomains that enclose each region of applied boundary condition are tried until an acceptable solution for the elastic constants is found. Equations of nodes at subdomain boundaries are not solved if they are connected to unsolved elements outside of the region considered. To illustrate, for the bottom arm of the cruciform shown in Fig. 2.3, we can set up the initial partition shown as shaded elements in Fig. 2.5.

Step 2: Using resultant forces from solved subdomains to solve adjacent subdomains

Once the equations for a subdomain have been solved, the global domain is reduced by removing all the solved elements from the global mesh. The subdomain boundary nodes, whose equations were not solved in the previous step, now have resultant forces from the removal of solved elements. These boundary nodes are treated as pseudo-traction boundary conditions on the reduced domain (Fig. 2.6). Various choices of subdomains (see §2.3.2 for details) adjacent to the previously solved subdomains are tried until a solution is found. As in step 1, equations of subdomain boundary nodes

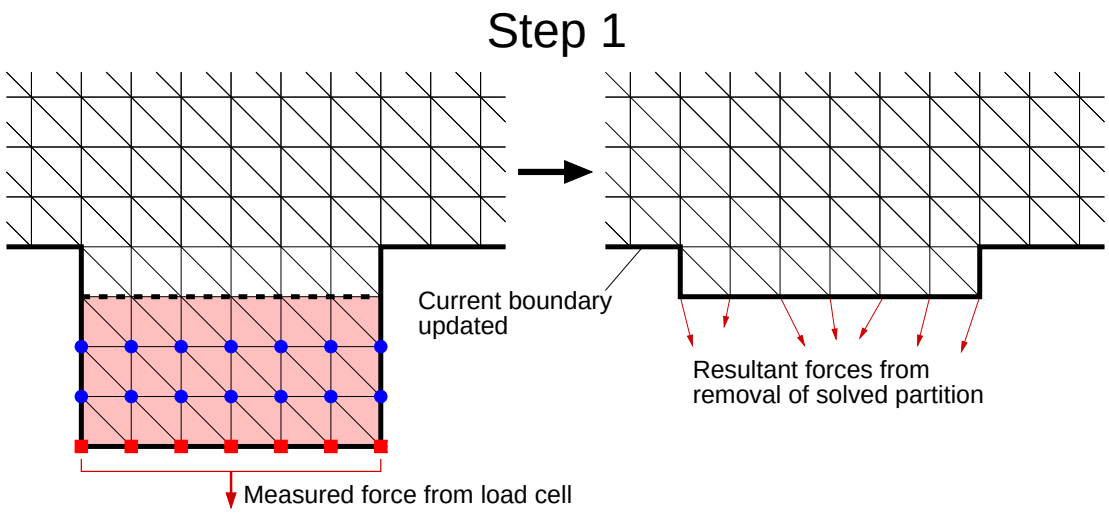

Figure 2.5: Step 1: Solving the boundary partition Partitions are formed and solved at the boundary regions corresponding to the arms. The bottom arm region is shown here with the gripped edge marked with red nodes. The shaded elements represent a partition size of n layers ($n = 3$ shown) from the gripped edge. The equations of the red nodes in the direction of pull are added and set equal to the total grip normal force obtained from load cell data. The blue nodes represent all nodes enclosed within n layers from the red nodes. Once the partition is solved, its elements are removed from the mesh and the resultant forces are applied on the remaining unsolved domain. The current boundary of the mesh is updated and the new nodes on the boundary provide further starting points to form partitions in *step 2*.

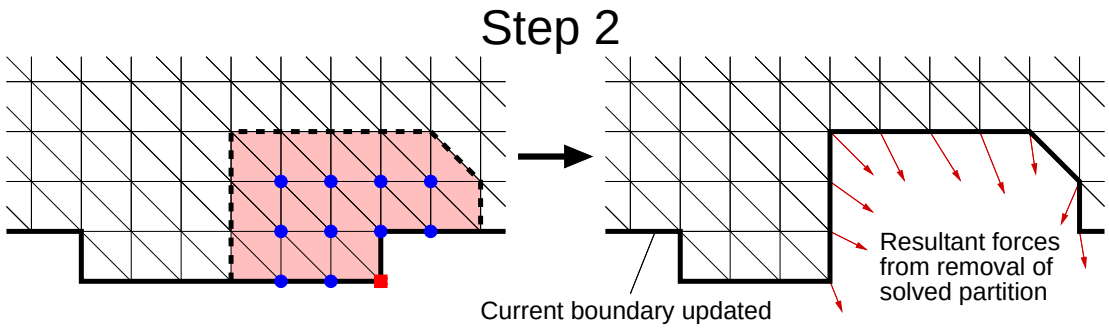

Figure 2.6: Step 2: Solving the interior partitions. After *step 1* is completed there are a number of nodes on the updated boundary which have calculated resultant forces. These nodes are starting points to create new partitions. The shaded elements shown in the figure represent a partition size of n layers ($n = 3$ shown) starting from the red node. If this selection of partition elements is accepted, the removal of solved elements gives resultant forces on the updated boundary. The process of solving partitions and removing them from the mesh is repeated until the entire domain is solved.

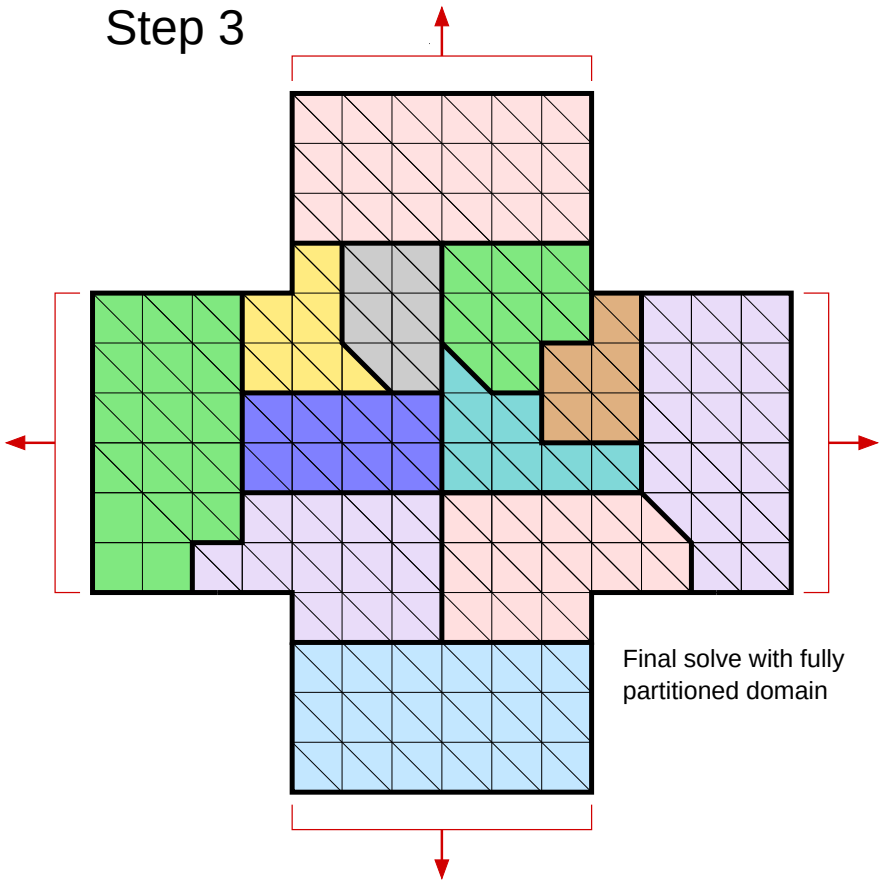

Figure 2.7: Step 3: Final solve of the partitioned domain. The fully partitioned domain is solved with a final pass for the coupled global system with all the grip forces. Each partition is shown by shaded regions with thick borders. The only non-zero terms in the force vector are those representing the grip forces.

are not used if they are connected to other unsolved elements. This step is repeated until all subdomains have been determined.

Step 3: Solving the coupled, global system using the obtained partitioning The set of all solved subdomains gives us the partitioning of the full sample domain. This partitioning is then used to construct and solve the global system in which the elastic constants of the subdomains are coupled (Fig. 2.7). This final pass enforces solving for all equations including unused equations from subdomain boundary nodes in previous steps.

2.3.2 Partition Shape Selection

In step #2 it is required to try various choices of subdomains that contain one or many nodes on the current boundary. There are numerous ways to select a candidate subdomain of contiguous mesh elements. These can differ in size and shape. Using the graph representation of the finite element mesh (Fig. 2.4), one can develop a library of partition shape selection tools. These tools can be used to generate a number of candidate partitions.

The unsolved domain shrinks continuously with the removal of solved partitions. Nodes on the current boundary have resultant forces from the removal of neighboring solved elements. In order to have a non-zero force vector for the solution of each partition (*c.f.* Eqn. 2.14) each candidate partition must contain such one or more such nodes. These nodes are considered to be starting points around which the neighboring elements are selected to form a candidate partition. While one can build an arbitrarily large number of partition shape selectors from a given start-node, we briefly describe a few that we commonly use:

Scoop: Choose all unsolved mesh elements that are within n layers of elements from the start node. This procedure can be visualized as scooping elements within a specified connection radius. Figure 2.8(a) shows this process where the red node on the current boundary is identified as a starting point due to the presence of non-zero forces (from removal of adjacent solved partitions). The first three layers of elements are shown shaded in different tones from dark pink (first layer) to light pink (third layer). The nodes that are contained in this partition are marked in blue. The dashed line represents the potential change in boundary if this partition is accepted and removed from the mesh. Equations of the nodes on the dashed line are unused.

Trim: If there are only one or two unsolved mesh elements connected to a start node on the current boundary then the elements can be donated to neighboring solved partitions if the equations of the trim node are satisfied within the tolerance. Figure 2.8(b) illustrates this where the trim node is marked in red and the previously solved partition (shaded blue) is neighboring the trim node. The two trim elements (shaded pink) can be donated to the blue partition if the

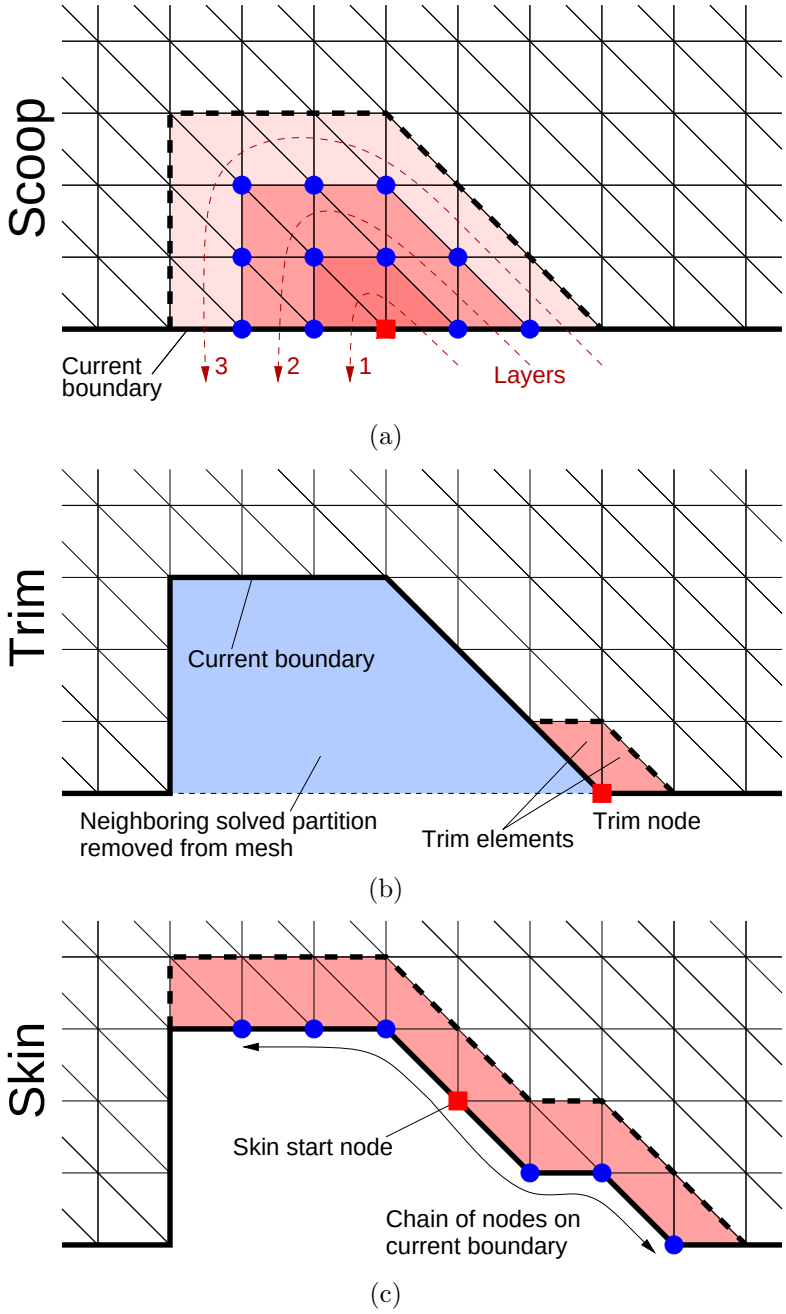

Figure 2.8: Different types of partition forming operations illustrated sequentially. Thick lines and dashed lines represent the current boundary and change in boundary (if partition is accepted) respectively. The red node on the boundary is a starting point with non-zero forces. (a) *Scoop*- Elements in the first three layers of the start node are shown shaded in different colors. (b) *Trim*- The two elements containing the trim node can be donated to neighboring solved partitions (blue) by checking for equations of the node. (c) *Skin*- A thin layer of elements connected to chain of nodes on the current boundary can be selected.

equations of the trim node are satisfied. The parameters of the neighboring solved partition are tried on the equations of the trim nodes.

Skin: This procedure is similar to the scoop operator but it selects layers of elements along the current boundary and does not dig into the domain's interior. This operator forms a chain of boundary nodes that are within n edges from the start node and selects all mesh elements connected to them. This procedure can be visualized as skinning elements on the surface. Figure 2.8(c) shows this for $n = 3$.

2.3.3 Partitioning Algorithm

In subsections §2.3.1 and §2.3.2 we outlined the solution procedure and the method of forming candidate partitions respectively. In this subsection we describe the partitioning algorithm in more detail. The three steps from §2.3.1 can be summarized into a basic solution algorithm shown in Algorithm 1. The analysis domain is continually shrunk by solving partitions on the exterior, removing the solved partitions and using the resultant forces to solve the remaining domain. Hence the boundary of the analysis domain is continually changing based on the number of boundary nodes with non-zero forces present at any given stage of processing. Using the mesh data structure of Fig. 2.4 we maintain a list of such nodes on the current boundary (henceforth referred to as NCB). After the completion of step #1 the NCB list is populated. In step #2 the NCB list is processed in sequential order and updated with change in current boundary by removing solved boundary nodes from the list and adding new boundary nodes to it. Within step #2 there can be many approaches to processing the NCB list. A library of such approaches could be built and ranked in terms of priority depending on the problem being solved. We describe two approaches below and mention the context of their use.

Algorithm 2 shows the combinination of a series of scoop and trim operations. Candidate partitions of large scoop sizes are tried on all nodes in the NCB list. After all the nodes in the list are processed and if the domain is not fully solved then the method attempts trimming the unsolved elements of the current boundary. Following this, the cycle of scoop and trim is repeated multiple times with the scoop size being decreased after every cycle. The combination of scoop and trim in this method

Input: mesh, displacements and grip forces from all experiments,
user-specified residual force tolerance
Output: Partitioning of the domain, anisotropy and stiffness of each
partition

```
/* STEP 1:  Solve the boundary partitions                    */
while unsolved boundary partitions exist do
    Solve boundary partition with corresponding grip force data;
    Remove solved partition from mesh;
    Update list of nodes on current boundary with resultant forces (NCB);
end
/* STEP 2:  Solve the interior partitions                    */
foreach node in NCB list do
    Examine candidate partition containing the node;
    /* Partition selection acceptance criterion              */
    if residual force norm is within tolerance then
        Accept solution and remove solved partition from mesh;
        Update NCB list;
    end
end
/* STEP 3:  Final solve and output of results                */
Assemble fully partitioned domain and perform final solve;
Output alignment and modulus maps for visualization;
```

Algorithm 1: Basic GAIM solving procedure

leads to rapid solution time. This method has been successful in detecting the shape and location of an inclusion within a larger sample especially when the noise in the measured response is low. We will present an example with this method in §3.2.

Algorithm 3 shows a modification to the previously mentioned approach. Here, instead of accepting a candidate partition if it meets the tolerance criterion, the method scans all possible choices in the NCB list and selects the partition that leads to the lowest residual force norm. This process is continued with cycles of scoops with decreasing size, and trims. This method requires the population of a list of residual force norm values ($RFNorm$) corresponding to the various alternatives of partitions at scoop locations. The list is continually updated with the acceptance of every partition. Because of the search for the minimum norm at every stage, this method

```
Input: NCB list, current domain, solved domain
Output: Form partitions by scoop and trim operation, solve them and
        shrink the unsolved domain

for scoopSize ← maxSize to minSize do
    foreach node in NCB list do
        Examine candidate partition of size scoopSize;
        Accept and update NCB list if acceptance criterion is satisfied;
    end
    Examine trimming the elements on current boundary;
    Accept trim of elements which have residual force norm within tolerance;
end
```

Algorithm 2: Scoop and trim based processing of interior partitions

```
Input: NCB list, current domain, solved domain
Output: Form partitions by scoop and trim operation, solve them and
        shrink the unsolved domain

for scoopSize ← maxSize to minSize do
    foreach node in NCB list do
        /* Find the partition with lowest residual force norm  */
        foreach node in NCB list do
            Examine candidate partition of size scoopSize;
            Store residual norm in list RFNorm;
        end
        Accept partition with the lowest value in the RFNorm list;
        Update NCB and RFNorm lists;
    end
    Examine trimming the elements on current boundary;
    Accept trim of elements which have residual force norm within tolerance;
end
```

Algorithm 3: Scoop and trim processing guided by a minimum norm search

involves significantly more computation time than that of Algorithm 2. However, Algorithm 3 has been found to be particularly advantageous in detecting gradual changes in material properties. This method has been applied successfully to tests on collagen tissue equivalents which are detailed in section §4.3.5.

2.4 Visual Representation of Anisotropy

The full determination of all the C_{ijkl} constants of the elasticity tensor allows identification of particular elastic symmetries [44] by analyzing the eigentensors (or principal elasticities as proposed by Lord Kelvin [45]) of C. Using the major and minor symmetries, the 4th rank elastic tensor C can be compacted into a 2D matrix form that relates the components of stress and strain

$$\begin{bmatrix} \sigma_{11} \\ \sigma_{22} \\ \sigma_{12} \end{bmatrix} = \begin{bmatrix} C_{1111} & C_{1122} & C_{1112} \\ C_{1122} & C_{2222} & C_{2212} \\ C_{1112} & C_{2212} & C_{1212} \end{bmatrix} \begin{bmatrix} \varepsilon_{11} \\ \varepsilon_{22} \\ 2\varepsilon_{12} \end{bmatrix} \tag{2.24}$$

Written in this form C does not constitute a 2nd rank tensor but can be converted into a 2nd rank tensor $\hat{C}$ by the transformation

$$\begin{bmatrix} \sigma_{11} \\ \sigma_{22} \\ \sqrt{2}\sigma_{12} \end{bmatrix} = \begin{bmatrix} C_{1111} & C_{1122} & \sqrt{2}C_{1112} \\ C_{1122} & C_{2222} & \sqrt{2}C_{2212} \\ \sqrt{2}C_{1112} & \sqrt{2}C_{2212} & 2C_{1212} \end{bmatrix} \begin{bmatrix} \varepsilon_{11} \\ \varepsilon_{22} \\ \sqrt{2}\varepsilon_{12} \end{bmatrix} \tag{2.25}$$

Rewriting Eqn. 2.25 in matrix form for the transformed matrices and vectors

$$\hat{\sigma} = \hat{C}\hat{\varepsilon} \tag{2.26}$$

The eigenvalue states of $\hat{C}$ were referred to by Lord Kelvin as the principal elasticities. These represent symmetry states in which $\hat{C}$ converts a strain vector $\hat{\varepsilon}$ into a parallel stress vector $\hat{\sigma}$ by

$$\hat{\sigma} = \hat{C}\hat{\varepsilon} = \Lambda\hat{\varepsilon} \tag{2.27}$$

$$(\hat{C} - \Lambda I)\hat{\varepsilon} = 0 \tag{2.28}$$

The eigenvalues Λ^k are denoted as the *Kelvin moduli* ($k = 1, 2, 3$ for 2D). The eigenvectors $\hat{\varepsilon}^k$, when projected back into Cartesian tensor form are termed as *strain eigentensors*, and the corresponding stresses are *stress eigentensors*. The normalized

strain eigentensors of the symmetry states of Eqn. 2.28 can be computed as

$$\hat{\varepsilon}^k = \begin{bmatrix} a \\ b \\ c \end{bmatrix}, \quad a^2 + b^2 + c^2 = 1 \quad \Rightarrow \quad \varepsilon^k = \begin{bmatrix} a & \frac{c}{\sqrt{2}} \\ \frac{c}{\sqrt{2}} & b \end{bmatrix} \tag{2.29}$$

For example, isotropic materials have one eigentensor of dilatational mode and two eigentensors of isochoric (distortional) mode, and the largest Kelvin modulus is associated with the dilatational mode. Orthotropic materials have three distinct Kelvin moduli corresponding to three deformation modes– one mode of shear in the symmetry plane and two modes of extension/contraction along symmetry axes. Since the strain eigentensor ε^k represents a strain state, we compute its principal values (λ_1, λ_2) and principal directions (θ_1, θ_2). For the case of fibrous materials based on an underlying fiber distribution and mean orientation, the major principal direction of the strain eigentensor corresponds to the preferred fiber orientation. We convert the principal values $(\lambda_1, \lambda_2;\ \lambda_1 > \lambda_2)$ of the strain eigentensor corresponding to the largest Kelvin modulus into a measure of degree of alignment analogous to the normalized retardation in polarized light microscopy [4]

$$r_{GAIM} = \frac{|\lambda_1| - |\lambda_2|}{|\lambda_1| + |\lambda_2|} \tag{2.30}$$

Hence, the values for r_{GAIM} vary from 0 (for an isotropic sample) to 1 (for a completely aligned sample). Regional variation in anisotropy can be visualized by an alignment map generated from the major anisotropy direction and value of r_{GAIM} over each partition. Furthermore, a stiffness map can be generated by plotting the largest Kelvin modulus over each partition.

2.5 Steps to Reduce the Ill-Posedness of the Inverse Problem

Figure 2.9 shows the mapping from the material response domain to the material properties domain during the solution of an inverse problem. The region within dashed lines in the domain of material properties represents the spread of possible material parameters that closely fit the response in the shaded region of the domain of material response. There is an inherent loss of information in the mapping from

response to properties and this is the cause of the ill-posedness of the inverse problem. In the presence of noise, the range of material response is increased leading to a significantly larger increase in the range of material properties, further exacerbating the ill-posedness. Methods that reduce the ill-posedness can be thought as those that supply additional information or constraints that shrink the domain of possible material properties (Fig. 2.9) from the dashed region to the region shaded in pink. This process is also termed as regularization of the inverse problem. A couple of methods that we employ to improve the reliability of the process of C_{ijkl} parameter extraction are discussed below.

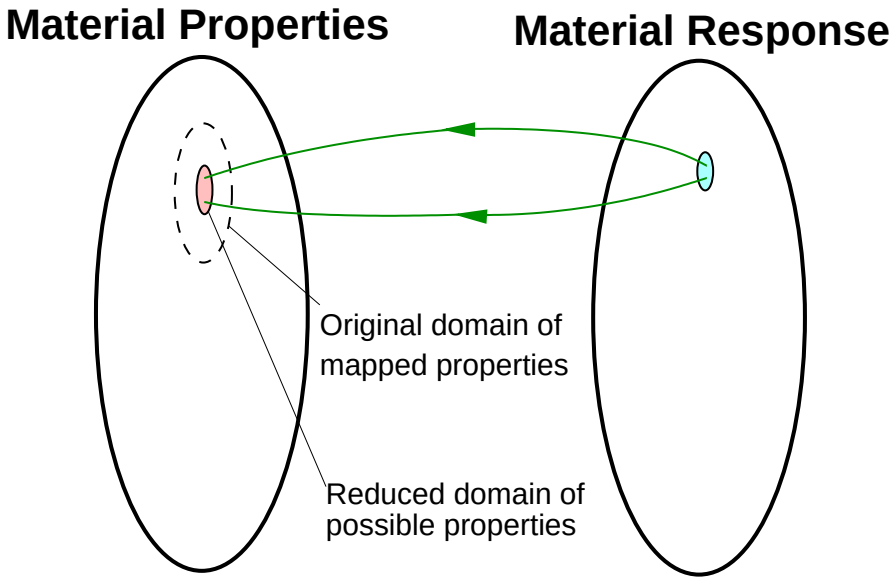

Figure 2.9: The effect of reducing ill-posedness by better conditioned system is that of shrinking the domain of possible material parameters that fit the given response.

2.5.1 Heterogeneity of the Strain Field

It can be noticed from Eqn. 2.21 that each element has a column dependence on $\varepsilon_{11}, \varepsilon_{22}$ and ε_{12} for the respective parameters of C_{1111}, C_{2222} and C_{1212}. Terms C_{1122}, C_{2212} and C_{1112} have a column dependence on a linear combination of the three strain components. In the assembled form, each nodal equation uses the strain contribution from all connected elements. If the strain field is homogeneous in a partition, then redundant equations result at its nodes. The confidence of parameter extraction in each partition is increased by providing more information; heterogeneous strain fields

provide a larger span of inputs and increase the sensitivity of the parameters to the deformation and are therefore desirable.

Heterogeneity in the strain field can be generated in a number of ways by manipulating the following: gripping condition at the boundaries, sample geometry, and asymmetry in the applied loading. A number of methods to grip the sample at the boundaries include using sutures, hooks and clamps (Fig. 2.10). Sun *et al.* [46] performed a detailed analysis of the effect of various gripping conditions on the nature of the stress and strain fields generated in the biaxial testing of soft tissues. It was shown that the use of suture attachments resulted in homogeneous strain fields with significant load transfer to the inner region. However, the negligible shear from this method would lead to poor accuracy in determining the shear components of the elastic tensor. In comparison, use of clamps produce significant strain heterogeneity, shear and Saint-Venant effects at the boundaries. These also result in high stress concentrations at the corners leading to an under-loaded inner region. The stress concentration at corners of cruciform shaped samples can be avoided by using curved edges (dashed lines in Fig. 2.10).

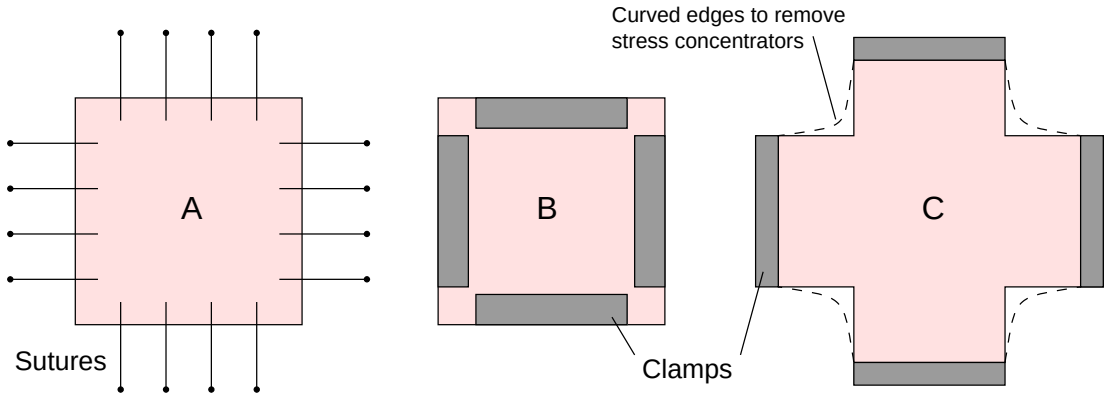

Figure 2.10: Different types of sample attachment for biaxial testing: A) Hooks or sutures are the most commonly used method. They produce homogeneous strain fields and transfer most of the loads to the inner region. Negligible shear is produced with this method; B) Clamps fixing a square shaped sample generate heterogeneous strain fields and shear at the boundaries. There are high stresses at the corners which take most of the loads and transfer little to the inner region; C) Clamps fixed on a cruciform shaped sample produce similar results with heterogeneous strain fields at the arms and boundaries. There are high stresses at the corners. Use of curved edges (dashed lines) will remove the stress concentrators and lead to better load transfer to the inner region.

The curved cruciform geometry with clamped ends is preferable for the sample shape to provide shear, strain heterogeneity and optimal transfer of loads to the inner region. Asymmetric sample geometry and rotation of sample arms relative to the loading axes can further increase the heterogeneity of the strain field.

2.5.2 Multiple Testing Protocol

The strain heterogeneity mentioned in §2.5.1 is limited to the region at the arms and boundaries in the case of equibiaxial loading. In order to increase the span of the strain-space at each region of the sample we perform multiple experiments by varying the hold/stretch at each arm. Figure 2.11 shows a schematic of the various loading protocols that can be applied for the four arms of the biaxial test. Each arm can be held or stretched leading to a total of 15 possible tests excluding the trivial four-way hold. The asymmetric stretches induce shear at arms and parts of the inner region and contribute to a more balanced set of strains spanned. The equations from multiple experiments are combined and solved in a least-squares sense. In doing so, we assume that the material properties in each partition do not change significantly between experiments. If the strains applied are moderately high but not too large to cause damage then this assumption is reasonable. The resulting parameters that are extracted represent a best fit to the average response over all experiments. An additional equibiaxial test can be performed at the end of the fifteen tests and compared with the first equibiaxial test to ensure that any changes that occurred due to the testing protocol were insignificant.

2.6 Noise Sensitivity and Evaluation of Model Performance

It is imperative to test the robustness of an inverse method in the presence of noise. Due to the ill-posed nature of inverse problems, small errors in the measured response have large effects on the parameter extraction. Some of the possible sources of errors in the inversion are listed below and are followed by a brief description of how they are handled.

1. Noise associated with load measurement

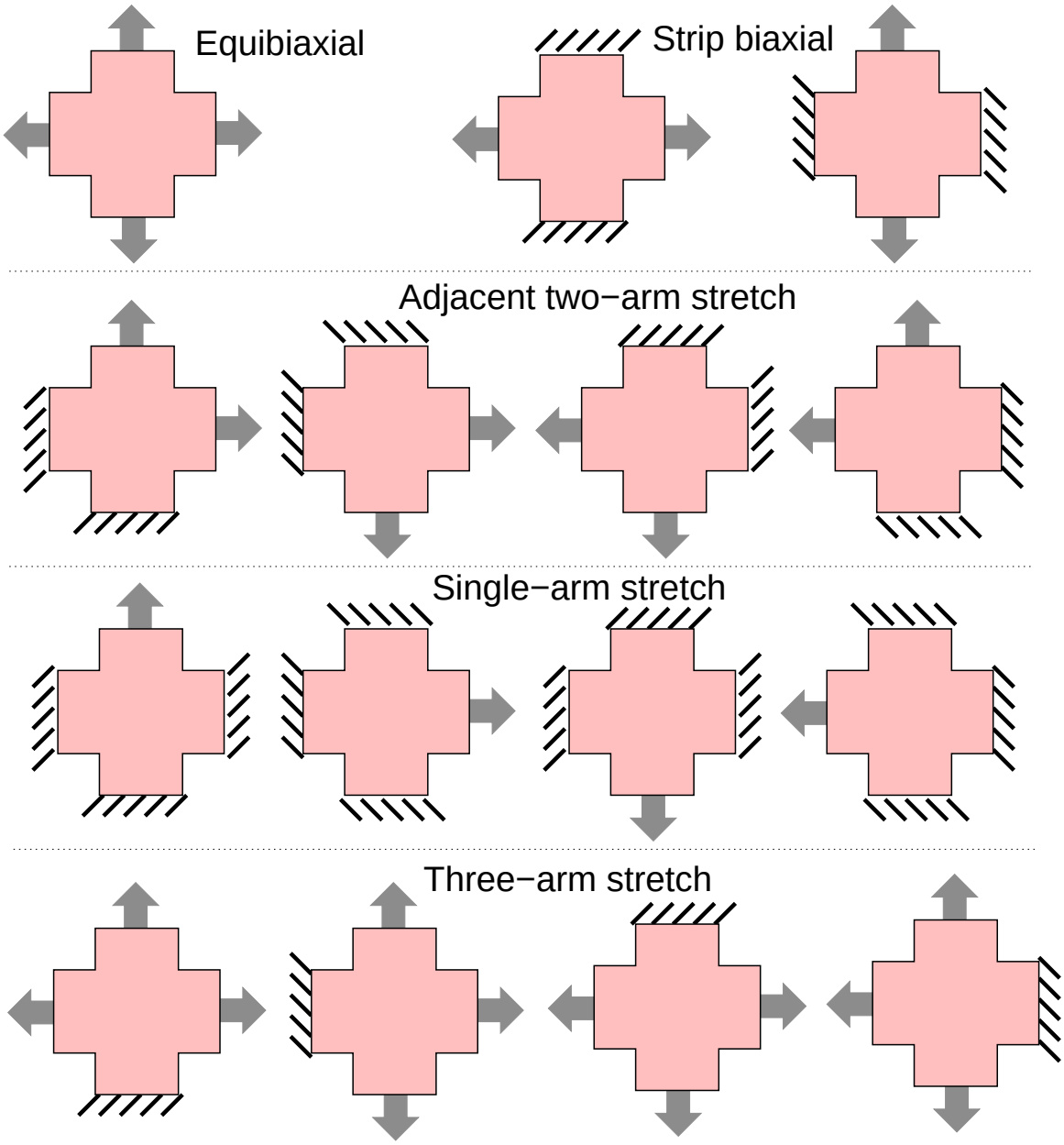

Figure 2.11: Multiple biaxial tests for GAIM: Each of the four arms of the cruciform sample are either extended or held fixed. A total of fifteen biaxial tests are performed by these basic protocols: equibiaxial, strip-biaxial (2), adjacent two-arm (4), single-arm (4), and three-arms (4), where the number in parenthesis represents the number of cyclic permutations of each protocol.

2. Errors in the nodal displacement calculation from images
3. Errors in the assumption of homogeneity of partition
4. Errors in the material model

Grip forces during the biaxial tests are recorded continuously from the load cells. Fluctuations in the force measurement might be caused due to the inaccuracy of the load cells and vibrations in the experimental setup. The load cells are calibrated before the testing protocol is run. Slow rates of loading ($\sim$ 1mm/sec) are used to minimize dynamic effects. Fluctuations in the load versus time plot are smoothed using the curve fitting toolbox in MATLAB® to reduce the errors.

The nodal displacements are calculated by digital image correlation (DIC) of the image sequence corresponding to the loading curve. A detailed description of the displacement calculation by DIC is given in appendix §2.7. The image correlation technique is applied incrementally between successive pairs of images and hence errors can accumulate progressively. Error in displacement calculation is critical and has the most influence in the parameter extraction. Noise in displacement is amplified partly due to taking gradients for the calculation of strains, and also due to the inversion of K matrix in Eqn. 2.22. To reduce errors in the image correlation, we calculate the displacements on the nodes of a fine mesh and apply a smoothing filter on the displacement field between each pair of images. The filter minimizes the local gradients in the displacement field. Subsequent to smoothing, the displacement field on a coarse mesh is obtained by interpolation and the coarse mesh is used for the parameter extraction. This method of computing displacements on a fine mesh, smoothing and fitting them onto a coarse mesh provides high accuracy in the strain field.

One of the assumptions in the GAIM model is that the heterogeneity in the sample domain can be represented in the form of piecewise homogeneous subdomains. If the properties inside each partition are continuously varying then the assumption of constant C_{ijkl} over the partition is not accurate. However, we adopt the linear, least squares method for solving Eqn. 2.14 so that the L2 norm ($\|\cdot\|_2$) of the errors in forces

at all finite element nodes are minimized. This results in an extracted parameter set that is a best fit homogeneous approximation over the observed response.

Nonlinear and time-dependent material response of soft tissues is not accounted for in this method. It may not be possible to obtain a reasonable fit of the response to a linear model. Errors in the model fit are reflected as large residuals in the nodal forces. Non-positive definite C_{ijkl} parameters are another indication of poor fit. Even if the material response is nonlinear it is possible that a linear model is sufficient to capture qualitative changes in regional anisotopy and stiffness. In this case the stiffness measure is a secant modulus and not a tangent modulus.

Since we solve the inverse problem (Eqn. 2.14) directly by the linear least squares method (Eqn. 2.22) the potential application of linear regression tools to evaluate the fit of the model is appealing. The common assumption in linear regression theory [47, 48] is that the predictor variables (inputs or independent variables) are error-free, and the errors in the response variables (outputs or dependent variables) are uncorrelated with the predictors. However in the GAIM model, the matrix of predictors (K) is a function of computed strains and hence subject to errors. The output variables ($\mathcal{F}$) are a vector of forces and are also subject to errors since the non-zero terms are forces measured by load cells. If the true and unobserved values of K and $\mathcal{F}$ are K^* and $\mathcal{F}^*$ respectively then

$$K = K^* + e_K \tag{2.31}$$

$$\mathcal{F} = \mathcal{F}^* + e_{\mathcal{F}} \tag{2.32}$$

where e_K and $e_{\mathcal{F}}$ are the corresponding errors. Assuming that the true $\mathcal{C}$ parameters are related to the true values K^* and $\mathcal{F}^*$ then

$$\mathcal{F}^* = K^* \mathcal{C} \tag{2.33}$$

$$(\mathcal{F} - e_{\mathcal{F}}) = (K - e_K)\,\mathcal{C} \tag{2.34}$$

$$\mathcal{F} = K\,\mathcal{C} + (e_{\mathcal{F}} - e_K\,\mathcal{C}) \tag{2.35}$$

Application of the least squares method to solve Eqn. 2.35 can result in biased estimates because

$$\text{covariance}(K,\, e_{\mathcal{F}} - e_K\, \mathcal{C}) \neq 0 \tag{2.36}$$

Ref. [48] contains a description of measurement error models that handle errors in the predictors. However, it is possible to apply standard linear regression tools if the errors in the K matrix cause negligible bias. In the next subsection we perform simulated tests with noise to examine the feasibility of using 95% confidence intervals to estimate the performance of the model.

2.6.1 Displacement Noise Sensitivity Tests

The performance of the GAIM model in the presence of noise in displacements was investigated on a quadrilateral mesh constructed out of a 7×7 grid of elements, with the four corner elements removed to represent a cruciform (Fig. 2.12). We used an orthotropic material with the following elastic constants

$$\begin{bmatrix} C_{1111} & C_{1122} & C_{1112} \\ & C_{2222} & C_{2212} \\ \text{symm} & & C_{1212} \end{bmatrix} = \begin{bmatrix} 19 & 10 & 0 \\ 10 & 28 & 0 \\ 0 & 0 & 6 \end{bmatrix} \text{GPa} \tag{2.37}$$

and rotated the orthotropic axes by $-60°$. The material in the cruciform was assigned the values corresponding to the rotated C tensor. These values were taken from Ref. [49] and used only for illustrative purposes. A single asymmetric extension test was performed on the cruciform with the adjacent two-arm stretch of 2.5% and the other two arms held fixed. The boundary forces and displacement response were obtained.

Random error drawn from a uniform distribution was added to the nodal displacements. The four normal grip forces and the noisy displacement data were used by GAIM to obtain C_{ijkl} values for the entire cruciform modeled as a single homogeneous partition. Multiple runs were performed with various noise amplitudes ranging from 0.1–10.0% of the maximum displacement. The C_{ijkl} values were averaged over 1000 trials for each noise level and are shown in Fig. 2.13(a) with the error bars representing the standard deviation of 1000 trials. Figure 2.13(b) shows the anisotropy direction

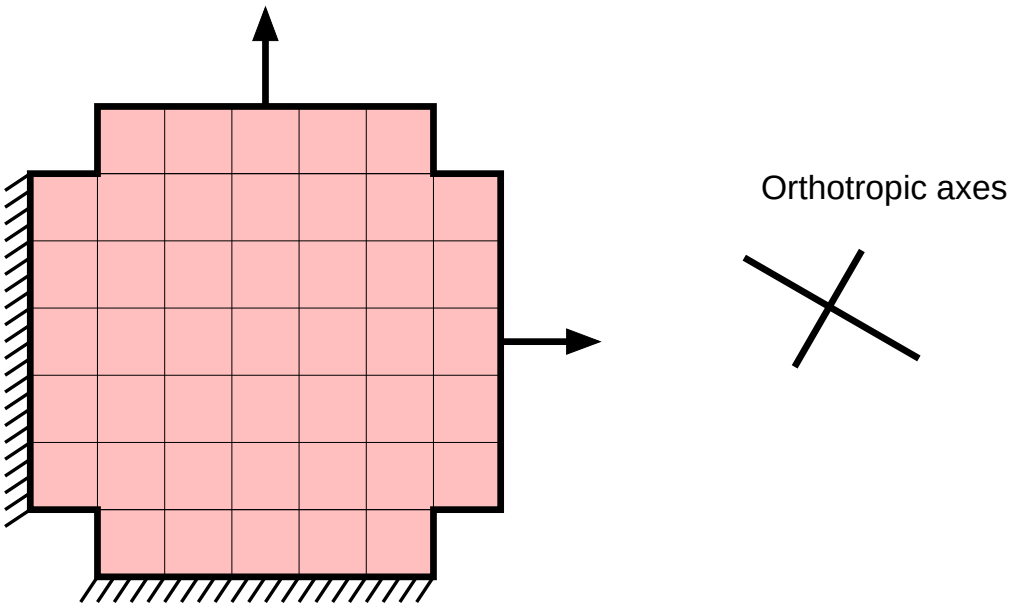

Figure 2.12: A cruciform mesh with the adjacent two-arm stretch test is used for the noise sensitivity analysis. The material properties assigned to all elements are those that correspond to the rotated state of orthotropy (the orthotropic axes shown are the two directions along which the moduli values are 19 GPa and 28 GPa).

(principal directions of the largest Kelvin moduli) for each of the noise levels. The error bars represent the standard deviation from 1000 trials. The anisotropy angle is accurate within $\pm 5^\circ$ upto noise levels of 3%. The growth of the standard deviation (normalized by the mean value) in C_{ijkl} values show a direct proportionality with noise up to 4% (Fig. 2.13(c)). These plots indicate that more than 3–4% noise in the displacement fields result in poor estimates of C_{ijkl} parameters.

To test whether we can apply the theory of linear regression [47] and obtain unbiased estimates of the model's performance in the presence of errors in the regressors, we computed the 95% confidence intervals for the C_{ijkl} estimates and compared them with the standard deviations (Fig. 2.13(d)). It is seen that there is strong correlation between the standard deviations (from multiple trials) and confidence intervals (from linear regression). This suggests that there is negligible bias from errors in the regressor. Confidence intervals may therefore be used as a metric to assess the performance of the model. This provides us an additional measure to the assess the fit instead of only comparing the residual force norm against a pre-set tolerance.

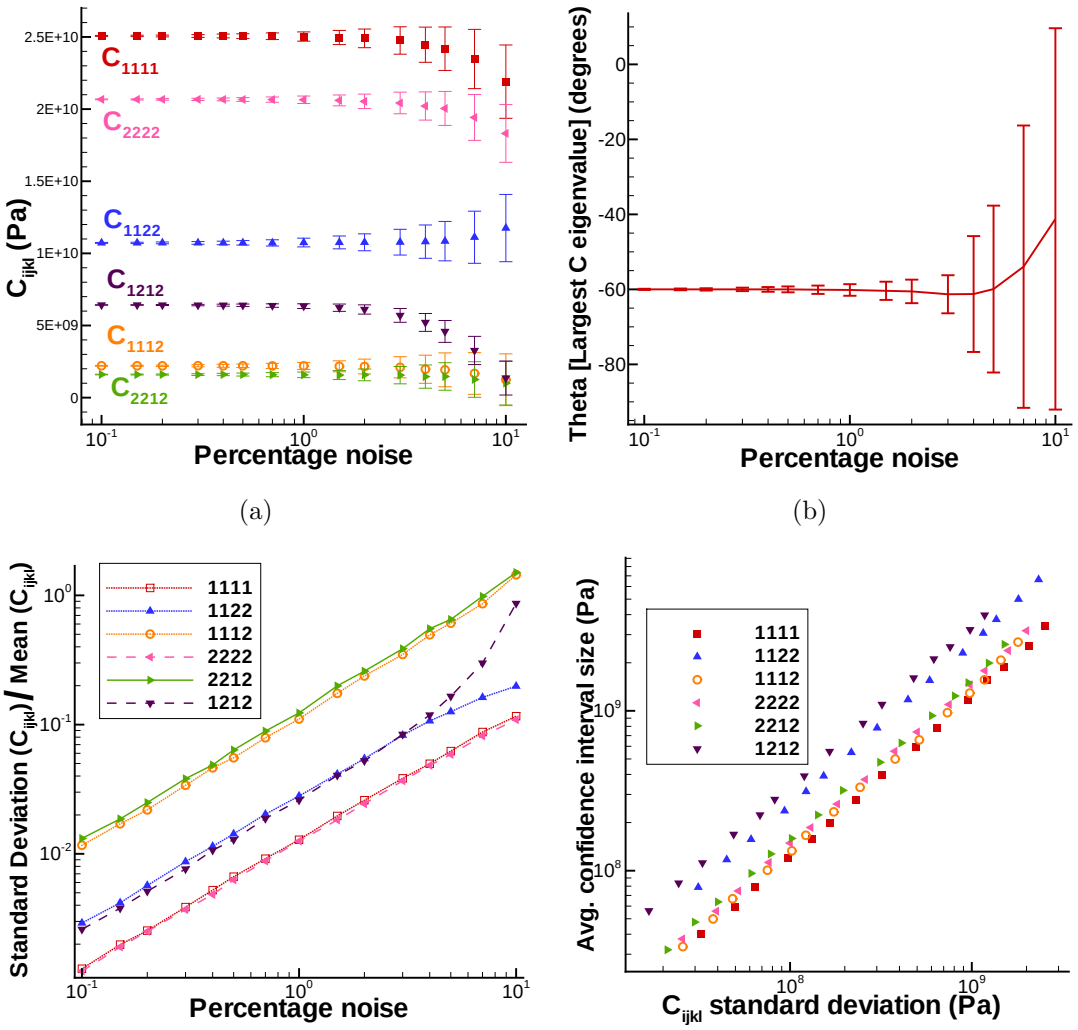

Figure 2.13: Displacement noise sensitivity results- (a) C_{ijkl} values sensitivity to noise, (b) Principal direction of C_{ijkl}, (c) Normalized standard deviation of C_{ijkl}, (d) Correlation between standard deviation and confidence intervals,

2.7 Strain Tracking for GAIM

A critical component to the successful application of GAIM on data from mechanical tests of soft tissues is the estimation of accurate full-field displacements from motion capture of the tissue deformation. It is further required that these displacement fields be available for the continuous deformation occurring during multiple test protocols. Errors in the displacement field estimation have drastic effects on the inversion of material parameters since the inverse matrix is a function of strains which amplify the errors due to the gradient operator on a noisy field. In this section we briefly outline our method for accurate estimation of the displacement and strain field for a tissue sample undergoing multiple biaxial stretch protocols.

2.7.1 Digital Image Correlation (DIC)

DIC is a image registration technique that determines the location of matching image subsets drawn from two or more images. Given two image subsets, the pixel array intensities of the two are correlated against each other to obtain a correlation function whose maxima corresponds to the location of the best match between the two subsets. A detailed review of various DIC techniques for estimating displacements and strains is provided in Refs. [78,79] where the authors compared the performance of correlation algorithms in spatial versus Fourier domains (e.g., [80–82]) and subpixel algorithms that used interpolation for peak detection and those that used iterative least squares to account for the deformation of the subset (e.g., [83, 84]). We adopt the method outlined in [84] where coarse displacement estimates are obtained by the normalized cross-correlation function (Matlab function `normxcorr2`) and the subpixel displacements from the iterative Newton-Raphson method. The subpixel method accounts for linear shift and scaling in the light intensity spectrum.

The recorded video capture of the tissue deformation is downsampled and processed to obtain a grayscale image sequence. The images are synchronized with the load cell data to identify the images corresponding to the start of the test and over each loading protocol. The image of the sample before the start of the test is used as the reference configuration and the region of interest is sketched and meshed with quadrilateral meshes in Abaqus. This finite element mesh is mapped onto the image

and successive pairs of images in the sequence are correlated to identify the movement of the locations corresponding to the mesh nodes. After the locations of the nodes on the next image are determined, the displacement field from the scattered data is smoothed by cubic-spline smoothing on a grid that is oversized in comparison to the mesh edge size ($\approx$ 1.5–2 mesh edge lengths). At each successive step of the correlation, the movement of the integer pixels nearest to the current locations of mesh nodes is estimated and the displacement field is smoothed and interpolated at the current nodal location to obtain a continuous tracking of the mesh nodes. Strains were computed using finite-element theory from the estimated nodal displacements the bilinear quadrilateral mesh elements. A graphical user interface based program was developed in Matlab to perform the continuous strain tracking and is shown in Fig. 2.14

2.8 Summary of the GAIM Method for Determining Regional Changes in Anisotropy and Heterogeneity

Conventional methods in biaxial testing of soft tissues require strain homogeneity and prefer symmetric shapes in order to measure the stress response to specific strain states. In stark contrast, tissue testing for GAIM requires a paradigm shift in the design of experiments due to the preference for heterogeneous strain fields and asymmetry in sample geometry and loading.

In the previous sections we have outlined the mathematical model, computer implementation and design of experiments for the GAIM method. We summarize the keys steps from different stages of tissue testing, data processing and analysis using the schematic shown in Fig. 2.15 which is explained below.

Experiments: Tissue samples are cut to cruciform shape and speckled with stains or dye to provide visual texture for digital image correlation (DIC). The sample is loaded on a biaxial testing unit (e.g, Instron planar biaxial tester) and gripped by clamps. An overhead digital camera records the motion of the tissue during the entire duration of the test. A multi-experiment loading protocol is specified based on §2.5.2. The test is performed while recording the tissue motion and grip forces.

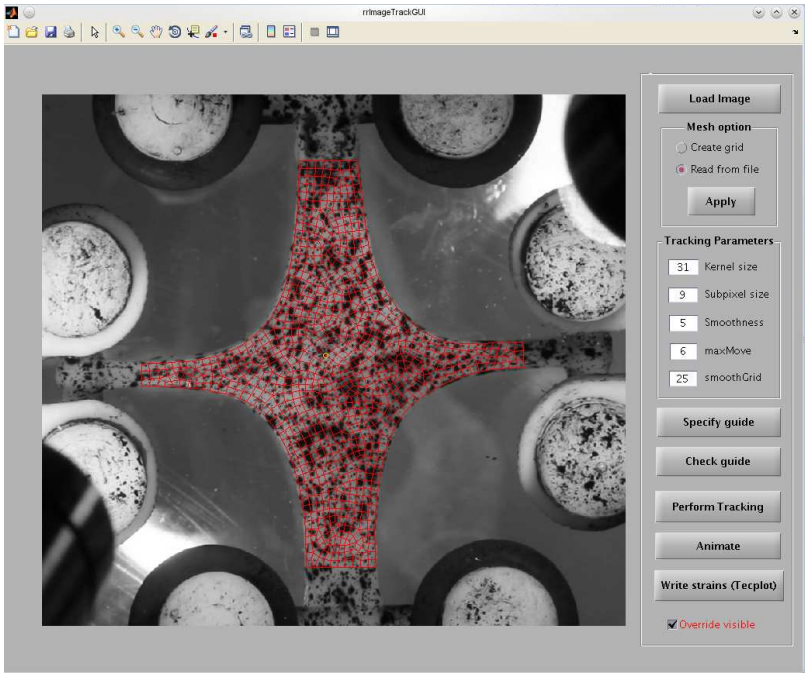

(a)

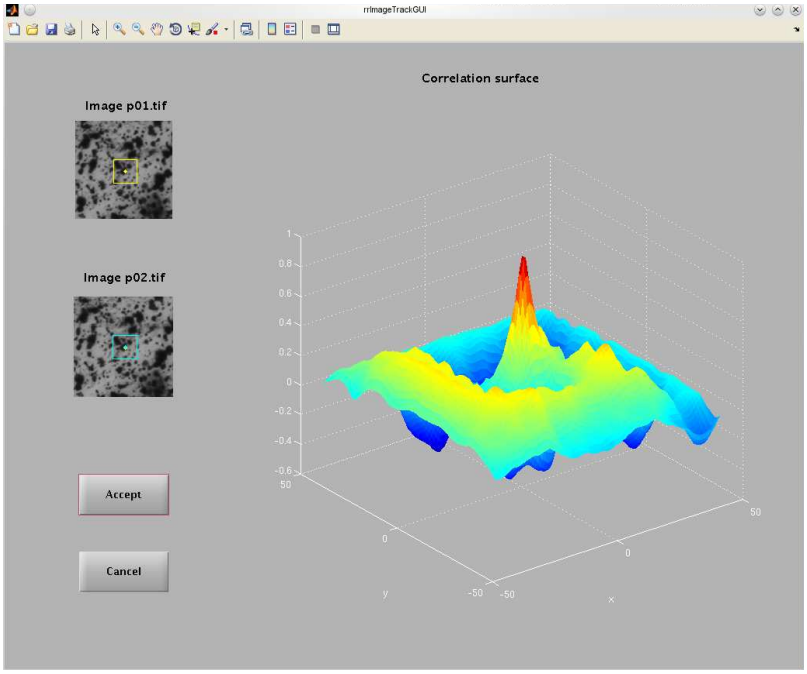

(b)

Figure 2.14: Graphical user interface for strain tracking- (a) Finite element mesh is overlaid on the image and tracked at nodal locations, (b) Tracking parameters are chosen to obtain clear peak in correlation surface for a user-specified point

Data Processing: The two main data sets obtained from the previous step are the grip forces from the load cells and the image sequence for each experiment. The loading curve of force data is smoothed if necessary, and the total force applied between the unloaded and fully deformed configuration is computed for each arm over each experiment. The video capture is downsampled to a sufficient frame rate and grayscale image sequences are extracted. The image sequences are synchronized with the loading cycles and the image corresponding to the undeformed configuration is identified. The boundary of the tissue within the grips is sketched in Abaqus and a 2D mesh is generated to represent nodal locations that will be continuously tracked by DIC (see details in appendix §2.7) from the undeformed to fully-deformed states of each experiment. The displacement fields of tracked nodes are smoothed to reduce noise artifacts when computing strains.

GAIM Analysis: The processed data set of grip forces and nodal displacements are input to the inverse solver. The user provides a guide for the solver by specifying the acceptable level of tolerance in the residual force norm. The user can examine the degree of fit of the C_{ijkl} parameters with the 95% confidence intervals and decide whether to repeat the analysis with different settings. There is flexibility in specifying the approximate size of partitions. The results can be visualized in the form of alignment and stiffness maps which describe the following three output: (i) partitioning of the domain, (ii) regional changes in direction and degree of anisotropy, and (iii) regional changes in the Kelvin modulus.

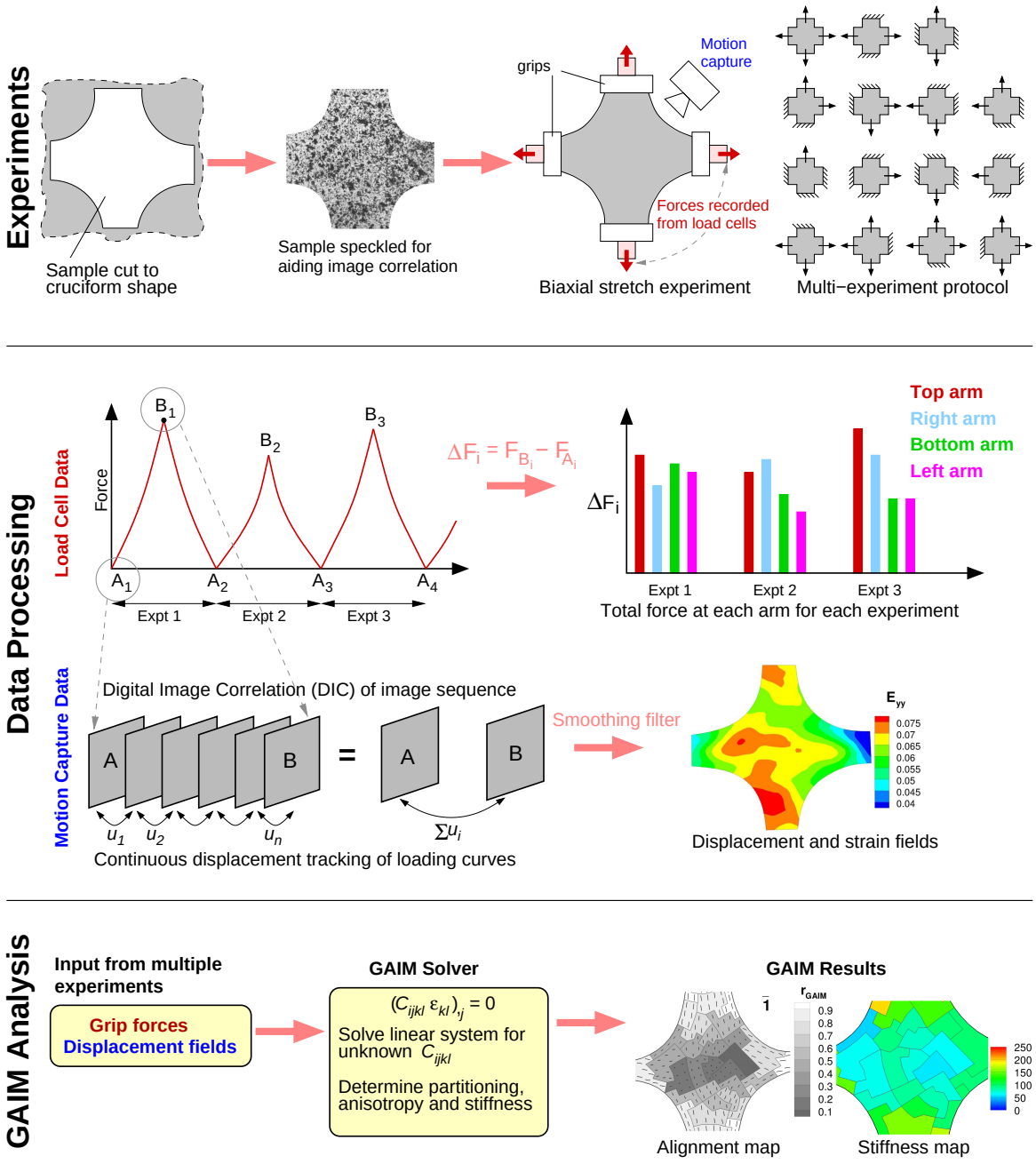

Figure 2.15: Schematic for the GAIM method showing the process flow between experiments, data processing, solution and visualization of results.

Chapter 3

Application to Simulated Experiments

This work was a part of the paper:

Generalized Anisotropic Inverse Mechanics for Soft Tissues
Journal of Biomechanical Engineering, 2010, 132(8)
Raghupathy, R. and Barocas, V.H.

3.1 Introduction

In this chapter, we apply the GAIM model to simulated data and test the method's capability to identify regional changes in anisotropy and heterogeneity. Artificial test data are generated by simulations of the forward problem. The artificial data are passed to the inverse solver, and the results are compared with the input anisotropy and heterogeneity. First, we test the case of an inclusion within a sample, a common test case with inverse problems, and demonstrate that the method can detect the presence and location of material difference. Second, we examine the performance of the model with simulated data from a nonlinear constitutive model applicable to soft tissues. It is shown that the linear model of GAIM is sufficient to identify regional changes in anisotropy and heterogeneity in soft tissues.

3.2 Linear, Orthotropic Sample with Heterogeneity

Detection of the presence and location of a hidden inclusion within a sample is a common test case in inverse mechanics [cite here]. We test this in the context of anisotropic soft tissues by using a cruciform shaped orthotropic sample with an inclusion whose orthotropic axes are rotated with respect to the sample. Figure 3.2 shows the cruciform and square shaped inclusion along with their orthotropic axes. For the material outside the square box we set the values of

$$\begin{bmatrix} C_{1111} & C_{1122} & C_{1112} \\ & C_{2222} & C_{2212} \\ \text{sym} & & C_{1212} \end{bmatrix} = \begin{bmatrix} 190 & 100 & 0 \\ & 280 & 0 \\ \text{sym} & & 60 \end{bmatrix} \text{kPa} \tag{3.1}$$

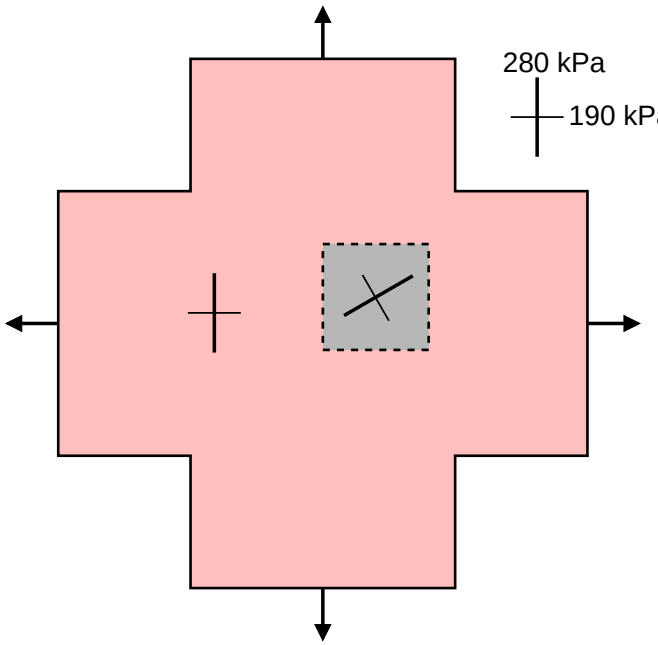

Figure 3.1: Schematic of test for detection of inclusion inside sample. Cruciform shaped sample (pink) is a linear orthotropic material whose orthotropy axes correspond to the Cartesian axes. The inclusion inside the box (gray) has rotated axes of orthotropy. The cruciform is stretched equibiaxially by 3% and the data from the simulated experiment are passed to the inverse solver.

These values were adapted from [49] and are used for illustrative purposes. For the

material inside the square box, we rotated the orthotropic axis clockwise by 60° and used the corresponding values of

$$\begin{bmatrix} C_{1111} & C_{1122} & C_{1112} \\ & C_{2222} & C_{2212} \\ \text{sym} & & C_{1212} \end{bmatrix} = \begin{bmatrix} 251 & 107 & 22 \\ & 207 & 16 \\ \text{sym} & & 64 \end{bmatrix} \text{kPa} \tag{3.2}$$

The forward problem was solved for a single equibiaxial stretch test with the four arms extended by 3%. The strains from the forward simulation are shown in Fig. 3.2.

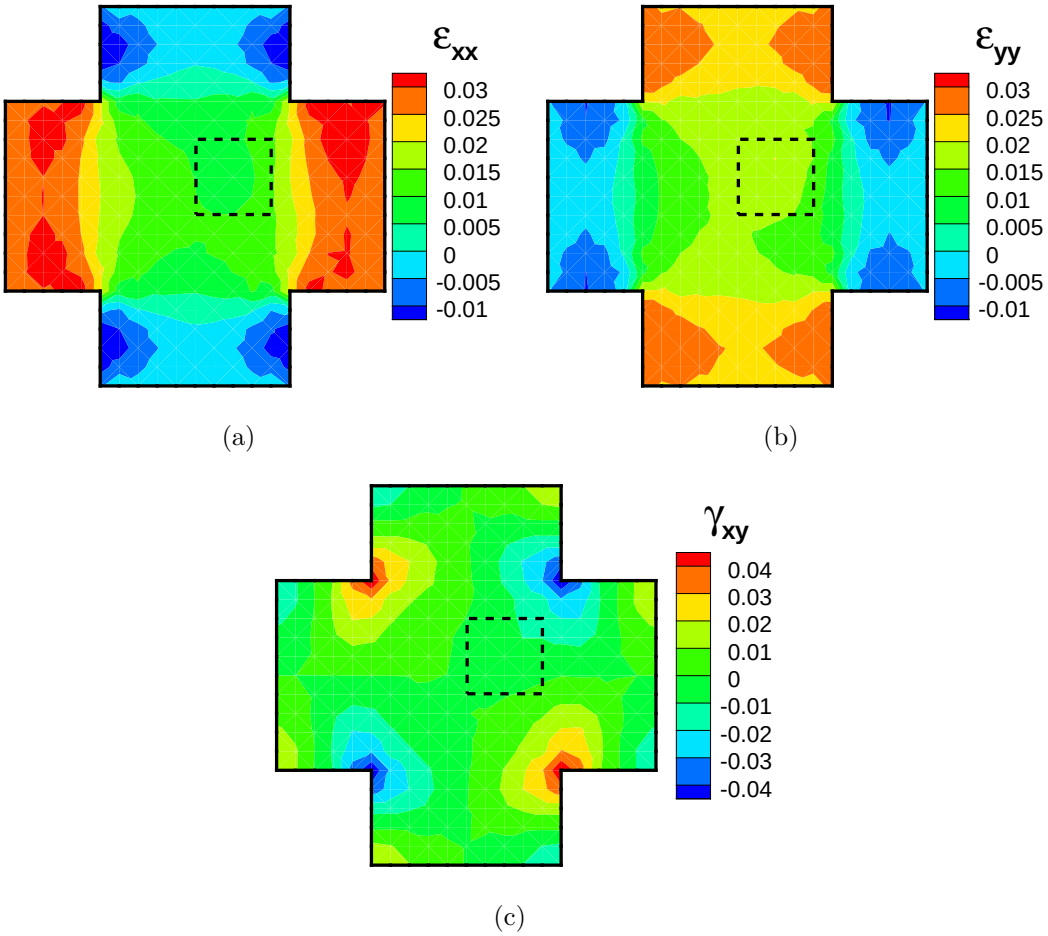

Figure 3.2: Strain reponse of the linear orthotropic test with the inclusion region shown in dashed lines. (a) ε_{xx}, (b) ε_{yy}, (c) shear strain γ_{xy},

Nodal displacements and the total normal force at each arm computed from the forward problem simulation were passed to GAIM. The basic scoop-and-trim algorithm was used to divide the domain into subdomains and determine the material properties of each subdomain. Figure 3.3 shows snapshots of solved partitions and the unsolved domain remaining at various steps of the processing. After the four boundary partitions were solved, one pass of scoop followed by trim was sufficient to partition the entire domain. The final partitioned domain is shown in Fig. 3.4(a) where the 18 partitions are numbered according to the order in which they were created. The evaluated six C_{ijkl} parameters of each partition are shown in Fig. 3.4(b) along with the input values (dotted lines).

The first 17 partitions belong to the cruciform material outside the box and the last partition exactly overlies the square box region of the inclusion. All the evaluated C_{ijkl} parameters of all partitions are identical with the input values. Hence GAIM successfully identified the anisotropic parameters and the region of material difference based only on the strain field and boundary forces from a single equibiaxial stretch test with no *a priori* specification of partitions. A better partitioning could have been found if the partitions with identical C_{ijkl} values were merged. Partitions 1–17 could have been combined into one giant, homogeneous partition. Hence there is scope for improvement in the partitioning method.

Eigentensor analysis for each of the materials correctly identified the principal directions at 90° and 0° for the materials outside the box, and at 30° and −60° for the material inside the box. The alignment map (Fig. 3.4(c)) shows the distinct difference in the anisotropy direction between the material inside and outside of the box. The low value of degree of anisotropy ($r_{GAIM} = 0.21$) shows that all the materials are nearly isotropic. The map of Kelvin moduli (Fig. 3.4(d)) shows that all regions have a uniform stiffness of 345 kPa. This number is larger than the maximum C_{ijkl} values in two perpendicular directions (190, 280 kPa) since it is an eigenvalue measure of the elastic tensor C. It is important to note that despite no regional change in stiffness GAIM was able to detect a different material inside the box which would not be perceptible for conventional methods that evaluate only the regional change in stiffness.

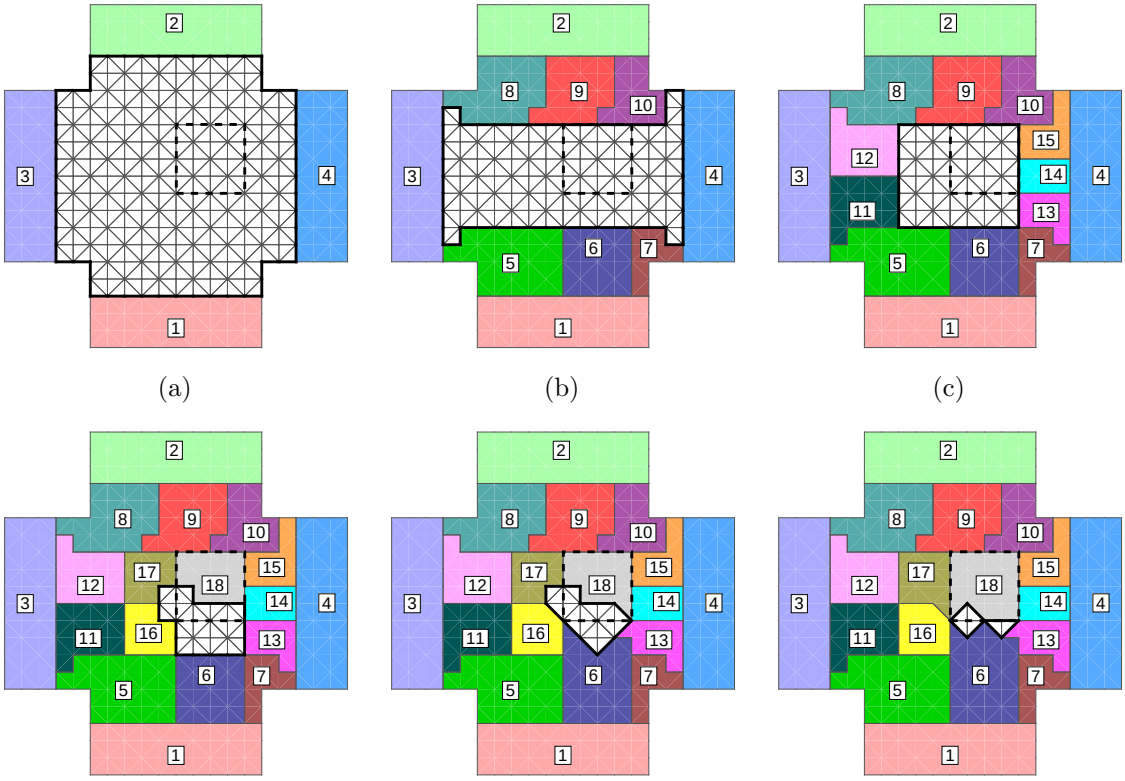

Figure 3.3: Snapshots from various stages of partitioning. Thick solid lines represent the current boundary of the unsolved mesh, shaded regions with numbers are the solved partitions numbered according to order of creation, the square box with thick dashed lines is the location of the inclusion. (a) After step 1 of the algorithm, all partitions at the grip boundaries are solved and removed. (b) Resultant forces on the current boundary allow scooping partitions starting from the boundary nodes. (c) The unsolved domain is continually shrunk. Partitions have been formed and solved at all the nodes on the original boundary leading to a boundary front that advances inwards. (d) Further partitions are solved and removed. Partition #18 is an incomplete portion of the inclusion. Candidate partitions that contain elements from both the sample and inclusion have large error residuals and will not be accepted as the method ignores these choices and probes the remaining list of nodes on the current boundary. (e) When no further partitions can be scooped from the current boundary the trim operator is invoked. This checks if elements at the boundary can be donated to solved neighbors and trims the boundary. (f) Snapshot before the last set of trims. The trim is continued until no more elements on the current boundary can be donated to neighboring solved partitions. In this case the trim continues and solves the entire mesh.

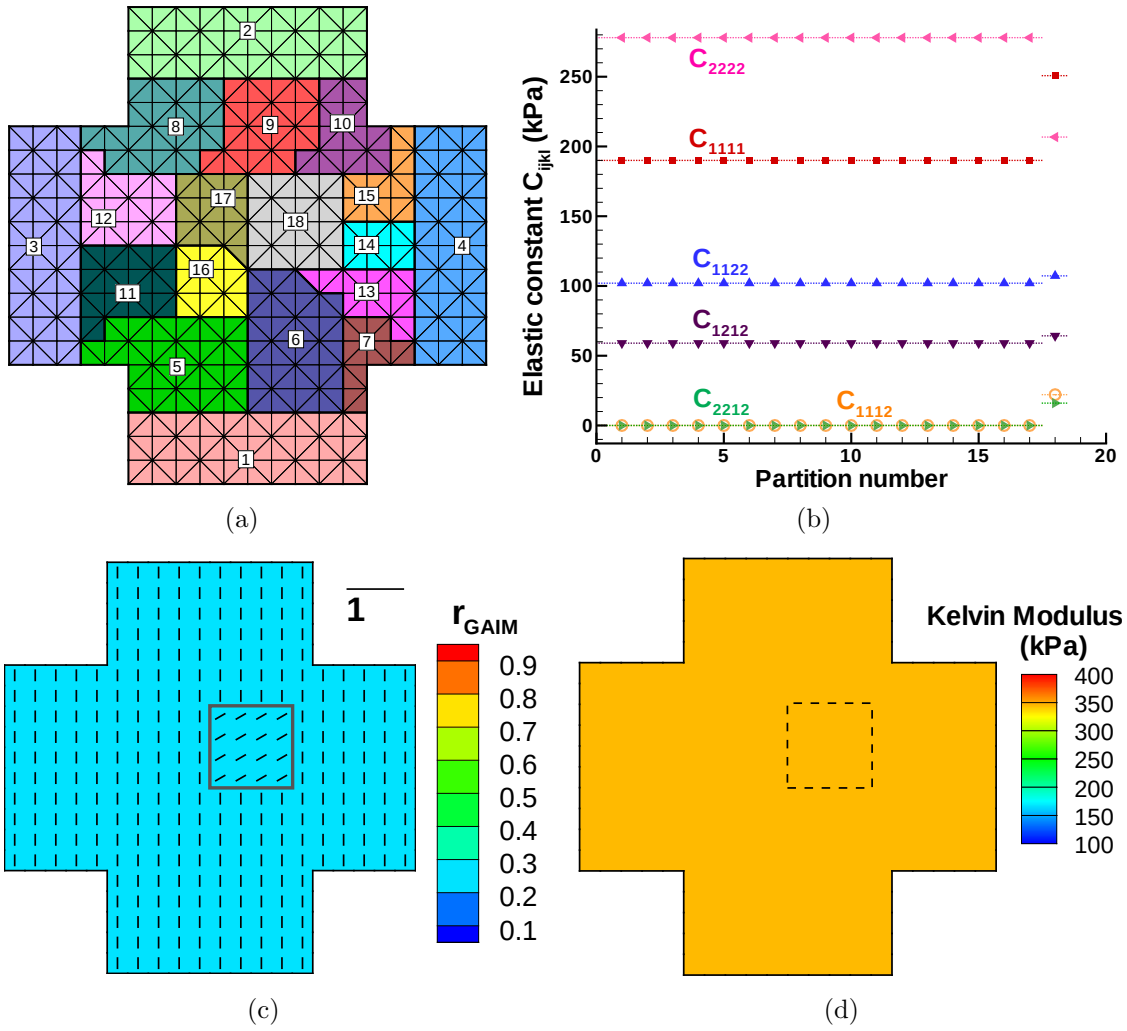

Figure 3.4: GAIM results for the linear, orthotropic test. (a) Final partitions produced by GAIM with the number indicating the order in which they were made; (b) C_{ijkl} values (symbols) for each partition compared with input data (dotted lines); (c) Alignment map showing the major anisotropy direction (vectors) and degree of anisotropy (contour). There is a distinct change in the anisotropy direction inside the box but the degree of anisotropy is constant everywhere ($r_{GAIM} = 0.21$). The low value of anisotropy indicates that all regions are nearly isotropic; (d) Kelvin modulus map shows that all regions have a uniform stiffness value of 345 kPa.

3.3 Nonlinear, Homogeneous Fibrous Tissue Sample

Having been verified for the linear orthotropic case, the GAIM method was tested on a nonlinear model applicable to fibrous soft tissues. Structural models that use the sum of fiber contributions for a distribution of fibers are popular in representing the complex mechanical behavior of soft tissues. We have developed a closed-form constitutive model for planar fibrous soft tissues, which is presented at greater length in §5.2. Here, we provide a brief summary of the model which is used to generate data from simulated experiments. The model assumes that the fibers in the tissue can be represented by the bidirectional von Mises distribution:

$$f(\theta, \kappa, \mu) = \frac{1}{\pi I_o(\kappa)} \exp\left(\kappa \cos\left[2\theta - 2\mu\right]\right) \quad \theta \in [0, \pi) \tag{3.3}$$

where κ is a concentration parameter, μ is the preferred direction and I_o is the modified Bessel function of first kind and zeroth order. The fiber distribution is uniform and represents isotropy when κ is zero. As κ becomes larger the distribution becomes more narrow and represents more alignment of fibers. For the constitutive relationship we use an exponential stress-strain law [50] to relate the fiber stretch-ratio λ_f to the 2nd Piola-Kirchhoff stress S_f by:

$$S_f = A\left(\exp\left[B(\lambda_f^2 - 1)\right] - 1\right) \tag{3.4}$$

where A and B are constants representing the stiffness and degree of nonlinearity respectively. Integrating the stress for all contributions, one can obtain a closed-form solution for the 2nd Piola-Kirchhoff stress and the tangent moduli [51]. This model was used to generate test data for a cruciform under equibiaxial stretch of 2.5%. The sample was set to be homogeneous with constants $A = 270$ kPa, $B = 3$, $\kappa = 2$ and $\mu = 60^\circ$ throughout. Green strains and principal stretches from the test are shown in Fig. 3.5. The major principal stretches at the four arms are towards the pull direction whereas at the center of the cruciform they are close to the vertical direction with negative slope. The nodal displacements and the total force at each arm were used as inputs for the inverse analysis. Although the material model was nonlinear, this experiment was used to test whether a linear model for the inverse method could capture the mechanical anisotropy in correlation to the input structural anisotropy.

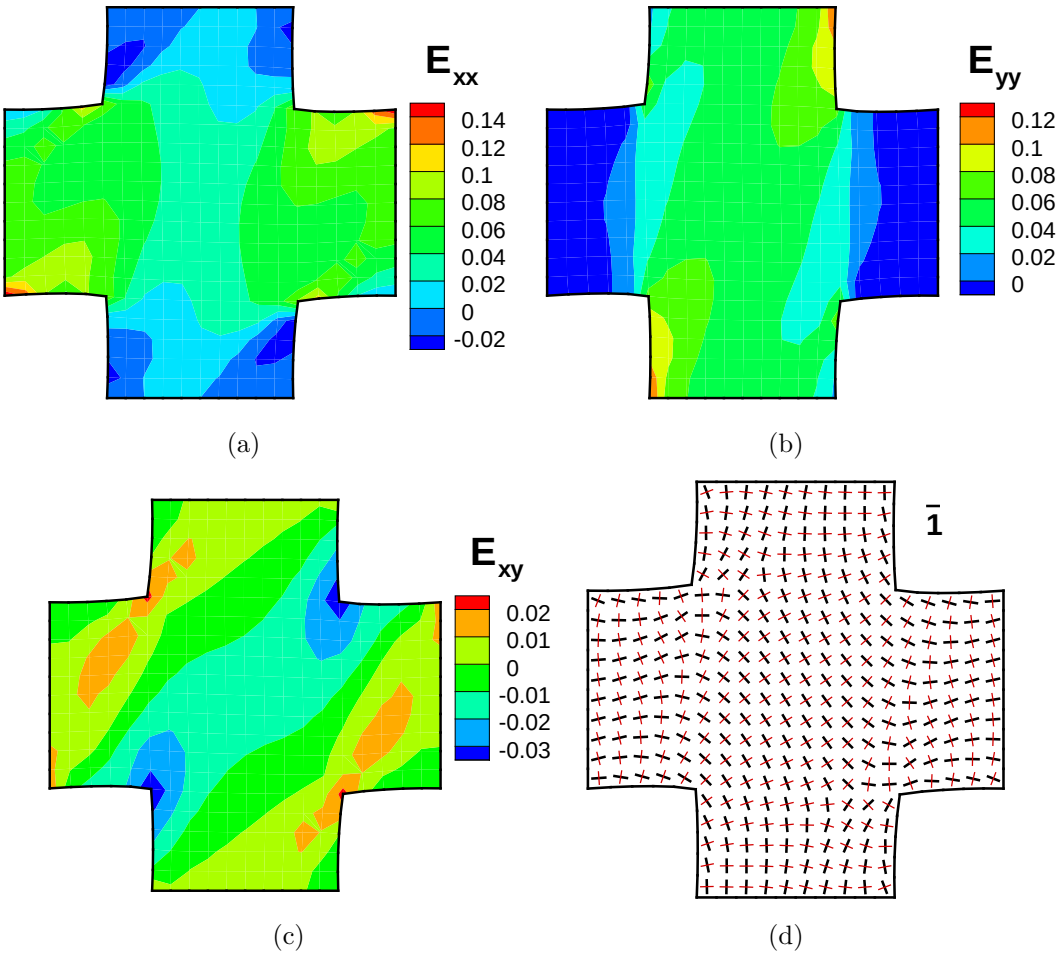

Figure 3.5: Strain and deformation response of simulated test on nonlinear fibrous tissue. (a) Green strain E_{xx}, (b) E_{yy}, (c) E_{xy}, (d) Principal stretches with major and minor directions in black and red respectively.

Two different inverse analyses were done using bilinear quadrilateral elements for the mesh. First, the entire domain was assumed to be homogeneous (no partitioning) and the inverse solver was used to determine its C_{ijkl} parameters. The resulting values and their 95% confidence intervals were

$$\begin{bmatrix} C_{1111} & C_{1122} & C_{1112} \\ & C_{2222} & C_{2212} \\ \text{sym} & & C_{1212} \end{bmatrix}_{\text{homog}} = \begin{bmatrix} 395 \pm 3 & 285 \pm 8 & 218 \pm 7 \\ & 1100 \pm 4 & 327 \pm 10 \\ \text{sym} & & 265 \pm 8 \end{bmatrix} \text{kPa} \qquad (3.5)$$

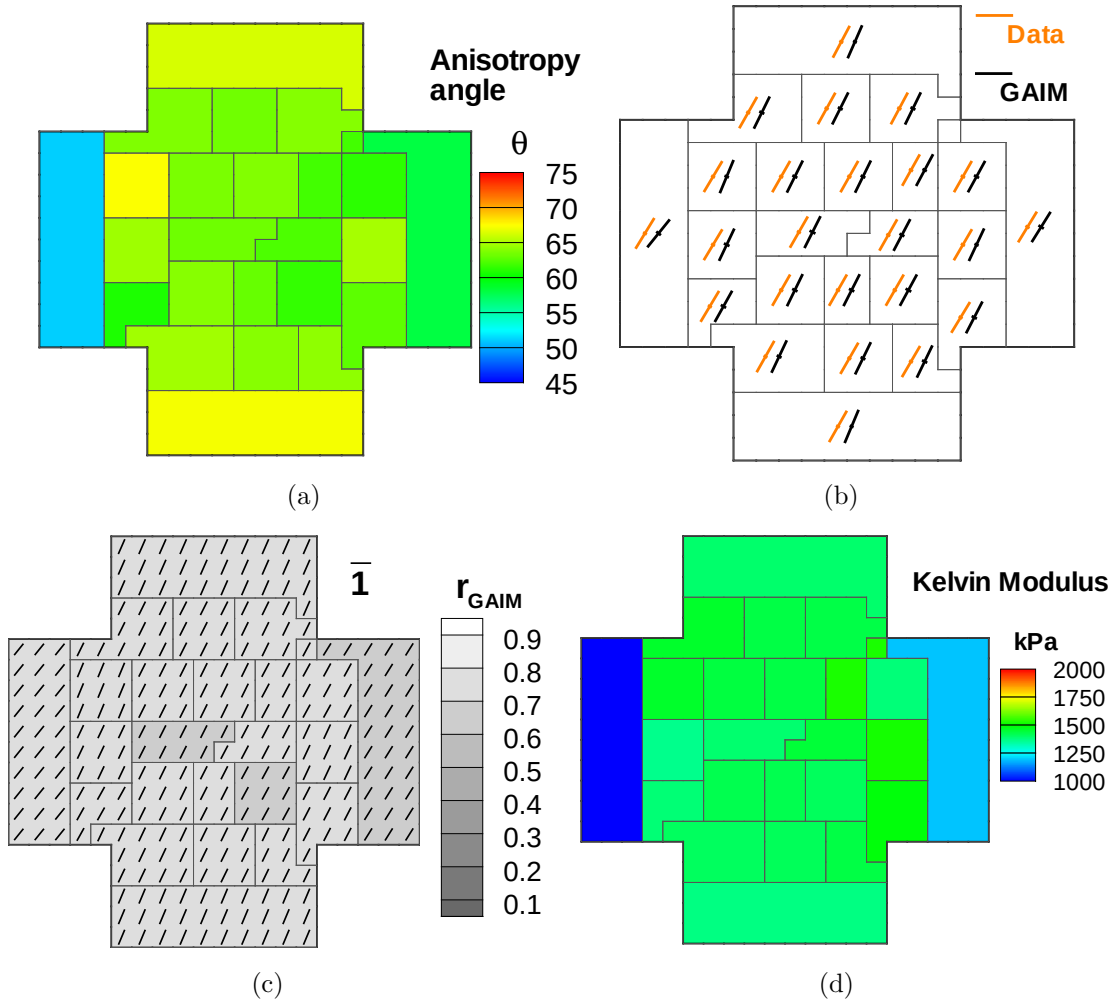

Figure 3.6: GAIM results for the simulated test on nonlinear fibrous tissue. (a) Anisotropy direction of each partition shows a range between 51–67°. Excluding the four boundary partitions this range is 61–67°; (b) Comparison of anisotropy vectors from input data and GAIM. Both the major and minor anisotropy vectors are plotted for each partition. Tangent moduli were averaged over each partition and the anisotropy vectors are computed from the eigentensors. There is excellent match between GAIM and input data, with little mismatch at some boundary partitions; (c) Alignment map showing the major anisotropy direction (vectors) and degree of anisotropy (contour). The entire cruciform is highly anisotropic with r_{GAIM} between 0.69–0.79; (d) Kelvin modulus map shows a range of values between 950–1525 kPa. Excluding the two horizontal arms this range is roughly uniform (1360–1525 kPa).

Eigentensor analysis resulted in principal directions at 62° and −28° for the largest Kelvin modulus of 1504 kPa and a corresponding r_{GAIM} value of 0.73 which indicates high anisotropy. In comparison to the input mean fiber alignment ($\mu = 60°$) these were highly satisfactory.

A second inverse analysis was done by letting the solver segment the domain. Results from this analysis are shown in Fig. 3.6 with the domain divided automatically into 24 partitions. Figure 3.6(a) shows the anisotropy plot with the partitions and their eigenvector angles. Except for a few partitions at the arms, all regions had anisotropy angles between 61–67°. From the forward problem, we averaged the tangent moduli over each partition and evaluated the major and minor anisotropy vectors of the strain eigentensor corresponding to the largest Kelvin modulus. These were compared (Fig. 3.6(b)) with the anisotropy vectors obtained by GAIM from the C tensor of each partition, and matched well. For the nonlinear model, since the tangent moduli are dependent on the deformation at each point, a heterogeneous deformation results in a heterogeneous behavior. The inverse analysis, with the domain divided into homogeneous partitions, evaluates an average material property over each partition. For our test case, the deformation was such that at the regions in the vicinity of the arms, the fibers are being stretched primarily along the direction of pull and hence oriented towards it, causing the rotation in angle noticed at the vertical and horizontal arms. The alignment map (Fig. 3.6(c)) shows little variation in alignment and degree of anisotropy over the sample with r_{GAIM} between 0.69–0.79. The contour of Kelvin modulus was nearly uniform (Fig. 3.6(d)) with a range of 1360–1525 kPa at all locations except the two horizontal arms where the combination of lower C_{2222} and higher C_{1111} lead to a smaller modulus estimate– 950 kPa (left arm) and 1200 kPa (right arm).

3.4 Discussion

GAIM was successful in evaluating the regional changes in mechanical anisotropy and stiffness in both the tests cases. In the linear, orthotropic test, the partitioning identified the exact location and shape of the inclusion in addition to the properties of all regions from a single experiment. The combination of multiple experiments, displacement field smoothing and confidence intervals will next be applied for real

experiments. In the second test, the linear GAIM model was sufficient to describe the regional anisotropy of nonlinear, fibrous tissue. Although the Green strain was typically close to 8% in many regions, the anisotropy estimates from GAIM were highly satisfactory. This is particularly striking since the C_{ijkl} values from GAIM are secant moduli of the linearized system and were fairly close to the tangent moduli computed from nonlinear fiber mechanics. Small errors were noticed at the partitions containing the arms. In these regions the tissue stretches primarily in the direction of pull, causing fibers to orient towards it. Due to little transverse deformation and discarding of the equations corresponding to the transverse force at the grips, transverse and normal moduli are evaluated to be lower and higher respectively. Since the tissue is much stiffer in the 2222 direction than in 1111 ($\mu = 60$, $\kappa = 2$), the effect on Kelvin moduli at the vertical arms is negligible, but is noticeable at the horizontal arms. It is important to be aware of the reduced accuracy of the method at the boundaries. Methods for addressing this problem will be presented in Chapter 4 where we validate GAIM with experiments on soft tissue analogs.

Chapter 4

Application of GAIM to Soft Tissue Analogs

This work was a part of the paper:

Identification of Regional Mechanical Anisotropy in Soft Tissue Analogs
Journal of Biomechanical Engineering, 2011 (in press)
Raghupathy, R., Witzenburg, C., Lake, S.P., Sander, E.A and Barocas, V.H.

4.1 Introduction

In chapter 3, we demonstrated the utility of GAIM in analyzing material anisotropy and heterogeneity for simulated data. In this chapter, we applied the method to *in vitro* model systems in a step-wise fashion: a homogeneous, isotropic PDMS sample, followed by a heterogeneous, isotropic sample, and finally a heterogeneous, anisotropic tissue analog. Table 4.1 classifies the samples tested according to isotropy and homogeneity. Cruciforms made from polydimethylsiloxane (PDMS) were used as isotropic test cases with separate samples for homogeneity and heterogeneity. More challenging tests were done on cell-compacted collagen cruciforms, which were prepared with predictable variation in regional anisotropic properties. Two collagen tissue equivalents with different regional architectures were tested to determine whether the method could reliably extract regional mechanical changes and distinguish between the two samples. Subsequent to biaxial mechanical tests on the samples, the recorded data

were processed and input to GAIM. The resulting alignment and stiffness maps were compared against known measurements, and the method was evaluated for its accuracy, reliability, and potential to quantify regional anisotropic material behavior on an intact tissue sample.

Sample	**Homogeneity**	**Isotropy**
Constant thickness PDMS	Homogeneous	Isotropic
Variable thickness PDMS	Heterogeneous	Isotropic
Fibroblast-compacted collagen cruciform	Heterogeneous	Anisotropic

Table 4.1: Soft tissue analogs classified according to isotropy and homogeneity

4.2 Polydimethysiloxane (PDMS) Samples

4.2.1 Sample Preparation

Homogeneous, isotropic samples (Fig. 4.1(a)) were prepared by casting polydimethylsiloxane (PDMS) gels in a cruciform mold. PDMS solution (*Sylgard ® 184 Silicone Elastomer Kit*; Dow Corning) was made by mixing the curing agent and base at a 1:10 ratio. Rice flour was added to the mixture to opacify the clear polymers for better visualization. The mixture was poured into an aluminum mold of cruciform geometry. The PDMS solution was left open to the atmosphere and allowed to cure overnight at room temperature. The final sample was approximately 15 mm square in the center with 7.5 mm wide arms, and it was 2.1 mm thick throughout.

Heterogeneous, isotropic samples (Fig. 4.1(b)) were prepared in a cruciform mold of identical geometry but with a square step in the center. As a result, this sample had a square depression (7 mm wide, 1.9 mm deep) in the center. Analyzed in 2D, the non-uniform thickness led to a compliant central region surrounded by a more stiff region.

4.2.2 Biaxial Mechanical Testing

Prior to mechanical testing, visual texture (Fig. 4.1) was added to the samples to facilitate strain-tracking. Graphite powder and spray paint were used for speckling.

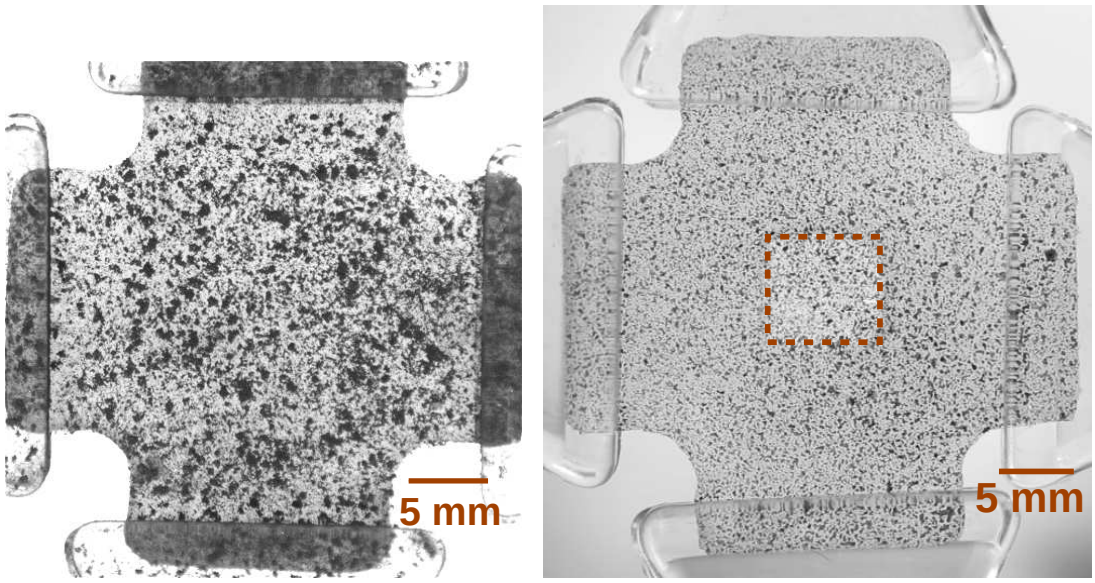

(a) (b)

Figure 4.1: Isotropic PDMS samples with visual texture added for strain tracking. (a) Homogeneous sample textured with graphite powder, (b) Heterogeneous sample textured with spray paint. The central square region is of one-tenth the thickness of surrounding material.

The samples were tested on an Instron planar biaxial testing unit. The biaxial testing protocol mentioned in Fig. 2.11 was performed with extension ratios of Table 4.2. Each loading and unloading cycle lasted 10 seconds.

Number of cycles and test	**% extension at arms (cyclic)**			
(1) Equibiaxial	7	7	7	7
(4) Two-adjacent arms	10.5	10.5	0	0
(4) Single arm	10.5	0	0	0
(2) Strip biaxial	7	0	7	0
(4) Three-adjacent arms	10.5	7	0	7

Table 4.2: Extension ratios for biaxial mechanical tests of PDMS samples. The column values for extension ratios are in clockwise order of the arms. The number in parentheses before the test represents the number of cyclic permutations of that test.

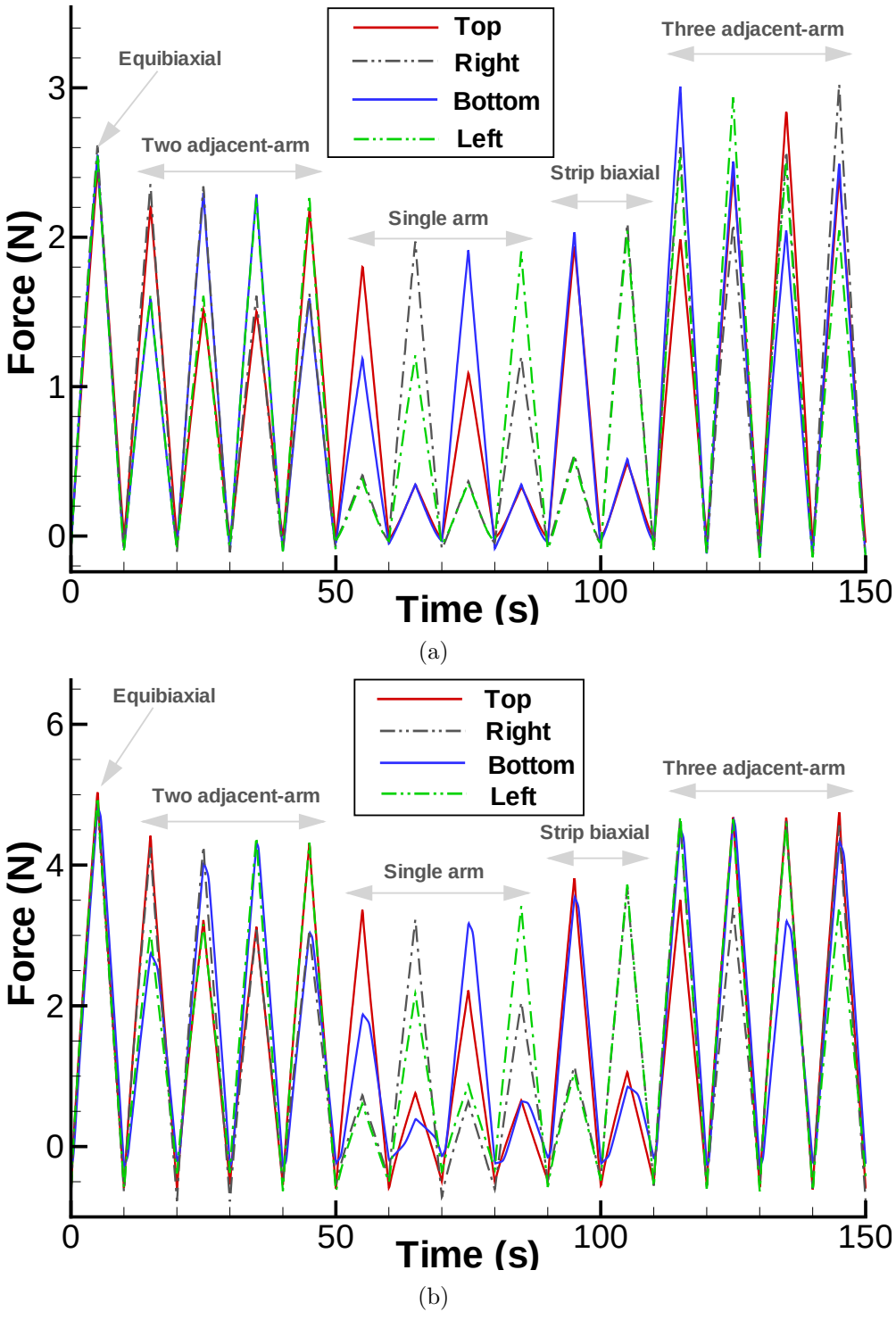

Figure 4.2: Force data from tests on PDMS samples are shown for all four arms. (a) Homogeneous sample, (b) Heterogeneous sample.

4.2.3 Data Processing

Figure 4.2 shows the force data from the load cells where the response is seen to be linear. Total forces applied over all loading cycles at all arms were calculated as shown in in the schematic in Fig. 2.15. Image sequences from each of the loading cycles were correlated, and displacement fields were obtained for all 15 tests. Figure 4.3 shows the Green strain for both samples. Strains in the homogeneous PDMS sample were uniform at the belly, with the junction of the arms carrying the maximum strains. In contrast, the heterogeneous PDMS sample had significant strain heterogeneity at the belly of the cruciform. The largest normal strains corresponded to the location of the thinner section.

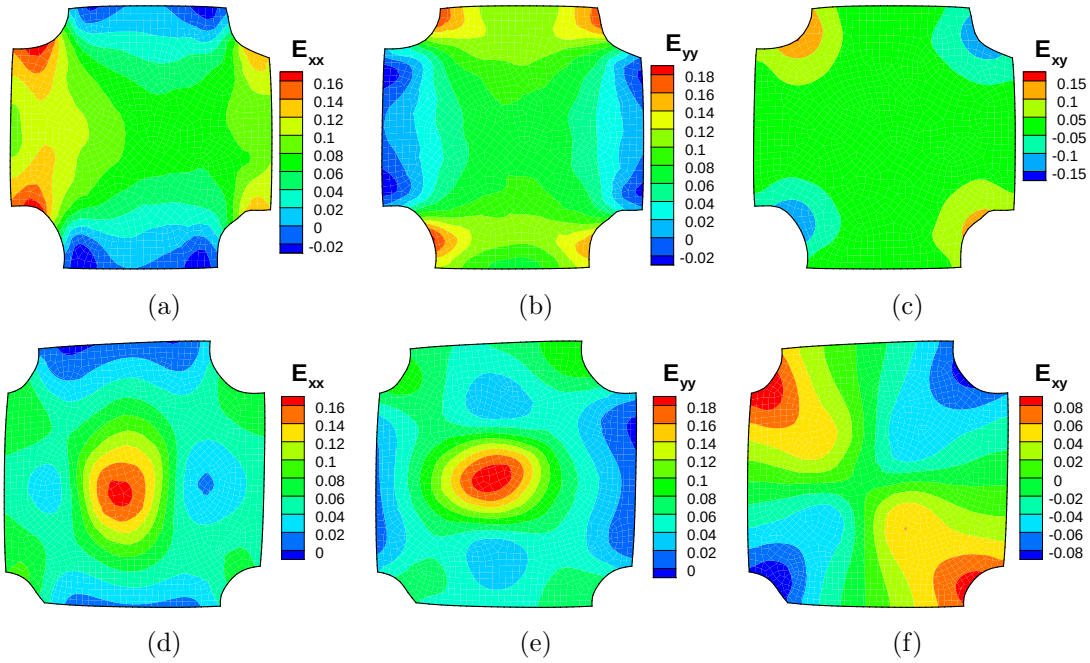

Figure 4.3: Strain response of homogeneous (a–c) and heterogeneous (d–f) PDMS samples for the equibiaxial test. All three components of Green strains are shown for each sample.

4.2.4 GAIM Results

We discuss the results from GAIM analysis on the processed data of both the samples in the following two subsections.

4.2.4.1 Homogeneous, Isotropic

Using the boundary forces and displacement fields from all fifteen tests on the PDMS sample of uniform thickness, GAIM automatically partitioned the domain into 30 regions. The alignment map (Fig. 4.4(a)) shows that partitions in the belly region of the cruciform are in the isotropic range ($r_{GAIM} \leq 0.3$) as expected. The higher anisotropy values in the arms (clockwise from top arm: $0.87, 0.85, 0.49, 0.45$) are believed to be due to the reduced accuracy in determining the transverse component of the elasticity tensor at the arms. Our load cells measure the forces only in the direction of pull, hence we must discard the equations corresponding to shear forces at the grips. The lack of transverse force data and the minimal transverse displacement in the arms combine to make the linear equation system for the arms poorly conditioned. As a result, the transverse components of C (e.g., C_{1122} and C_{2222} for an arm pointing in the 1 direction) are consistently underestimated. This is however, not a factor for the belly region where GAIM successfully identified the isotropy.

The contour of the largest Kelvin modulus (Fig. 4.4(c)) is nearly uniform (0.88–1.29 MPa) over the sample. In particular, the belly region has negligible variation (1.06–1.25 MPa) in modulus, indicating homogeneity. Hence, GAIM successfully identified the isotropy and homogeneity in the belly of the sample.

4.2.4.2 Heterogeneous, Isotropic

GAIM automatically partitioned the heterogeneous PDMS sample into 22 regions. The alignment map (Fig. 4.4(b)) shows the belly region to be isotropic ($r_{GAIM} \leq 0.3$) with an average anisotropy value of 0.14. The contour of Kelvin modulus (Fig. 4.4(d)) shows a range of values between 1.7–3.7 MPa over the entire sample. The central region corresponding to the thin section (box with dashed lines) was measured to be more compliant ($\sim$1.8 MPa) than the surrounding region at the belly ($\sim$3 MPa). The perceived relative stiffness ratio (0.6) is much larger than the thickness ratio of the sample (0.1). This apparent inconsistency is due primarily to through-thickness shear in the sample, which cannot be measured when the 3-D sample is imaged and analyzed in 2-D. A 3-D simulation of equibiaxial stretch on the sample performed in ABAQUS® yielded a strain ratio of 0.56 on the top surface, confirming that the

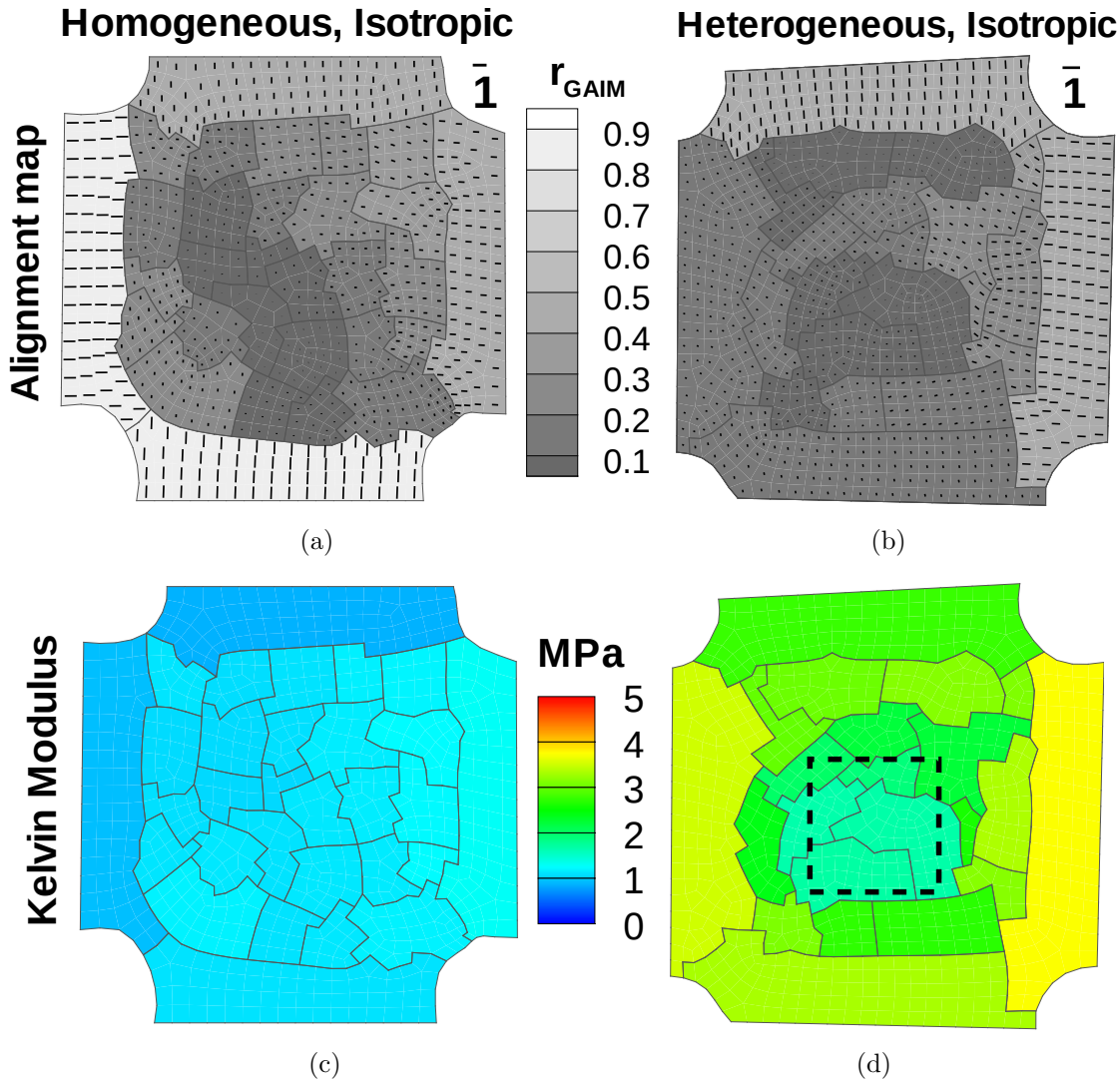

Figure 4.4: GAIM alignment maps (a,b) and Kelvin moduli plots (c,d) for isotropic PDMS samples. The length of vectors in (a,b) is the relative anisotropy in each partition. (a) Homogeneous sample shows low anisotropy values at the belly, indicating a largely isotropic sample. (b) Heterogeneous sample also shows low anisotropy, indicating an isotropic sample. (c) Homogeneous sample has uniform values in Kelvin modulus at the belly. (d) Heterogeneous sample shows a relatively compliant region at the center which corresponds to the location of the thin section (shown in dashed lines). The region inside the box has a Kelvin modulus of 1.8 MPa, while the region immediately outside the box is stiffer with 3 MPa.

apparent stiffness ratio is not the thickness ratio. The reduced 2-D strains on the top surface result in the sample being perceived as more stiff, leading to higher estimates of Kelvin modulus in comparison to the homogeneous case. Despite the artifacts of the 3-D deformation, GAIM successfully identified the isotropy of the sample and detected the region of low compliance with sufficient accuracy.

4.3 Collagen Tissue Equivalent Samples

4.3.1 Sample Preparation

Heterogeneous, anisotropic collagen tissue-equivalent (TE) cruciforms [4, 52] were formed by seeding neonatal human dermal fibroblasts (0.5×10^6 cells/mL) in a collagen gel-forming solution (initial collagen concentration of 1.5 mg/mL) as described in [53, 54]. Briefly, 2.2 mg/mL of bovine dermal collagen (Organogenesis, Canton, MA), 1M 4-(2-hydroxyethyl)-1-piperazineethanesulfonic acid (HEPES, Cellgro, Manassas, VA), 0.1M NaOH, 10X Modified Eagle's Medium (MEM, Sigma-Aldrich, St. Louis, MO), fetal bovine serum (FBS, HyClone, Logan, UT), and fibroblasts were mixed and cast into cross-shaped Teflon molds in which the fixtures needed for testing were already in place [54] so that all samples could be tested in the in-mold reference configuration. After gelation for 30 minutes at 37°C, high glucose DMEM (Invitrogen), supplemented with 10% FBS, 1% fungizone, 1% penicillin-streptomycin, 0.1% insulin, 50 μg/mL ascorbic acid (Sigma-Aldrich) and 1 ng/mL TGF-β, was added to each sample and was changed every 48 hours.

TE samples with an arm-width ratio of 1:0.5 were made and incubated for either 7 or 11 days (Figs. 4.5(a),4.5(b)). In contrast to a symmetric 1:1 cruciform where the center region is isotropic [53], the asymmetric 1:0.5 configuration produces moderate alignment in the center along the axis with wider arms. With longer incubation times we expect to observe increased alignment in the center due to continued cell-induced contraction and remodelling of the collagen network, resulting in samples with varying patterns of anisotropy. Since the collagen fiber-alignment of these samples can be confirmed by polarized light microscopy, they served as convenient tests cases for GAIM .

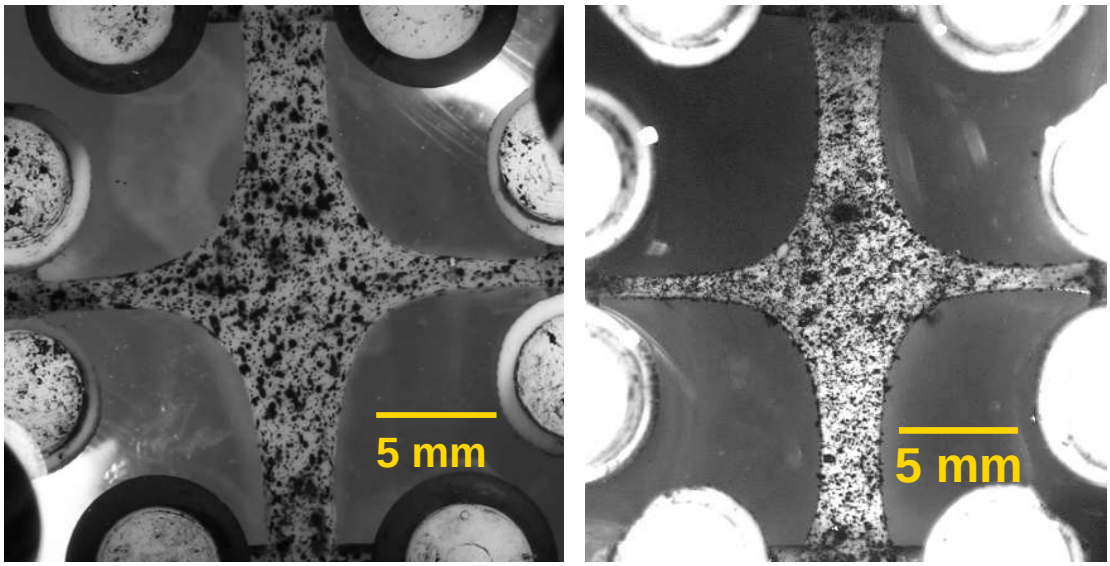

(a) (b)

Figure 4.5: Collagen tissue equivalent cruciforms of 1:0.5 arm width ratios. The cruciforms were cast in a Teflon mold of curved shape with glass rods at the ends and allowed to incubate. The cell-seeded gels wrapped themselves around the glass rods and compacted further resulting in the highly curved shape. Here the samples are shown with visual texture of Verhoeff's stain added for strain tracking prior to mechanical testing. (a) Sample incubated for 7 days, (b) Sample incubated for 11 days.

4.3.2 Polarized Light Microscopy (PLM)

Prior to mechanical testing, PLM [55] was used to quantify the localized direction and strength of fiber alignment in the collagen TE samples. PLM on the 7-day cruciform (Fig. 4.6a) showed high fiber alignment at the arms and boundaries as indicated by the large retardation values. The direction of alignment was along the arms and curved edges. The retardation values decreased from the boundaries towards the belly, where the sample was largely isotropic. In contrast, the 11-day cruciform (Fig. 4.6b) had a central region that was aligned with the wider arms. Two isotropic zones were present away from the center and towards the smaller arms (*cf.* [53]).

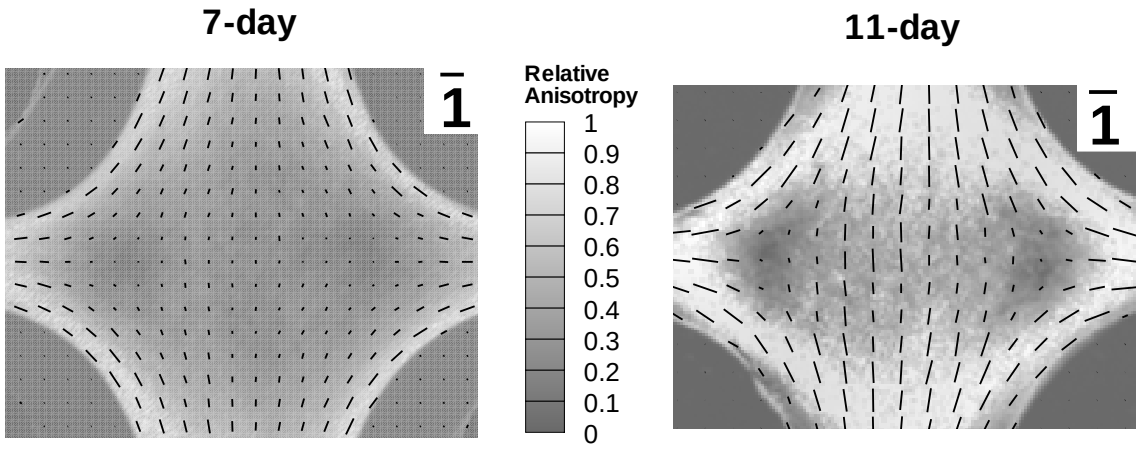

(a) (b)

Figure 4.6: Polarized light alignment maps for 1:0.5 collagen TE incubated for 7 and 11 days shows variation in sample anisotropy from isotropic to completely aligned. Retardation from PLM is a measure of the strength of fiber alignment (high retardation values indicate high alignment). The gray level shows the normalized retardation from PLM, and the vectors indicate the direction of alignment with vector lengths corresponding to the normalized retardation value. (a) 7-day sample shows high alignment at arms and curved ends while most of the belly is close to isotropic. (b) 11-day shows moderate alignment in center along the wide axis, two isotropic regions offset from the center, and strong alignment at arms and curved ends.

4.3.3 Biaxial Mechanical Testing and Data Processing

Number of cycles and test	**% extension at arms (cyclic)**			
(9) Preconditioning	7.5	7.5	7.5	7.5
(1) Equibiaxial	7.5	7.5	7.5	7.5
(4) Two adjacent-arms	11.25	11.25	0	0
(4) Single arm	11.25	0	0	0
(2) Strip biaxial	7.5	0	7.5	0
(4) Three adjacent-arms	11.25	7.5	0	7.5

Table 4.3: Biaxial mechanical test protocol for collagen TE samples. The column values for extension ratios are in clockwise order of the arms. The number in parenthesis before the test represents the number of cyclic permutations of that test. The 11-day sample was tested on a previous version of the GAIM protocol and did not undergo the strip-biaxial and three adjacent-arm tests.

Verhoeff's stain was added to the sample to provide visual texture for strain-tracking during mechanical testing. The samples were tested on an Instron planar biaxial testing unit while immersed in phosphate buffered saline (PBS) at room temperature. After a pre-load (0.01 N) had been applied to each of the four arms, the samples were pre-conditioned by nine equibiaxial stretch tests of 7.5% stretch and then loaded equibiaxially followed by cyclic combinations of asymmetric stretches holding one or more arms and stretching the others. Table 4.3 shows the extension ratios at each arm for the GAIM testing protocol that was run.

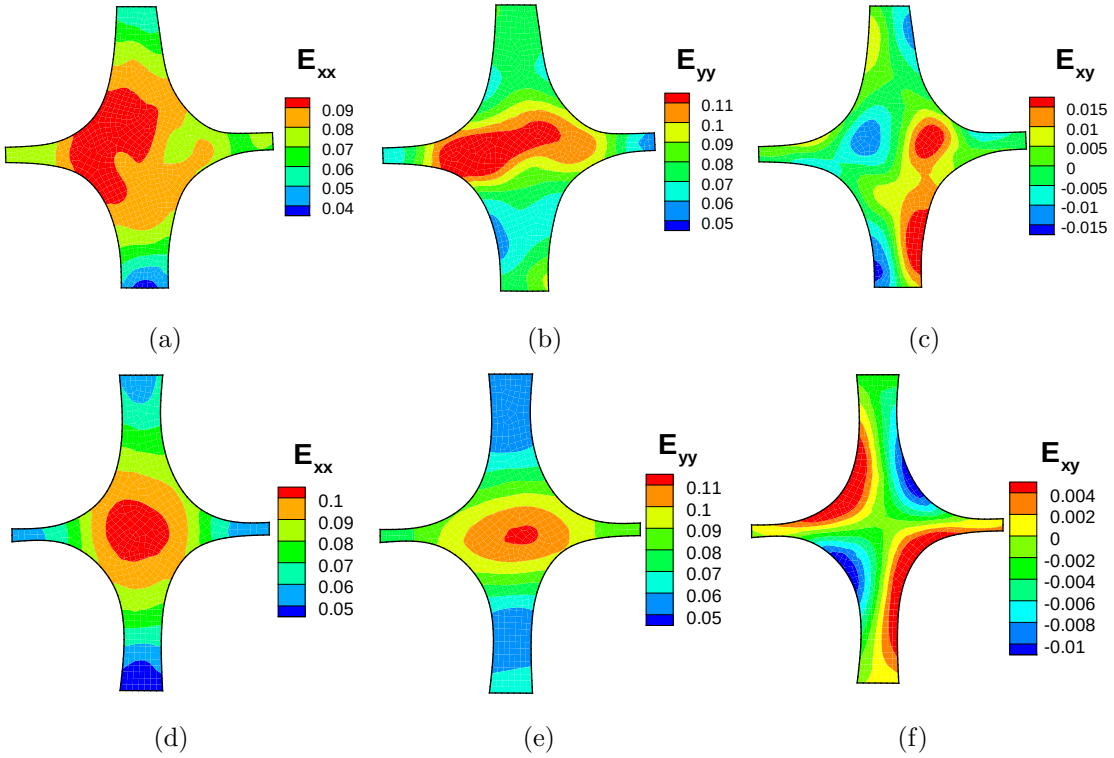

Figure 4.8: Strain response of cell-compacted collagen cruciform showing all three components of Green strains from the equibiaxial test. (a–c) 7-day sample, (d–f) 11-day sample.

4.3.4 Data Processing

Image sequences of the samples corresponding to the loading curves were correlated to obtain displacement and strain fields. Figure 4.8 shows the Green strain components for the equibiaxial test of both samples which have different patterns of strain hetero-

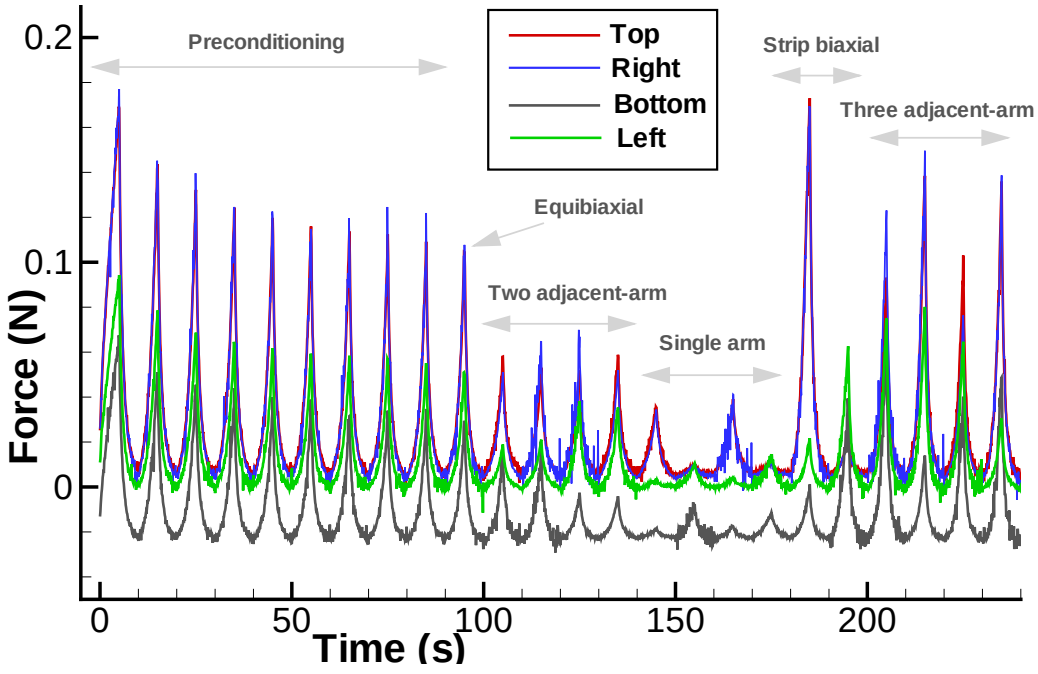

(a)

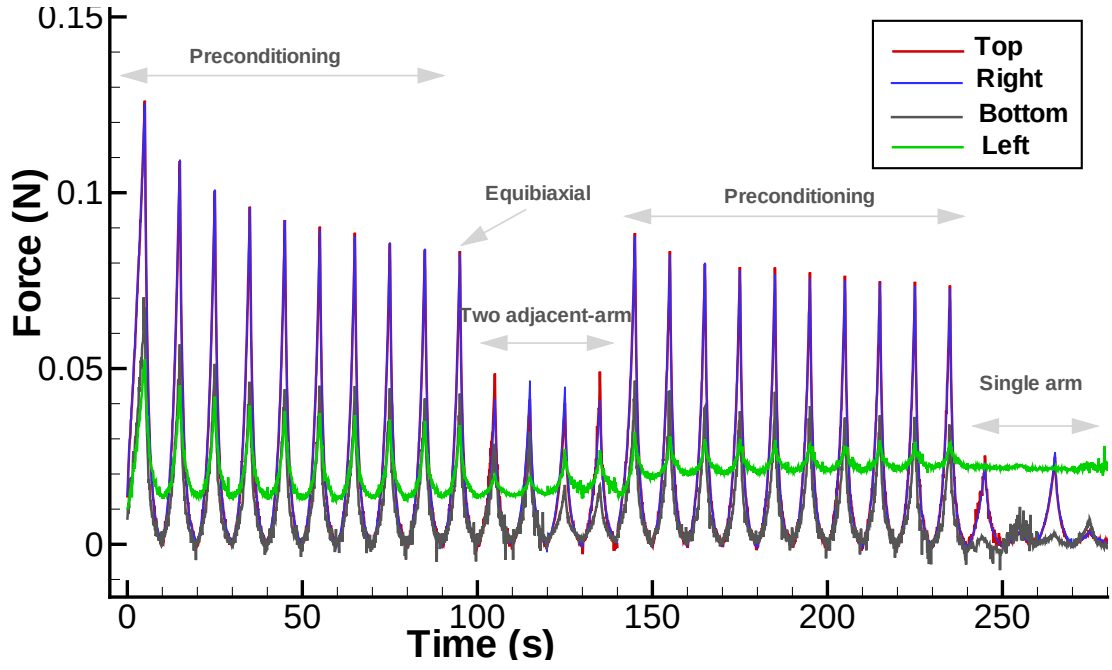

(b)

Figure 4.7: Force data for all four arms from tests on collagen cruciform samples are shown. (a) 7-day sample with preconditioning cycles followed by 15-test GAIM protocol, (b) 11-day sample with preconditioning cycles followed by 9-test GAIM protocol with an extra set of 10 preconditioning cycles between the two-adjacent-arm tests and single-arm tests.

geneity. Force data from the grips are shown for both samples in Fig. 4.7. There were slight differences in the testing protocol run on both samples. For the 7-day sample, a total of 15 tests were performed (Fig. 2.11). The 11-day sample was prepared from a different batch and tested earlier with an older version of the GAIM protocol where the strip biaxial and three adjacent-arm tests were not included. Each loading and unloading cycle lasted 10 seconds. The loads on each axis were not zeroed before testing, and hence some loading curves start below others in Fig. 4.7. Nonlinearity and noise in the force response was observed. The noise was smoothed by fitting the force data to cubic or quartic polynomials. The force curve on the left arm of the 11-day sample (Fig. 4.7(b)) drifted as the test progressed. Its magnitude was much smaller than the forces on the other arms. The second preconditioning set of cycles between 140–240s in Fig. 4.7(b) had little change in forces compared to those between 0–90s. This suggests that instead of preconditioning before every test of the GAIM protocol to ensure repeatability, it is sufficient to run the multi-test protocol continuously after the initial preconditioning cycles.

4.3.5 GAIM Results

GAIM automatically partitioned the domains and generated the alignment maps shown for the belly region in Figs. 4.9(a) and 4.9(b). Similar to alignment maps from polarimetry, the contour shows the anisotropy evaluated from Eq. 2.30, and the vectors show the alignment direction with lengths scaled according to the anisotropy value. The alignment map for the 7-day cruciform showed that the arms and curved edges were highly aligned in comparison to the center region, matching the general trend in regional changes in alignment observed in the polarimetry data, but with sharper changes in the anisotropy values at regional boundaries. GAIM also predicted well the alignment in the 11-day cruciform, including moderate alignment along the wider axis and two regions of isotropy in the center region.

Within the first few days of culture, the fibroblasts compacted the collagen gels and significantly reduced both sample volume and thickness by day 11. While the 11-day sample had 27% less area (measured from images) than the 7-day sample, we were not able to reliably detect differences in sample thickness between them. Hence, we report the largest Kelvin modulus expressed as a surface tension for both samples

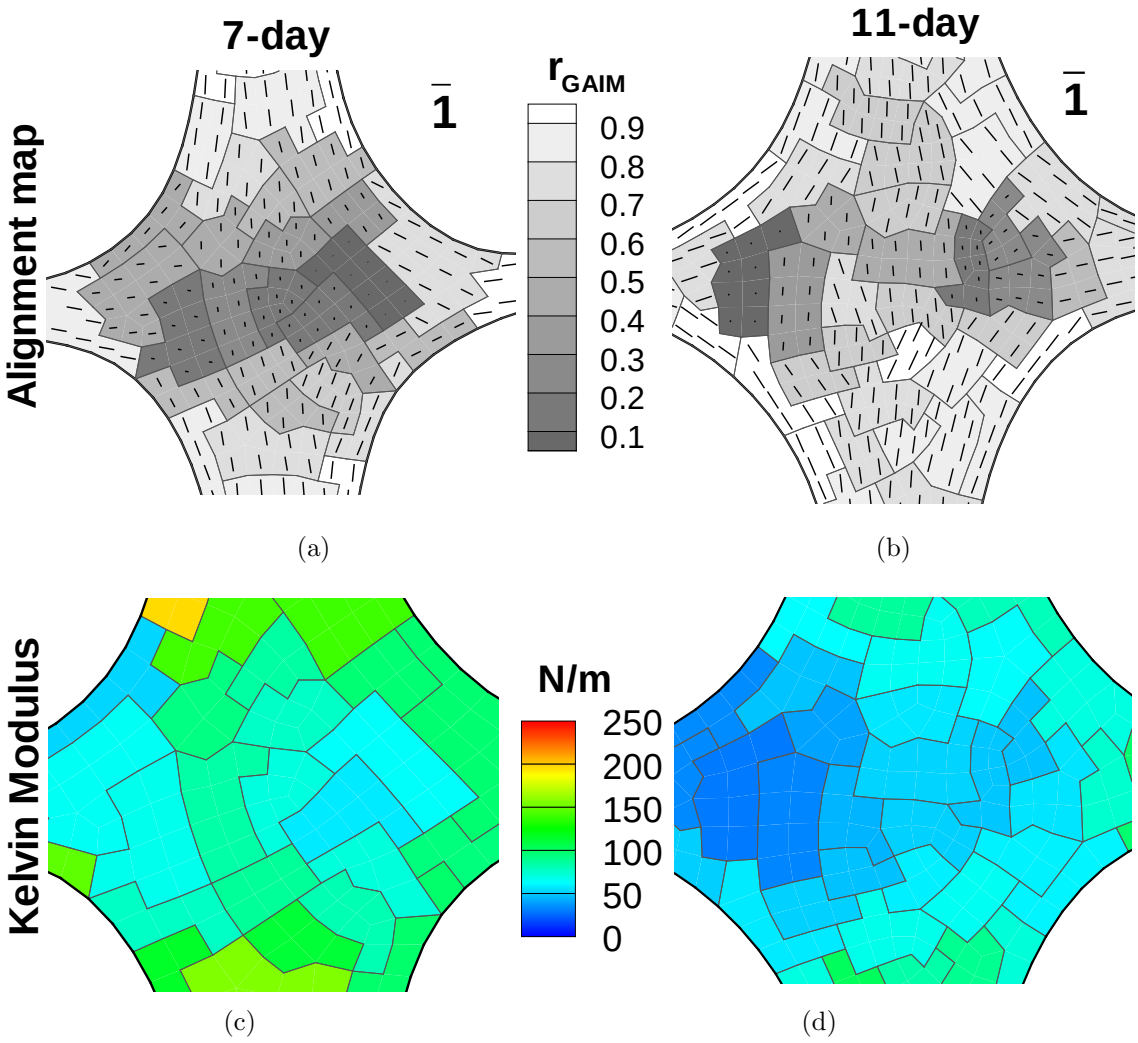

Figure 4.9: GAIM alignment maps and Kelvin modulus plots for 7-day and 11-day TE samples. The alignment maps from GAIM are indicative of the mechanical anisotropy of all elements in each partition. Alignment map for 7-day (a) and 11-day (b) samples show similar patterns to polarized light data, namely a large isotropic region for the 7-day, and increased alignment at 11-days. (c) Kelvin modulus (surface tension) plot for 7-day sample shows a range of values from 50–160 N/m at the belly. (d) Kelvin modulus (surface tension) for 11-day sample are evaluated to be within 30–85 N/m at the belly.

(Figs. 4.9(c),4.9(d)). Modulus values at the belly ranged from 50–160 N/m for the 7-day sample, and 30–85 N/m for the 11-day sample. While the large apparent reduction in modulus with increasing compaction time is unexpected, we believe that it is possibly due to sample environment variability since the samples were prepared

from different cell batches and tested with different protocols. The lowest Kelvin modulus values for the 11-day sample were observed in the left arm (Fig. 4.9(d)) and may have been a result of the low forces mentioned earlier.

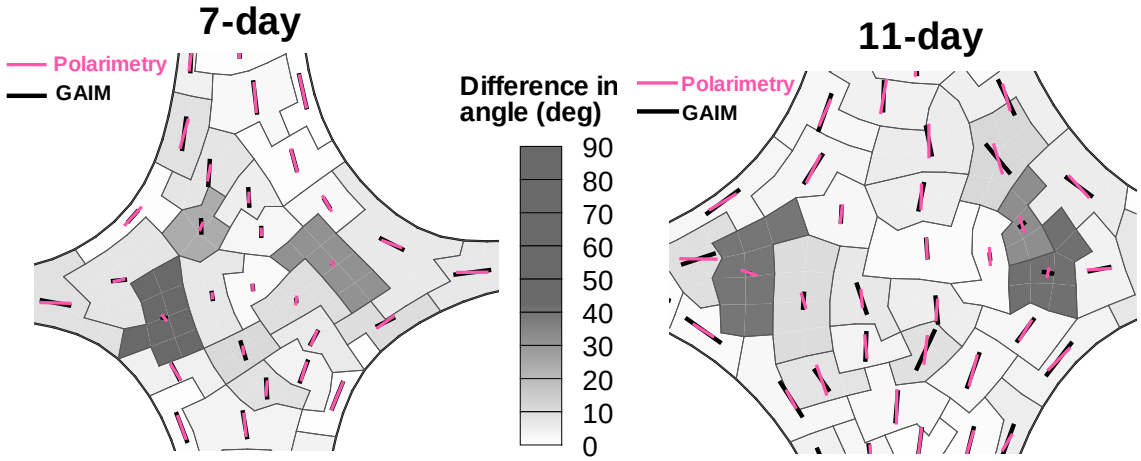

(a) (b)

Figure 4.10: Comparison of alignment maps generated by the model (GAIM) and the experiment (PLM) for 7-day and 11-day TE samples. The retardation and fiber alignment data from PLM were vector-averaged over each partition. The contour in the figures show the magnitude of difference in alignment angles between GAIM and PLM. The vectors indicate the relative anisotropy with the length given by the value of r_{GAIM} and averaged retardation (for PLM) in each partition. The length of the vectors in the legend indicate the maximum anisotropy of 1. There is excellent match between the alignments from model and experiments. The regions with large differences in angles correspond to largely-isotropic partitions for which there are no preferred directions and hence the errors can be discounted.

Figures 4.10(a) and 4.10(b) show the comparison between the alignment map predicted by GAIM and the measured values from PLM. The retardation and alignment directions from PLM were vector-averaged for each partition and the contour in the figures show the magnitude of the difference in angles between GAIM and PLM. Partitions with large error in angle corresponded to regions that were isotropic and hence had no preferred directions. Excluding these partitions, the mean error in angle at the belly was 5° and 8° for the 7-day and 11-day samples, respectively.

4.4 Discussion

Results from the tests on soft-tissue analogs shown in this chapter demonstrated that GAIM was successful in identifying regional differences in anisotropy from full-field displacements and boundary forces obtained from multiple biaxial extension tests. Tests on PDMS samples demonstrated the performance of the method on isotropic materials with uniform and non-uniform properties. The region of material difference was identified with sufficient accuracy although three-dimensional motion artifacts could not be captured by our 2-D model.

Due to the unavailability of shear force measurements from the load cells, the method has reduced accuracy at the grip boundaries. Load cells that record shear and normal forces as well as moments can be used to improve the accuracy. Even then, the arms experience little transverse deformation, so it may be necessary to truncate the domain of analysis. With symmetric sample shapes, it may be difficult to impose shear at the center of the sample, which would lead to poor estimates for the shear modulus at the center. Using asymmetric shapes and clamping the sample with slight rotation in the arms could help offset the potential problem and will require investigation.

Tests on fibroblast-remodeled collagen cruciforms indicated a strong correlation between local structural anisotropy (measured by polarized light microscopy) and the local mechanical anisotropy. The method's success in capturing changes in anisotropy associated with growth and remodelling is highly satisfying. Despite considerable noise and nonlinearity in the force response, it is encouraging that the linear model was able to identify the degree and directions of anisotropy. The results demonstrate the potential to quantify regional anisotropic material behavior on an intact tissue sample. In tissues where direct measurements of structure are not feasible, GAIM could be used to identify major anisotropy directions and the degree of anisotropy from the tissue response.

Chapter 5

Extension to Nonlinearity with a Structural Model for Fibrous Soft Tissues

Part of this work was developed in the paper:

A Closed-Form Structural Model of Planar Fibrous Tissue Mechanics
Journal of Biomechanics, 2009, 42(10), pp. 1424-1428
Raghupathy, R. and Barocas, V.H.

5.1 Introduction

In previous chapters we have demonstrated that the linear model in GAIM was sufficient to extract regional anisotropic and stiffness quantities such as the preferred fiber orientation, degree of anisotropy and Kelvin modulus. While these quantities give valuable information about the mechanical and structural anisotropy, they cannot be directly applied to model the mechanical response of tissues exhibiting high nonlinearity. For instance, Kelvin moduli reported by GAIM are secant measures of stiffness and cannot give accurate stress predictions particularly for large deformations. However, once the regions of uniform anisotropic properties and their respective directions of alignment have been identified by GAIM, constitutive models applicable to soft tissues can be fit by nonlinear regression to the full set of measurements.

A major challenge in the mathematical description of soft tissue mechanics is the lack of an obvious choice of constitutive equation that can capture the complex architecture and nonlinear behavior of the tissue. In this chapter we present a structural model applicable to planar fibrous soft tissues. The simple, closed-form solution of the model makes it an attractive choice for characterizing soft tissues from biaxial extension tests. We also demonstrate that results from GAIM can be directly converted to estimates of some the model parameters, thus forming a nonlinear extension to the linear GAIM model.

5.2 Nonlinear Fiber Model for Planar Fibrous Tissues

We outline key aspects of the fiber model which is detailed in Ref. [51]. We adopt the popular approach [56–62] of using contributions from a continuous matrix and from a population of fibers with the constituents assumed to deform affinely with the macroscopic deformation and the stresses assumed to be additive. A continuous distribution function is used to represent the fiber population statistically. The continuous approach has the advantage that it applies to systems in which the fiber population is highly distributed with respect to direction, but the disadvantage is that the total stress from the population must be expressed as an integral rather than as a sum of a small number of values. We use the von Mises distribution

$$f(\theta, \kappa, \mu) = \frac{1}{\pi I_o(\kappa)} \exp\left(\kappa \cos\left[2\theta - 2\mu\right]\right) \quad \theta \in [0, \pi) \tag{5.1}$$

where κ is a concentration parameter, μ is the preferred direction of orientation and I_o is the modified Bessel function of first kind and zeroth order. As κ becomes large, f approaches a normal distribution with variance $1/(4\kappa)$, and as κ becomes small, f approaches a uniform distribution on the half circle, $f = 1/\pi$.

A critical feature of the structural approach is the transfer of constitutive description from the tissue level to the fiber level. That is, the model requires a constitutive equation for the fiber rather than for the tissue. An exponential form based on the Green strain of the fiber is a popular choice [50, 63] and used here as follows:

$$S_f = A\left(\exp\left[B(\lambda_f^2 - 1)\right] - 1\right) \tag{5.2}$$

where A and B are constitutive constants, S_f is the second Piola-Kirchoff stress in the fiber, and λ_f is the fiber stretch for a fiber aligned with angle θ, defined kinematically by

$$\lambda_f^2 = C_1 \cos^2(\theta - \alpha) + C_2 \sin^2(\theta - \alpha) \tag{5.3}$$

where C_1 and C_2 are the squared principal stretches, i.e., the eigenvalues of the Green deformation tensor $C = F^T F$, and α is the angle corresponding to the direction of the first eigenvector. Although other possibilities could be considered, the constitutive model of Eq. 5.3 was chosen because of its popularity and because of the simple closed-form integral that can be derived. Although the constants A and B do not have direct physical meaning, they capture the overall stiffness and nonlinearity of the fiber response respectively. Increasing A makes the fiber stiffer at all strains, and increasing B makes the fiber response more sharply nonlinear. It is further noted that in the limit of small strain ($\lambda_f \to 1$), Eq. 5.3 reduces to a linear response with modulus $2AB$.

Since the stress is the sum of all fiber stresses, and the fibers are assumed to be stretched affinely with the macroscopic deformation, the total second Piola-Kirchoff stress S_{ij} is given by

$$S_{ij} = \int_0^\pi \mathbf{e}_i(\theta)\, \mathbf{e}_j(\theta)\, S_f(\theta, C_1, C_2, \alpha)\, f(\theta, \kappa, \mu)\, d\theta \tag{5.4}$$

where $\mathbf{e}_i(\theta)$ is the i'th component of the unit vector in the fiber direction θ, S_f is the fiber stress defined by Eq. 5.3, and f is the von Mises distribution. The analytical evaluation of the integral in Eq. 5.4 is detailed in Ref. [51]. We present the final closed-form expressions for the stresses:

$$S_{11} = \frac{1}{2I_0(\kappa)} \left[k_0 \left(I_0(\gamma) + I_1(\gamma) \cos 2\delta\right) - A I_1(\kappa) \cos 2\mu\right] - A/2 \tag{5.5}$$

$$S_{22} = \frac{1}{2I_0(\kappa)} \left[k_0 \left(I_0(\gamma) - I_1(\gamma) \cos 2\delta\right) + A I_1(\kappa) \cos 2\mu\right] - A/2 \tag{5.6}$$

$$S_{12} = \frac{1}{2I_0(\kappa)} \left[k_0 I_1(\gamma) \sin 2\delta - A I_1(\kappa) \sin 2\mu\right] \tag{5.7}$$

where k_0, γ and δ are given by

$$
\begin{aligned}
k_0 &= A\exp\left[B\left((C_1+C_2)/2-1\right)\right] && (5.8)\\
k_1 &= \tfrac{B}{2}(C_1-C_2)\cos 2\alpha+\kappa\cos 2\mu && (5.9)\\
k_2 &= \tfrac{B}{2}(C_1-C_2)\sin 2\alpha+\kappa\sin 2\mu && (5.10)\\
\gamma &= \sqrt{k_1^2+k_2^2} && (5.11)\\
\delta &= \tfrac{1}{2}\tan^{-1}(k_2/k_1) && (5.12)
\end{aligned}
$$

5.2.1 Finite-Element Implementation

The four parameters for the fiber model A, B, κ, and μ are independent of deformation. The tangent stiffness tensor D_{ijkl} is obtained by taking the analytical partial derivative of the second Piola-Kirchoff stress S_{ij} with respect to Green strain E_{kl}

$$D_{ijkl}=\frac{\partial S_{ij}}{\partial E_{kl}} \tag{5.13}$$

With only minor symmetry ($D_{ijkl}=D_{ijlk}=D_{jikl}$) of tensor D, we report the final expressions for all the nine elements of the 3×3 matrix form of D as

$$
\begin{aligned}
D_{1111} &= \tfrac{k_0B}{2I_0(\kappa)}\left[I_0(\gamma)\left(1+\cos^2 2\delta\right)+I_1(\gamma)\left(2\cos 2\delta-\tfrac{\cos 4\delta}{\gamma}\right)\right] && (5.14)\\
D_{1122} &= \tfrac{k_0B}{2I_0(\kappa)}\left[I_0(\gamma)\sin^2 2\delta+I_1(\gamma)\tfrac{\cos 4\delta}{\gamma}\right] && (5.15)\\
D_{1112} &= \tfrac{k_0B}{2I_0(\kappa)}\left[I_0(\gamma)\sin 4\delta+I_1(\gamma)\left(2\sin 2\delta-\tfrac{2\sin 4\delta}{\gamma}\right)\right] && (5.16)
\end{aligned}
$$

$$
\begin{aligned}
D_{2211} &= D_{1122} && (5.17)\\
D_{2222} &= \tfrac{k_0B}{2I_0(\kappa)}\left[I_0(\gamma)\left(1+\cos^2 2\delta\right)+I_1(\gamma)\left(-2\cos 2\delta-\tfrac{\cos 4\delta}{\gamma}\right)\right] && (5.18)\\
D_{2212} &= \tfrac{k_0B}{2I_0(\kappa)}\left[-I_0(\gamma)\sin 4\delta+I_1(\gamma)\left(2\sin 2\delta+\tfrac{2\sin 4\delta}{\gamma}\right)\right] && (5.19)\\
D_{1211} &= \tfrac{1}{2}D_{1112} && (5.20)\\
D_{1222} &= \tfrac{1}{2}D_{2212} && (5.21)\\
D_{1212} &= 2D_{1122} && (5.22)
\end{aligned}
$$

The tangent matrix of D can be used in a finite-element setting with the incremental, linearized form of

$$\begin{Bmatrix} \Delta S_{11} \\ \Delta S_{22} \\ \Delta S_{12} \end{Bmatrix} = \begin{bmatrix} D_{1111} & D_{1122} & D_{1112} \\ D_{2211} & D_{2222} & D_{2212} \\ D_{1211} & D_{1222} & D_{1212} \end{bmatrix} \begin{Bmatrix} \Delta E_{11} \\ \Delta E_{22} \\ \Delta E_{12} \end{Bmatrix} \tag{5.23}$$

While matrix D is not symmetric in Eqn. 5.23, it is converted to a symmetric form by using Eqns.5.17,5.20–5.22 and choosing $2\Delta E_{12}$ instead of ΔE_{12}

$$\begin{Bmatrix} \Delta S_{11} \\ \Delta S_{22} \\ \Delta S_{12} \end{Bmatrix} = \begin{bmatrix} D_{1111} & D_{1122} & D_{1211} \\ & D_{2222} & D_{1222} \\ \text{symm} & & D_{1122} \end{bmatrix} \begin{Bmatrix} \Delta E_{11} \\ \Delta E_{22} \\ 2\Delta E_{12} \end{Bmatrix} \tag{5.24}$$

We have already presented results from the finite-element implementation of the fiber-based model in §3.3 where the strains and principal stretches for a cruciform sample with $A = 270$ kPa, $B = 3$, $\kappa = 2$ and $\mu = 60°$, and subject to equibiaxial stretch of 2.5% are shown in Fig. 3.5. The results show that the off-axis alignment of the fibers lead to skewing of the strain field. Cauchy stresses components and the principal stresses are shown in Fig. 5.1. It is observed that principal stresses (Cauchy) are smooth and symmetric.

Equations 5.5–5.12 can be viewed not as a fiber model per se but as a specialized constitutive model. The equations could be fit to experimental data using A, B, κ and μ as fitting parameters without making a specific claim that the equation represents an underlying fiber population. Such an approach would be similar to the Arruda-Boyce model and its variations [64, 65], which use a simple unit-cell representation of fiber mechanics where the model, although not a perfect description of the micromechanical environment, is able to describe a wide range of material responses with a relatively small number of parameters. The parameters in the current model represent four different effects: κ is the degree of anisotropy, μ the preferred direction, A the stiffness of the fiber, and B the nonlinearity of the fiber stress-strain response. The angle δ (Eqn. 5.12) and magnitude γ (Eqn. 5.11) represent the coupling between the fiber affine stretch and fiber population distributions. Specifically, the angle α (Eqn. 5.3), which depends solely on the macroscopic deformation and not on the

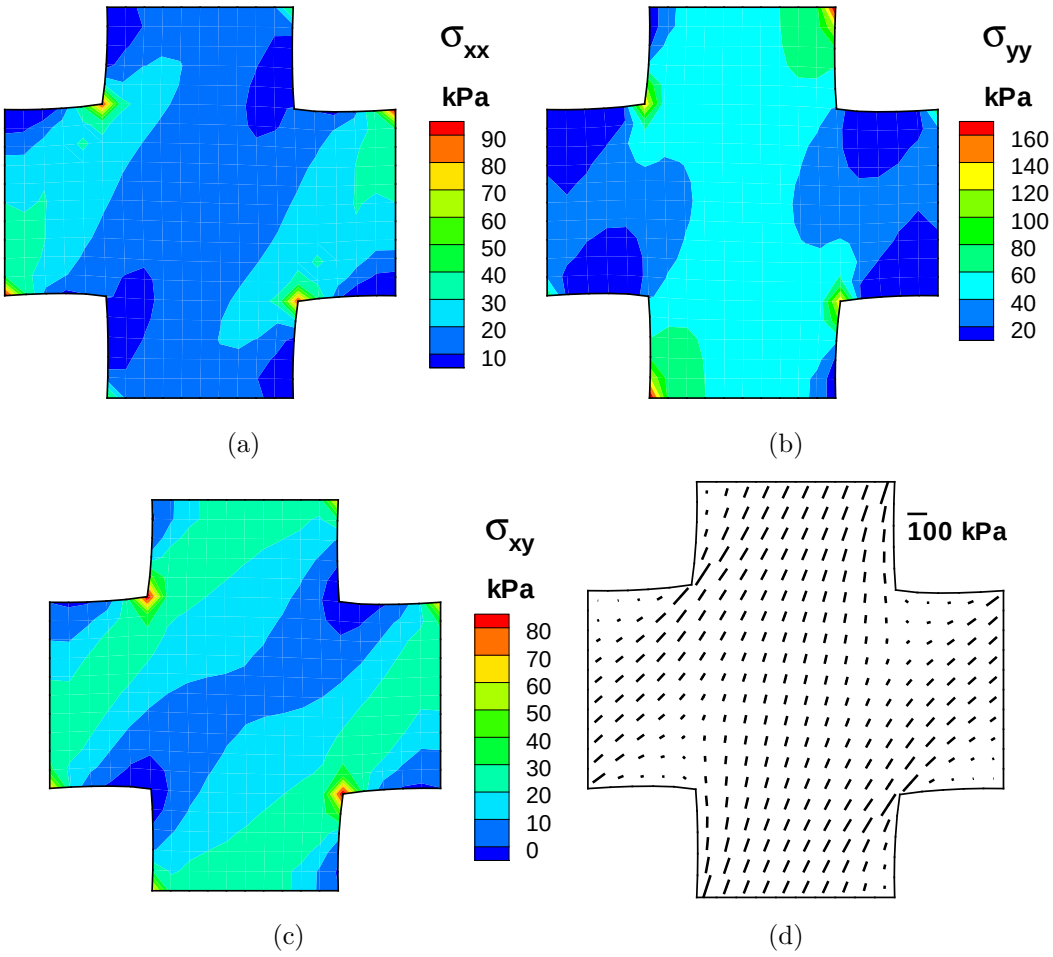

Figure 5.1: Stress response of simulated test on nonlinear fibrous tissue. The cruciform is stretch equibiaxially by 2.5%. (a) Cauchy stresses σ_{xx}, (b) σ_{yy}, (c) σxy, (d) Principal stresses (Cauchy).

fiber distribution, is the direction in which a fiber would be stretched the most by a given macroscopic deformation. The angle μ, in contrast, depends solely on the fiber distribution and not on the macroscopic deformation; it is the direction in which a fiber is most likely to be oriented. The angle δ depends on both the deformation and the distribution, and it is the direction that contributes most to the total stress.

The closed-form solution derived above provides the potential for more rapid solution of computational mechanics problems associated with fiber-population-based structural models. It is also important to recognize that the von Mises distribution does

not describe all data sets, so other options might need to be considered. Nevertheless, the commonness of the von Mises distribution and the potential for summation of multiple distributions is a strong point in favor of this model.

5.3 Application of the Model to Mechanical Characterization from Biaxial Experiments

The structural parameters of the model can be determined from optical imaging techniques such as light scattering [61, 66–68] by regressing κ and μ of the von Mises distribution to the measurements. The parameters A and B can be obtained from mechanical tests. For instance, biaxial extension tests can be performed on samples such that the loading directions correspond to the symmetry axes of the fiber population, which simplifies the calculation of S_{ij}. Parameters A and B can be regressed to fit the load-displacement data obtained.

If structural measurements are not available, or assumption of strain homogeneity in the loaded-sample is not valid, then a finite element model of the extension test can be used to estimate the four parameters by nonlinear regression. Briefly, a mesh of the sample geometry is created from an image of the test, an initial guess of parameters is made, and the test is simulated with grip displacements applied as boundary conditions to the finite element simulation. Grip forces from the simulation for the current choice of parameters are compared with the measured forces from experiments and the parameters are iteratively updated (e.g., Levenberg-Marquardt, Gauss-Newton [69]) to minimize the error in fit.

One advantage of the closed-form solution to the fiber model is that analytical expressions for derivatives of the optimization function with respect to the model parameters are available thereby leading to significant savings in computation time. Furthermore, each simulation of the fiber model using the analytically integrated stresses (Eqns. 5.5–5.7) was found to be about 200 times faster than using numerical integration of stresses from population of fibers (Eqn. 5.4).

We detail the procedure for obtaining the parameters by nonlinear regression applied to biaxial test data. Prior to testing, the sample is preconditioned with multiple

cycles of equibiaxial stretch with the same extension ratio used in the test. The applied stretch is large enough so that nonlinearity in the load response is visible without causing damage to the tissue. The optimization function Φ for nonlinear regression is set as the L^2 norm of the error between grip force computed by the simulation $F^{(g)}$ and the corresponding measurement $\bar{F}^{(g)}$ from load data:

$$\Phi = \sum_{i,\,(g)} \left(F_i^{(g)} - \bar{F}_i^{(g)} \right)^2 \tag{5.25}$$

where g is the grip location (e.g., top, right, bottom, left), and i is the step number over which load measurements are available. A multi-test protocol may be used similar to the GAIM protocol shown in Fig. 2.11 in which case we optimize the total error norm over all the n experiments $\left(\Phi^{(1)} + \Phi^{(2)} + \ldots + \Phi^{(n)}\right)$. Partial derivatives of the optimization function Φ with respect to the model parameters are required for the Jacobian of the nonlinear regression. Only the term $F_i^{(g)}$ in Eqn. 5.25 is dependent on the model parameters, and is obtained by integrating the forces in the measured direction along the grip boundary of the finite-element mesh. These forces, in turn, are obtained by numerical integration of the stresses over the element, and hence the following analytical derivatives are required- $\partial S_{ij}/\partial A$, $\partial S_{ij}/\partial B$, $\partial S_{ij}/\partial \kappa$, $\partial S_{ij}/\partial \mu$. Analytical expressions for these derivatives are presented in Appendix A.1 and can be used for computing the Jacobian in a finite-element framework that is coupled to a nonlinear optimization package.

5.3.1 Characterization of Urologic Tissue from Biaxial Experiments

As an example of the application of the model to characterize fibrous tissues from biaxial experiments, we performed tests on a urological tissue sample and fit the model parameters to the loads and displacements recorded at the grips. Quasi-static, biaxial stretch tests on a cruciform shaped sample of fresh cadaveric, bladder wall tissue was performed by holding the four arms with hooks and extending them. The sample was pre-conditioned and equibiaxial stretch of 12% was applied and the forces on the arms were recorded. An image of the sample was recorded at the beginning of the test and the geometry of the sample was meshed. The fiber model parameters were fit to force–displacement data on all arms via nonlinear regression. Figure 5.2

shows the sample (7.21 mm thickness) which was tested, with the mesh overlaid on the image. We assumed that the sample was homogeneous. Displacements applied on the hooks were transferred as boundary conditions to all nodes on the four arms of the cruciform mesh.

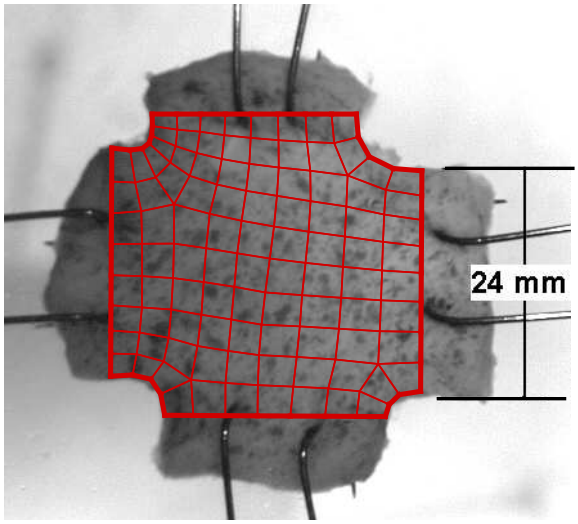

Figure 5.2: Biaxial stretch test of bladder wall sample extended by hooks. A mesh based on the undeformed geometry is used for the simulation. Displacement boundary conditions were applied to all nodes on the four arms.

Nonlinear regression fit of the parameters resulted in estimates of $A = 171$ kPa, $B = 12.6$, $\kappa = 0.24$, $\mu = 95°$. The comparison of force–displacement curves for the data and the simulation using the fitted parameters is shown in Fig. 5.3. The large value of B indicates a high degree of nonlinear behavior. The value of μ indicates that the sample has a preferential orientation that is near vertical, and the small value of κ suggests that there is considerable spread in the distribution around μ.

5.4 Obtaining Model Parameters from GAIM Results

We have shown in the previous section that homogeneous fibrous soft tissues can be represented by the fiber constitutive model based on biaxial experiments where only the boundary forces and displacements are recorded. However, as we have done with biaxial testing in GAIM, samples with visual textures can be strain-tracked and thus one can obtain the strain fields over the entire spatial domain. If heterogeneous

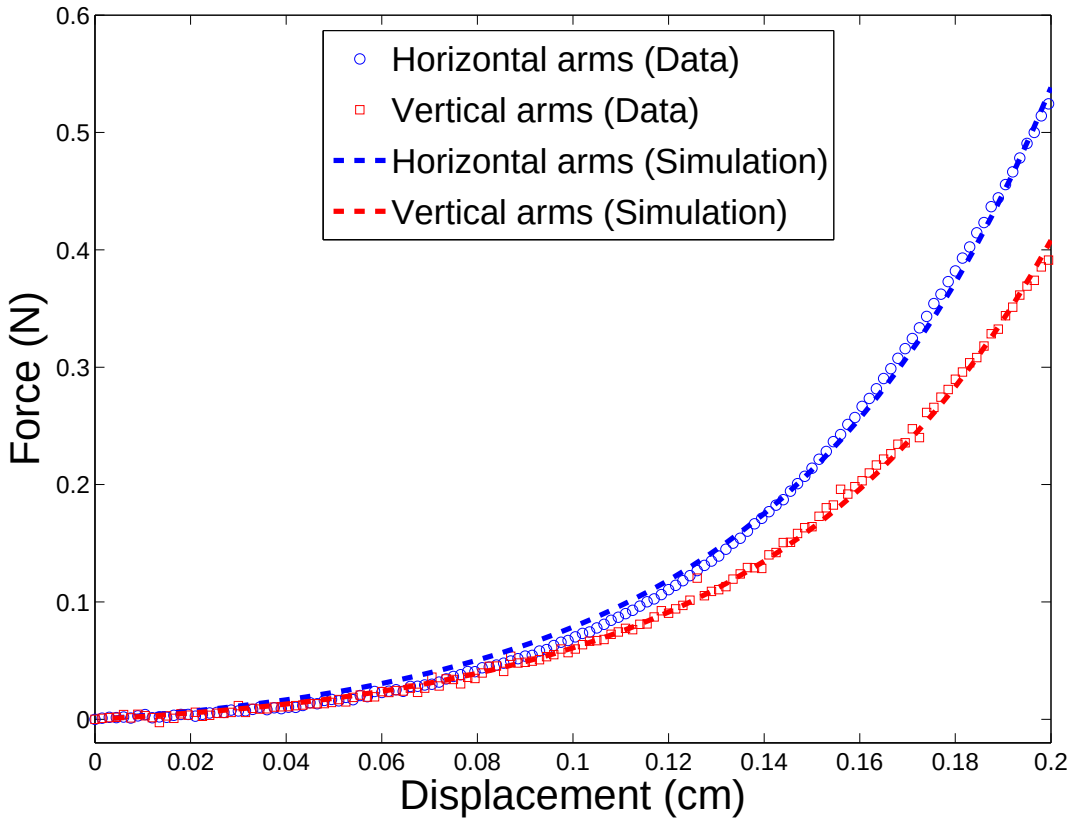

Figure 5.3: Comparison of force–displacement curves of the data and simulation for $A = 171$ kPa, $B = 12.6$, $\kappa = 0.24$, $\mu = 95^\circ$ shows a good fit to the data.

properties are to be determined then we can adopt a two step method: (i) GAIM is used to partition the domain into homogeneous subdomains and evaluate stiffness and anisotropic parameters of each partition, (ii) the output from GAIM is translated to estimate nonlinear model properties for each partition. In this section we demonstrate the use of results from GAIM to obtain fitting parameters for the nonlinear model applied to each partition. For each partition produced by GAIM, the three quantities of anisotropy and stiffness reported by eigentensor analysis of the elastic tensor C are:

- Preferred direction of alignment θ_{GAIM}
- Degree of anisotropy r_{GAIM}
- Kelvin Modulus Λ_{GAIM}

We have previously shown (Fig. 3.6(b)) that the anisotropy vectors of C_{ijkl} correlated well with the vectors from tangent moduli D_{ijkl} of the fiber model. Estimates for the parameters of the fiber model can therefore be made by matching r, θ, Λ obtained from D with those computed from C

$$(r, \theta, \Lambda)_{GAIM} \approx (r, \theta, \Lambda)_{fiber} \tag{5.26}$$

Since the direction of preferred alignment is a symmetry state of both C and D, clearly the two angles must be similar

$$\mu = \theta_{fiber} \approx \theta_{GAIM} \tag{5.27}$$

We employ the analytical expressions for D_{ijkl} to determine the form of r_{fiber} and Λ_{fiber}. In order to simplify the expressions we choose coordinate axes along the preferred direction of alignment so that μ is 0°. Thus matrix D and the converted tensor $\hat{D}$ are

$$D = \begin{bmatrix} D_{1111} & D_{1122} & 0 \\ D_{1122} & D_{2222} & 0 \\ 0 & 0 & D_{1122} \end{bmatrix} \quad \Rightarrow \quad \hat{D} = \begin{bmatrix} D_{1111} & D_{1122} & 0 \\ D_{1122} & D_{2222} & 0 \\ 0 & 0 & 2D_{1122} \end{bmatrix} \tag{5.28}$$

The three Kelvin moduli are evaluated to be

$$\Lambda^{(1)}, \Lambda^{(2)} = \frac{1}{2}\left[D_{1111} + D_{2222} \pm \sqrt{(D_{1111} - D_{2222})^2 + 4D_{1122}^2}\right] \tag{5.29}$$

$$\Lambda^{(3)} = 2D_{1122} \tag{5.30}$$

where $\Lambda^{(1)}$ is largest Kelvin modulus associated with the stretch mode of $\hat{D}$ and hence

$$\Lambda_{fiber} = \Lambda^{(1)} = \frac{1}{2}\left[D_{1111} + D_{2222} + \sqrt{(D_{1111} - D_{2222})^2 + 4D_{1122}^2}\right] \tag{5.31}$$

The corresponding eigenvector is $[\cos\phi, \sin\phi, 0]$ where $\phi = \tan^{-1}\left(\left(\Lambda^{(1)} - D_{1111}\right)/D_{2222}\right)$ and hence the anisotropy value r_{fiber} is obtained from Eqn. 2.30 as

$$r_{fiber} = \frac{|\,1 - |\tan\phi|\,|}{1 + |\tan\phi|} = \frac{\left|\,1 - \left|\frac{\Lambda^{(1)} - D_{1111}}{D_{2222}}\right|\,\right|}{1 + \left|\frac{\Lambda^{(1)} - D_{1111}}{D_{2222}}\right|} \tag{5.32}$$

Since the expressions for D_{ijkl} are a function of strains we first calculate them for the undeformed state. Then D_{1111}, D_{2222} and D_{1122} simplify to

$$D_{1111} = \frac{AB}{2}\left(2 + \frac{I_1(\kappa)}{I_0(\kappa)}\left[2 - \frac{1}{\kappa}\right]\right) \tag{5.33}$$

$$D_{2222} = \frac{AB}{2}\left(2 + \frac{I_1(\kappa)}{I_0(\kappa)}\left[-2 - \frac{1}{\kappa}\right]\right) \tag{5.34}$$

$$D_{1122} = \frac{AB}{2}\left(\frac{I_1(\kappa)}{\kappa I_0(\kappa)}\right) \tag{5.35}$$

Substituting these into Eqns. 5.31, 5.32 we obtain

$$\Lambda_{GAIM} \approx \Lambda_{fiber} = \frac{AB}{2}\left(2 - \frac{I_1(\kappa)}{\kappa I_0(\kappa)} + \frac{I_1(\kappa)}{I_0(\kappa)}\sqrt{4 + 1/\kappa^2}\right) \tag{5.36}$$

$$r_{GAIM} \approx r_{fiber} = \frac{1 + 2\kappa - \sqrt{1 + 4\kappa^2}}{1 - 2\kappa + \sqrt{1 + 4\kappa^2}} \tag{5.37}$$

The remaining two Kelvin moduli are evaluated to be

$$\Lambda^{(2)} = \frac{AB}{2}\left(2 - \frac{I_1(\kappa)}{\kappa I_0(\kappa)} - \frac{I_1(\kappa)}{I_0(\kappa)}\sqrt{4 + 1/\kappa^2}\right) \tag{5.38}$$

$$\Lambda^{(3)} = AB\left(\frac{I_1(\kappa)}{\kappa I_0(\kappa)}\right) \tag{5.39}$$

If the strain state of dilatation is considered (E_{11}=E_{22}=E, and E_{12}=0) then Eqn. 5.37 is unchanged while Eqn. 5.36 is changed by replacing $A \rightarrow Ae^{2BE}$. The value of r_{fiber} is dependent only on κ. Therefore, κ can be estimated directly from r_{GAIM}. Once κ is known, Eqn. 5.36 is used to estimate the coupled term AB.

Figure. 5.4 shows the graphs of both $\frac{\Lambda_{GAIM}}{AB}$ and r_{GAIM} plotted against κ using Eqns. 5.37 and 5.36 respectively. The range of values for r_{GAIM} is within 0 and

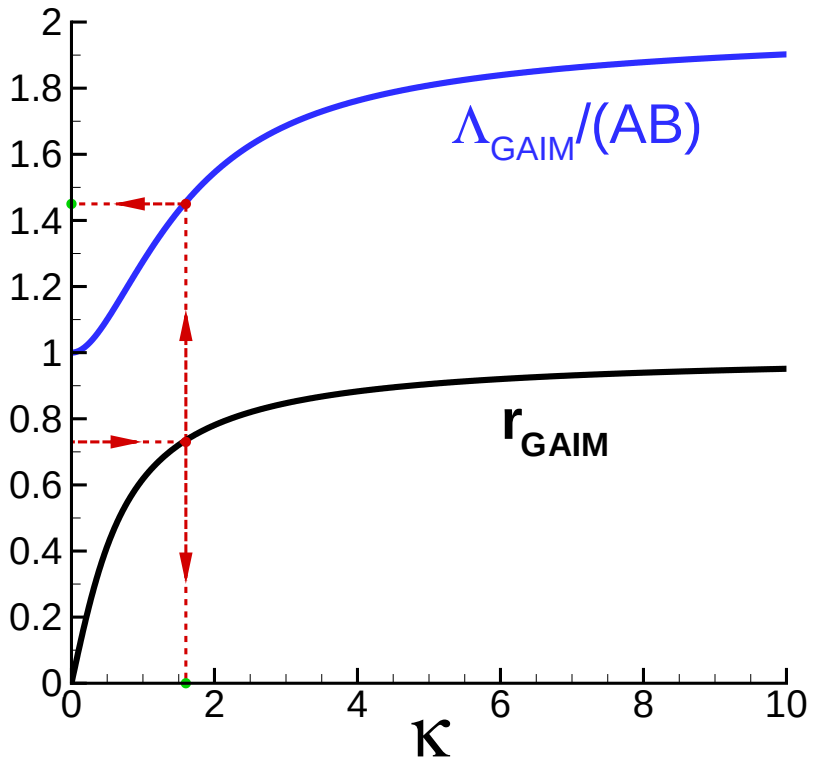

Figure 5.4: Obtaining parameters of fiber model from GAIM results: The curves for r_{GAIM} and $\Lambda_{GAIM}/(AB)$ for all values of κ are bounded within [0,1] and [1,2] respectively. If we obtain the values of $r_{GAIM} = 0.73$ and $\Lambda_{GAIM} = 1504$ kPa from GAIM, then from these graphs $\kappa \approx 1.6$ and $\Lambda_{GAIM}/(AB) \approx 1.45$. This implies that $AB \approx 1037$ kPa.

1, while $\frac{\Lambda_{GAIM}}{AB}$ is within 1 and 2. We illustrate the process of finding fiber parameters from GAIM results obtained for the simulated test in §3.3 where we obtained estimates of r_{GAIM}=0.73 and Λ_{GAIM}=1504 kPa. Using this value of r_{GAIM} on the y-axis, a horizontal line is drawn to the graph of r_{GAIM}. The abscissa of the intersection point is κ=1.6. A vertical line is drawn from this value of κ to the curve of $\frac{\Lambda_{GAIM}}{AB}$ and intersects it at an ordinate value of 1.45. The term AB is then approximated to be 1037 kPa. In comparison to the exact values used for the fiber model (κ=2, A=270 kPa, B=3), these are highly satisfactory. Hence, the knowledge of the triad of values r_{GAIM}, θ_{GAIM}, Λ_{GAIM} allows us to calculate the triad of κ, μ and AB with reasonable accuracy. While both A and B cannot be simultaneously obtained from GAIM, they can be decoupled by fitting the fiber model parameters to the deformation and force data for the full portion of all loading cycles.

Chapter 6

Conclusion and Future Work

In this study we have developed a method that fills a key gap in the modeling of soft tissues whose distinct, complex structure provides them with anisotropic and heterogeneous properties. We developed an inverse mechanics method that handled the combination of anisotropy and heterogeneity in the context of obtaining tissue properties from the common method of biaxial mechanical testing. Spatial heterogeneity was represented by dividing the domain into partitions of homogeneous properties. For each partition, regional anisotropy was determined by using a linear, elastic, anisotropic constitutive model and using the method of eigentensors to extract the major fiber direction and the degree of anisotropy. Reduction of the problem to that of partitioning the domain and determination of linear, anisotropic properties of each partition, resulted in several benefits, chiefly: (i) the linear model led to rapid computation and provided statistical confidence measures for assessing the performance of the model, (ii) anisotropy direction and degree of anisotropy were extracted from the parameters with no *a priori* assumption of orientation.

We validated our method with data from *in silico* and *in vitro* systems. Results from the tests on soft-tissue analogs showed successful identification of regional differences in anisotropy from full-field displacements and boundary forces obtained from multiple biaxial extension tests. Tests on fibroblast-remodeled collagen cruciforms demonstrated the method's success in capturing regional anisotropic changes associated with growth and remodelling. That the method extracted major fiber directions

with reasonable accuracy despite using a linear model, is a significant benefit.

Mechanical testing for GAIM requires a paradigm shift in the design of experiments. While conventional methods for parameter extraction from biaxial tests focus on applying homogeneous strains on the tissue sample and fitting specific constitutive models to the stress–strain measurements, GAIM requires experiments which generate a rich data set of force–strain measurements which improve the sensitivity of the parameters to the imposed deformations. Accordingly, heterogeneous strain fields and asymmetry in sample geometry and loading are preferred.

Some deficiencies in the method were identified, chief of which was the reduced accuracy at the grip boundary due to the unavailability of shear force at the grips. In future, we will employ load cells which report forces and moments about multiple axes. The reliability of the method depends on the success in generating significant strains of shear and stretch over all regions of the sample, and measuring them with good accuracy. Multiple tests with varied stretch ratios and asymmetric sample shapes generate a large range of deformations and the resulting system is solved with all the tests combined in a least-squares sense. Despite multiple tests with asymmetric loading, some portions of the tissue might be under-loaded or have very little shear. In future we will investigate the optimal combination of asymmetric sample shape, introducing offset in the loading axes, and gripping mechanisms that will induce more shear in the sample. It is imperative that samples are speckled well to provide visual texture that can be used by image correlation software to compute strains with good accuracy. That soft tissues need to be tested while immersed in a saline bath (to maintain similarity to their *in vivo* habitat), presents a challenge with the application of visual texture that will be preserved during the course of testing. We have had success in speckling samples with Verhoeff's stain by using an airbrush in addition to flicking a wet paintbrush over the sample. However, during the course of fixing the sample on the grips, there is risk of degrading the quality of texture at some regions. Improvements can be made in the design of better sample speckling methods that will produce good visual texture and contrast which will not degrade when immersed in a saline bath.

A limitation to GAIM is that since the constitutive assumption is linear, the elasticity

tensor C cannot directly characterize fibrous soft tissues which exhibit high nonlinearity. We have developed a closed-form model for fibrous tissues for which results from GAIM can directly be transferred as parametric estimates for each partition. Our future work will be to apply this as a second step in the modeling of anisotropic, heterogeneous tissues.

In summary, this work has built a novel exploratory tool to extract region-specific anisotropic properties on intact tissue samples. The ability to computationally dissect and analyze a tissue can be applied to provide information on the mechanical function of healthy tissue subjected to complex physiologic loads, identify regions within a tissue that exhibit irregular mechanical behavior (possibly due to disease or damage), and provide structural information from the mechanical function of tissues that are not amenable to structural tests.

6.1 Application of GAIM as a Novel Exploratory Tool in Soft Tissue Mechanics

The combination of GAIM and the nonlinear fiber model have opened up research avenues which will use the developed capabilities to further our understanding of tissue mechanics. In this section we describe a couple of the projects that are being pursued.

6.1.1 Mechanical Changes in the Rat Right Ventricle with Decellularization

This work is being prepared as a part of the paper:

Mechanical Changes in the Rat Right Ventricle with Decellularization
(in preparation) *Journal of Biomechanics*, 2011
Witzenburg, C., Raghupathy, R., Kren, S.M., Taylor, D.A., and Barocas, V.H.

Whole-organ decellularization has been established as a potential tool to produce an intact three-dimensional scaffold for bioartificial hearts [8]. In addition, decellularization provides an opportunity to study cardiac wall mechanics in a simplified system. By separating the cells from the matrix, decellularization can allow us to identify the

contribution of each component to the material properties of the myocardial tissue. Separating cell from matrix mechanics could be particularly valuable in the study of localized matrix injury or scarring which occurs in myocardial infarction. Previous studies of healthy and/or infarcted myocardium have involved cutting small samples from the myocardium and assuming homogeneity in tissue properties across each sample [70–73]. The small size of the tissue prevents assessment of heterogeneity by samples drawn from different locations. For example, the right ventricle of the Sprague-Dawley (SD) rat, a popular choice for myocardial decellularization experiments [8], is only about 8 mm across. The small size is however, not a limitation for GAIM since our model provides the capability to analyze intact tissue samples and assess the heterogeneity and regional anistropy.

In an ongoing study, we have used GAIM to compare the mechanical properties of freshly dissected right ventricle and decellularized right ventricle of the SD rat. We tested the hypotheses that decellularized samples have larger stiffness as measured by our method, and that they do not exhibit a change in the degree of anisotropy or heterogeneity.

Four samples ($n = 4$) of right ventricles from decellularized hearts and from cadaveric hearts (control) were tested biaxially on an Instron planar biaxial unit. Figure 6.1(a) shows a decellularized heart and the location from where samples are drawn. The epicardium surfaces were stained to provide visual texture for image correlation. The 15-test GAIM protocol (Fig.2.11) was run with an additional equibiaxial test at the end of the protocol, for verifying that minimal tissue damage occurred during the experiment.

Alignment and stiffness contour maps were generated for all samples. Figure 6.2 shows the results for a representative, decellularized sample. We considered only the central region (marked with a red circle) to avoid the artifacts that arose at the boundaries. The central region was observed to be anisotropic and aligned roughly along the circumferential direction (Fig. 6.2(a)) with little regional variation in angle or degree of anisotropy. Kelvin moduli over this region were within 350–700 kPa.

The mean and standard deviation of three quantities- (i) degree of anisotropy, r_{GAIM}, (ii) preferred direction of alignment, θ_{GAIM}, and (iii) largest Kelvin modulus, Λ_{GAIM},

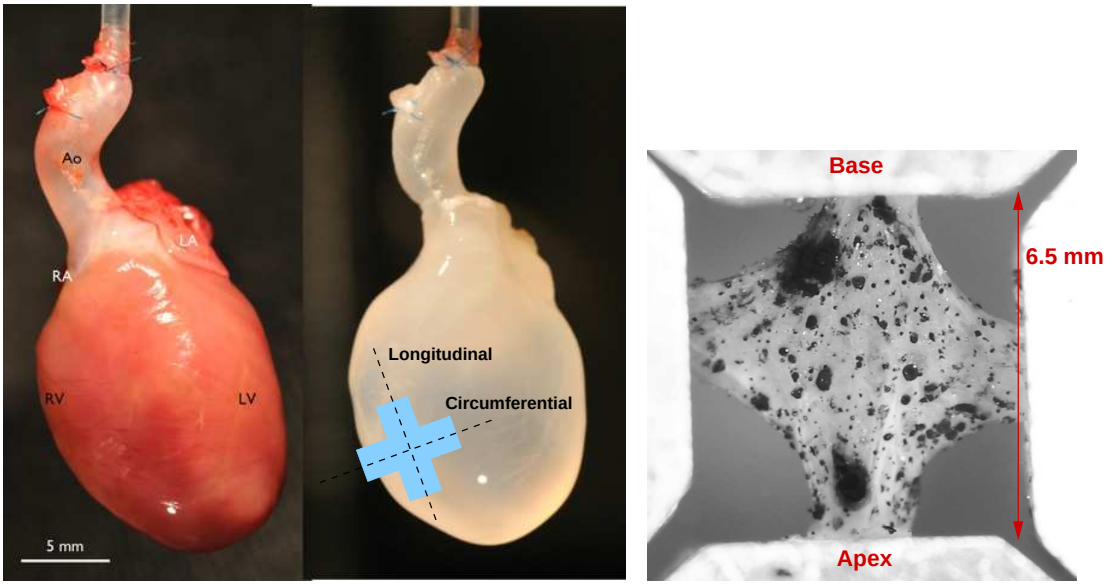

(a) (b)

Figure 6.1: a) Left panel shows the heart during the decellularization process. Labels indicate aorta (Ao), right atrium (RA), left atrium (RA), right ventricle (RV), and left ventricle (LV). The panel on right shows the heart after decellularization is complete, with the cruciform sample geometry overlaid on fully decellularized rat heart showing the circumferential and longitudinal directions. (b) The epicardium surface is stained for visual texture and gripped in an Instron biaxial test unit. The circumferential and longitudinal directions are horizontal and vertical respectively.

were computed for each sample over the central region. Heterogeneity in the center of the sample is quantified by the standard deviate in these results. These results were further averaged over the two types of samples (decellularized and control) to compare their respective mechanical properties and identify changes due to decellularization.

Figure 6.3 shows the comparison of these quantities between decellularized and control samples. No significant difference was found between the two types in the degree of anisotropy (Fig. 6.3(a)), the direction of orientation (Fig. 6.3(b)), and the heterogeneity in both (Figs. 6.3(d),6.3(e)). Decellularized samples had significantly higher stiffness than control (Fig 6.3(c)) but no significant change was found in the heterogeneity in stiffness (Fig 6.3(f)).

It is clear from this study that decellularization is responsible for increased stiffness (by one order of magnitude) of the right ventricle. Thus, the extracellular material

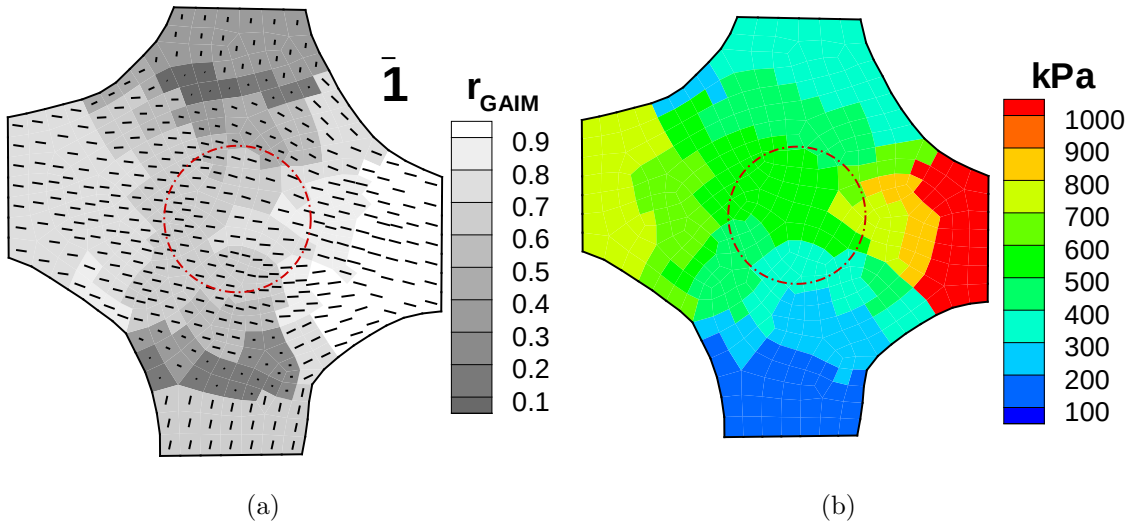

Figure 6.2: Results from a representative decellularized heart sample show (a) Alignment map and, (b) Kelvin moduli. We compared the values of alignment direction θ_{GAIM}, degree of anisotropy r_{GAIM}, and largest Kelvin modulus Λ_{GAIM} over all control and decellularized samples ($n = 4$) for the central region within the red circle.

is the primary determinant of the stiffness of passive myocardial tissue. However, because there was no significant difference in the average normalized standard deviation of the maximum Kelvin modulus there is little evidence to suggest that the decellularization process has an effect on the variability of the stiffness across the central region of the right ventricle. This indicates that the decellularization process does not change the regional differences in stiffness across the right ventricle. There is strong circumferential alignment for all samples, an observation consistent with previous studies [8]. This is expected to hold true for the right ventricle as well, since both have the same general fiber alignment [74]. Our finding that no heterogeneous alignment strength or direction across the central region of the tissue was altered by the decellularization process confirms previous histological results [8] which showed preservation of fiber composition and orientation of the myocardial extracellular matrix post-decellularization.

Large variability among the two types of samples were found for nearly all results. As part of our future work, we will increase the sample size to obtain more reliable statistics. We will also expand our tests to left ventricular samples, which pose a

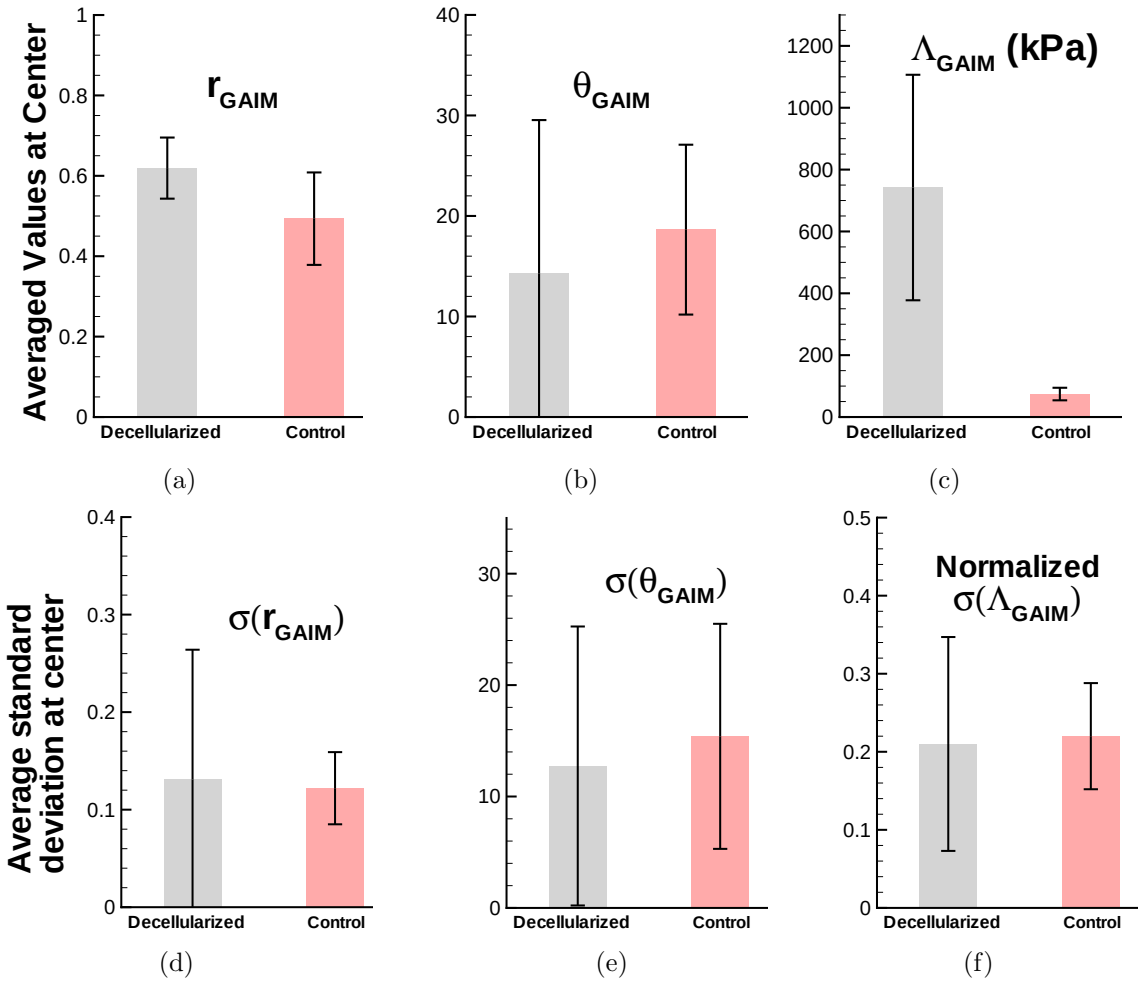

Figure 6.3: Comparison of degree of alignment, r_{GAIM}, preferred directon of alignment, θ_{GAIM}, and largest Kelvin modulus, Λ_{GAIM} between decellularized and control samples. Error bars represent the standard deviation of each quantity over the samples. (a,b,c) are averaged over the sample center, and further averaged over the four samples ($n = 4$) of the same type. (c,d,e) are standard deviations of the quantities over the sample center, averaged over the four samples of the same type. (a) Both decellularized and control have moderately high alignment with no significant difference between each other, (b) No significant difference was found in the preferred orientation between the two. Large error bars show that there was large variation among samples, (c) Decellularized samples had significantly more stiffness than control. Considerable variation in stiffness was present in the former, (d) Minimal heterogeneity was found in both the types which were not significantly different. There was large variability among decellularized samples, (e) Considerable heterogeneity was observed in preferred orientation with large variability among samples of both types which were not significantly different, (f) Heterogeneity in stiffness was not significantly different between the two types. Decellularized samples had large variability.

challenge for biaxial testing because of their high thickness which leads to non-planar deformations. Since left and right ventricles are known to have the same qualitative mechanical behavior, we will use the current results as a starting point towards analysing decellularized left ventricular samples. In particular we want to begin examining the effects of myocardial infarction on the extracellular matrix mechanics. There is disagreement as to the nature of the alignment within the infarct [75]. Also, the alignment within the tissue transiting from the healthy to diseased state has yet to be investigated.

6.1.2 Mechanical Characterization of Annulus Fibrosus of the Intervertebral Disc

The intervertebral disc is a complex tissue with different components that makes its mechanical behavior nonlinear, anisotropic, and viscoelastic. It is composed of a gelatinous core- the nucleus pulposus, and an outer ring- the annulus fibrosus (AF), composed of concentric layers of collagen fibers that are oriented at ± 28–30° to the horizontal plane layers (lamellae). The complex loading environment of the disk comprising of tension, compression, shear, torsion, and bending is supported by the AF.

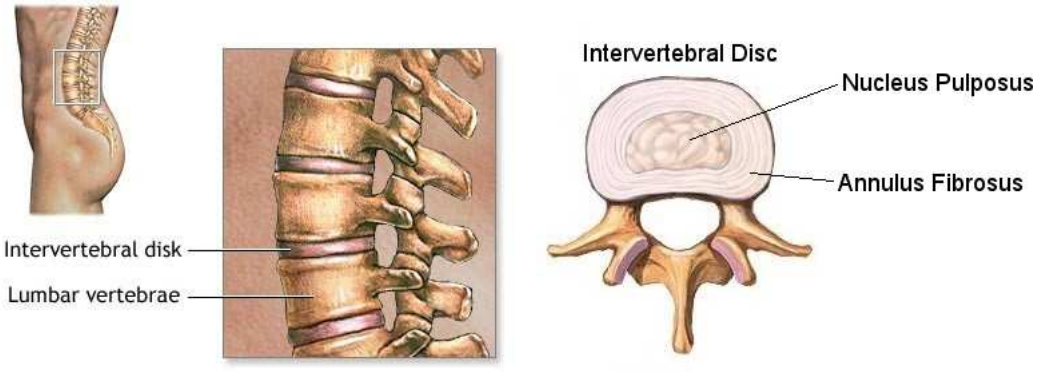

Figure 6.4: Anatomy of the (a) lumbar spine and (b) intervertebral disc showing the annulus fibrosus (AF) and nucleus pulposus regions. A single lamella from AF is dissected and tested biaxially with the vertebral attachments intact. [Image used with permission from A.D.A.M Images]

Few studies have been done to characterize the mechanical behavior of individual AF

lamellae [76,77]. Improved tissue characterization would enable tissue engineering and regenerative therapies to mimic natural disc mechanics. As a preliminary work, we have tested single AF lamellae samples drawn from human, cadaveric intervertebral disc and obtained the load-deformation response from biaxial extension tests. Freshly frozen human cadaveric L1-L2 segments were cut transversely with a bone saw to extract the disc with vertebral attachments above and below. The disc was cut parallel to the frontal plane to excise the most anterior portion of the disc. A rotary tool was used to cut the vertebral attachments along the sagittal plane. The samples were dissected to single lamellae. Figure 6.5 shows a couple of samples that were tested after visual texture was added to aid image correlation.

GAIM analysis on the samples could not be performed as accurate displacement fields over the entire sample could not be obtained. The surfaces of the lamellae have roughness that pose challenges to the image correlation software as new surface textures become visible upon extension, and lead to artificially large computed strains. In place of GAIM, the nonlinear fiber-based model that was presented in §5.2 will be used to characterize the AF tissue by fitting the model parameters (as done in §5.3) to to the applied displacements and measured loads at the grips assuming homogeneous properties of the sample. Since the orientation of each AF layer is known to be about $\pm 30^\circ$, we fit the three parameters A, B and κ to the recorded force-displacement data. Preliminary results of parameters fit and averaged over five samples using only a single equibiaxial protocol resulted in the following estimates and corresponding 95% confidence values: A=98 $\pm$ 51 kPa, B=11 $\pm$ 2.2, κ=1.2 $\pm$ 0.72, with θ taken as 30° as mentioned previously. Large variation in A values suggests that a number of stiffness values fit the data due to specimen health and regional variation. The large B value indicates high degree of nonlinearity. Although the value of κ is large, it is under-predicted since the lamellae have strong alignment with a tight distribution. The large confidence intervals indicate substantial variability in samples. In future we will test a larger sample set with fits obtained from the multiple test protocol, instead of a single equibiaxial test for better accuracy.

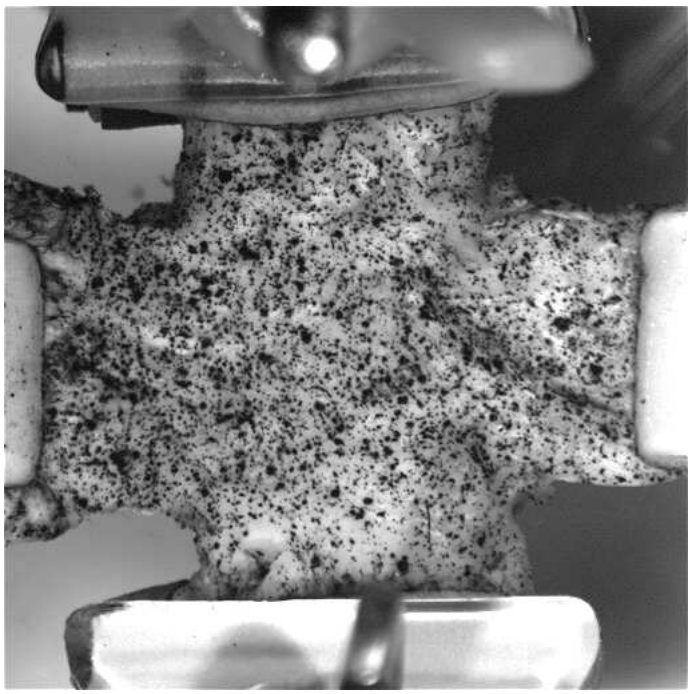

(a)

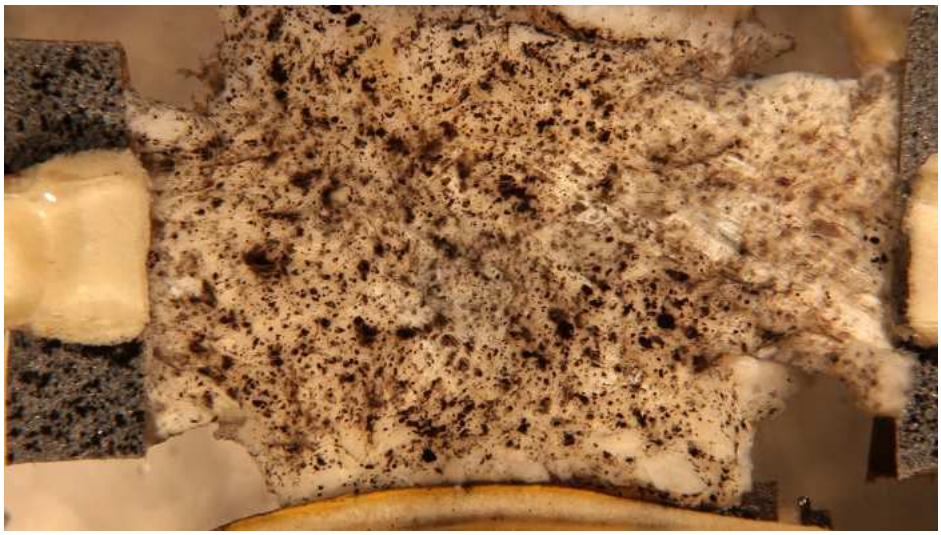

(b)

Figure 6.5: Samples of single lamellae of annulus fibrosus textured with Verhoeff's stain and loaded on the Instron biaxial unit. The circumferential direction is horizontal. The two vertical arms are gripped at the bony attachments. Sandpaper is glued to the sample ends and held in the grips. Surface roughness in the sample presents a challenge to obtain accurate displacement fields by image correlation.

Bibliography

[1] Lake, S. P., Miller, K. S., Elliott, D. M., and Soslowsky, L. J., 2010, "Tensile properties and fiber alignment of human supraspinatus tendon in the transverse direction demonstrate inhomogeneity, nonlinearity, and regional isotropy," Journal of Biomechanics, **43**(4), pp. 727 – 732.

[2] Insana, M. F. and Bamber, J. C., 2000, "Tissue motion and elasticity imaging," Physics in Medicine and Biology, **45**(6), p. 2 p preceding 1409.

[3] Richards, M. S., Barbone, P. E., and Oberai, A. A., 2009, "Quantitative three-dimensional elasticity imaging from quasi-static deformation: a phantom study," Physics in Medicine and Biology, **54**(3), p. 757.

[4] Sander, E. A., Stylianopoulos, T., Tranquillo, R. T., and Barocas, V. H., 2009, "Image-based multiscale modeling predicts tissue-level and network-level fiber reorganization in stretched cell-compacted collagen gels," Proceedings of the National Academy of Sciences of the United States of America, **106**(42), pp. 17675–17680.

[5] Stella, J. A. and Sacks, M. S., 2007, "On the Biaxial Mechanical Properties of the Layers of the Aortic Valve Leaflet," Journal of Biomechanical Engineering, **129**(5), pp. 757–766.

[6] Doehring, T. C., Kahelin, M., and Vesely, I., 2005, "Mesostructures of the aortic valve," The Journal of heart valve disease, **14**(5), pp. 679–686.

[7] Quinn, K. P. and Winkelstein, B. A., 2008, "Altered Collagen Fiber Kinematics Define the Onset of Localized Ligament Damage During Loading," Journal of Applied Physiology, **105**(6), pp. 1881–1888.

[8] Ott, H. C., Matthiesen, T. S., Goh, S.-K., Black, L. D., Kren, S. M., Netoff, T. I., and Taylor, D. A., 2008, "Perfusion-decellularized matrix: using nature's platform to engineer a bioartificial heart," Nature Medicine, **14**(2), pp. 213–221.

[9] Bertero, M. and Boccacci, P., 1998, *Introduction to Inverse Problems in Imaging*, IOP Publishing, Bristol.

[10] Aster, R., Borchers, B., and Thurber, C., 2005, *Parameter Estimation and Inverse Problems*, Academic Press, har/cdr ed.

[11] Greenleaf, J. F., Fatemi, M., and Insana, M., 2003, "Selected Methods for Imaging Elastic Properties of Biological Tissues," Annual Review of Biomedical Engineering, **5**, pp. 57–78.

[12] Dresner, M. A., Rose, G. H., Rossman, P. J., Muthupillai, R., Manduca, A., and Ehman, R. L., 2001, "Magnetic Resonance Elastography of Skeletal Muscle," Journal of magnetic resonance imaging : JMRI, **13**(2), pp. 269–276.

[13] Muthupillai, R., Lomas, D. J., Rossman, P. J., Greenleaf, J. F., Manduca, A., and Ehman, R. L., 1995, "Magnetic Resonance Elastography by Direct Visualization of Propagating Acoustic Strain Waves," Science (New York, N.Y.), **269**(5232), pp. 1854–1857.

[14] Rogowska, J., Patel, N., Plummer, S., and Brezinski, M. E., 2006, "Quantitative Optical Coherence Tomographic Elastography: Method for Assessing Arterial Mechanical Properties," The British Journal of Radiology, **79**(945), pp. 707–711.

[15] Ophir, J., Cespedes, I., Ponnekanti, H., Yazdi, Y., and Li, X., 1991, "Elastography: a Quantitative Method for Imaging the Elasticity of Biological Tissues," Ultrasonic imaging, **13**(2), pp. 111–134.

[16] Doyley, M. M., Meaney, P. M., and Bamber, J. C., 2000, "Evaluation of an Iterative Reconstruction Method for Quantitative Elastography," Physics in Medicine and Biology, **45**(6), pp. 1521–1540.

[17] Sinkus, R., Lorenzen, J., Schrader, D., Lorenzen, M., Dargatz, M., and Holz, D., 2000, "High-Resolution Tensor MR Elastography for Breast Tumour Detection," Physics in Medicine and Biology, **45**(6), pp. 1649–1664.

[18] Houten, E. E. V., Miga, M. I., Weaver, J. B., Kennedy, F. E., and Paulsen, K. D., 2001, "Three-Dimensional Subzone-Based Reconstruction Algorithm for MR Elastography," Magnetic Resonance in Medicine, **45**(5), pp. 827–837.

[19] Iding, R. H., Pister, K. S., and Taylor, R. L., 1974, "Identification of Nonlinear Elastic Solids by a Finite Element Method," Computer Methods in Applied Mechanics and Engineering,, **4**(2), pp. 121–142.

[20] Kavanagh, K. T. and Clough, R. W., 1971, "Finite Element Applications in the Characterization of Elastic Solids," International Journal of Solids and Structures,, **7**(1), pp. 11–23.

[21] Lei, F. and Szeri, A. Z., 2007, "Inverse Analysis of Constitutive Models: Biological Soft Tissues," Journal of Biomechanics, **40**(4), pp. 936–940.

[22] Promma, N., Raka, B., Grdiac, M., Toussaint, E., Cam, J. B. L., Balandraud, X., and Hild, F., 2009, "Application of the Virtual Fields Method to Mechanical Characterization of Elastomeric Materials," International Journal of Solids and Structures, **46**(3-4), pp. 698–715.

[23] Liu, Y., Sun, L. Z., and Wang, G., 2005, "Tomography-Based 3-D Anisotropic Elastography Using Boundary Measurements," IEEE Transactions on Medical Imaging, **24**(10), pp. 1323–1333.

[24] Sinkus, R., Tanter, M., Catheline, S., Lorenzen, J., Kuhl, C., Sondermann, E., and Fink, M., 2005, "Imaging Anisotropic and Viscous Properties of Breast Tissue by Magnetic Resonance-Elastography," Magnetic Resonance in Medicine, **53**(2), pp. 372–387.

[25] Park, E. and Maniatty, A. M., 2006, "Shear Modulus Reconstruction in Dynamic Elastography: Time Harmonic Case," Physics in Medicine and Biology, **51**(15), pp. 3697–3721.

[26] Chen, Q., Ringleb, S. I., Manduca, A., Ehman, R. L., and An, K. N., 2005, "A Finite Element Model for Analyzing Shear Wave Propagation Observed in Magnetic Resonance Elastography," Journal of Biomechanics, **38**(11), pp. 2198–2203.

[27] Doyley, M. M., Houten, E. E. V., Weaver, J. B., Poplack, S., Duncan, L., Kennedy, F., and Paulsen, K. D., 2004, "Shear Modulus Estimation Using Parallelized Partial Volumetric Reconstruction," IEEE Transactions on Medical Imaging, **23**(11), pp. 1404–1416.

[28] Seshaiyer, P. and Humphrey, J. D., 2003, "A Sub-Domain Inverse Finite Element Characterization of Hyperelastic Membranes Including Soft Tissues," Journal of Biomechanical Engineering, **125**(3), pp. 363–371.

[29] Barbone, P. E. and Bamber, J. C., 2002, "Quantitative Elasticity Imaging: What Can and Cannot be Inferred From Strain Images," Physics in Medicine and Biology, **47**(12), pp. 2147–2164.

[30] Barbone, P. E. and Gokhale, N. H., 2004, "Elastic Modulus Imaging: on the Uniqueness and Nonuniqueness of the Elastography Inverse Problem in Two Dimensions," Inverse Problems, **20**(1), pp. 283–296.

[31] Barbone, P. E. and Oberai, A. A., 2007, "Elastic Modulus Imaging: Some Exact Solutions of the Compressible Elastography Inverse Problem," Physics in Medicine and Biology, **52**(6), pp. 1577–1593.

[32] Avril, S., Bonnet, M., Bretelle, A.-S., Grediac, M., Hild, F., Ienny, P., Latourte, F., Lemosse, D., Pagano, S., Pagnacco, E., and Pierron, F., 2008, "Overview of Identification Methods of Mechanical Parameters Based on Full-Field Measurements," Experimental Mechanics, **48**(4), pp. 381–402.

[33] Bonnet, M. and Constantinescu, A., 2005, "Inverse Problems in Elasticity," Inverse Problems, **21**(2), pp. R1–R50.

[34] Cox, S. J. and Gockenbach, M., 1997, "Recovering Planar Lame Moduli from a Single-Traction Experiment," Mathematics and Mechanics of Solids, **2**(3), pp. 297–306.

[35] Flynn, D. M., Peura, G. D., Grigg, P., and Hoffman, A. H., 1998, "A Finite Element Based Method to Determine the Properties of Planar Soft Tissue," Journal of Biomechanical Engineering, **120**(2), pp. 202–210.

[36] Pedrigi, R. M., David, G., Dziezyc, J., and Humphrey, J. D., 2007, "Regional Mechanical Properties and Stress Analysis of the Human Anterior Lens Capsule," Vision Research, **47**(13), pp. 1781–1789.

[37] Girard, M. J., Downs, J. C., Bottlang, M., Burgoyne, C. F., and Suh, J. K., 2009, "Peripapillary and Posterior Scleral Mechanics–Part II: Experimental and Inverse Finite Element Characterization," Journal of Biomechanical Engineering, **131**(5), p. 051012.

[38] Zhu, Y., Hall, T. J., and Jiang, J., 2003, "A Finite-Element Approach for Young's Modulus Reconstruction," IEEE Transactions on Medical Imaging, **22**(7), pp. 890–901.

[39] Houten, E. E. V., Paulsen, K. D., Miga, M. I., Kennedy, F. E., and Weaver, J. B., 1999, "An overlapping subzone technique for MR-based elastic property reconstruction," Magnetic Resonance in Medicine, **42**(4), pp. 779–786.

[40] Oberai, A. A., Gokhale, N. H., Doyley, M. M., and Bamber, J. C., 2004, "Evaluation of the Adjoint Equation Based Algorithm for Elasticity Imaging," Physics in Medicine and Biology, **49**(13), pp. 2955–2974.

[41] Vogel, C. R., 2002, *Computational Methods for Inverse Problems*, Society for Industrial and Applied Mathematics, Philadelphia.

[42] Sun, W. and Sacks, M. S., 2005, "Finite Element Implementation of a Generalized Fung-Elastic Constitutive Model for Planar Soft Tissues," Biomechanics and Modeling in Mechanobiology, **4**(2-3), pp. 190–199.

[43] Hughes, T. J. R., 1987, *The Finite Element Method : Linear Static and Dynamic Finite Element Analysis*, Prentice-Hall, Englewood Cliffs, N.J.

[44] Mehrabadi, M. M. and Cowin, S. C., 1990, "Eigentensors of Linear Anisotropic Elastic Materials," Quarterly Journal of Mechanics and Applied Mathematics, **43**(1), pp. 15–41.

[45] Thomson, W., 1856, "Elements of a Mathematical Theory of Elasticity," Phil. Trans. R. Soc. Lond., **146**, pp. 481–498.

[46] Sun, W., Sacks, M. S., and Scott, M. J., 2005, "Effects of Boundary Conditions on the Estimation of the Planar Biaxial Mechanical Properties of Soft Tissues," Journal of Biomechanical Engineering, **127**(4), pp. 709–715.

[47] Draper, N. R. and Smith, H., 1998, *Applied Regression Analysis*, Wiley, New York.

[48] Fuller, W., 1987, *Measurement Error Models*, Wiley, New York.

[49] Meunier, A., Riot, O., Christel, P., Katz, J. L., and Sedel, L., 1989, "Inhomogeneities in Anisotropic Elastic Constants of Cortical Bone," IEEE Proceedings, Ultrasonics Symposium, **2**, pp. 1015–1018.

[50] Billiar, K. L. and Sacks, M. S., 2000, "Biaxial Mechanical Properties of the Native and Glutaraldehyde-Treated Aortic Valve Cusp: Part II–A Structural Constitutive Model," Journal of Biomechanical Engineering, **122**(4), pp. 327–335.

[51] Raghupathy, R. and Barocas, V. H., 2009, "A Closed-Form Structural Model of Planar Fibrous Tissue Mechanics," Journal of Biomechanics, **42**(10), pp. 1424–1428.

[52] Sander, E., Stylianopoulos, T., Tranquillo, R., and Barocas, V., 2009, "Image-based biomechanics of collagen-based tissue equivalents," IEEE Engineering in Medicine and Biology Magazine, **28**(3), pp. 10–18.

[53] Jhun, C. S., Evans, M. C., Barocas, V. H., and Tranquillo, R. T., 2009, "Planar biaxial mechanical behavior of bioartificial tissues possessing prescribed fiber alignment," Journal of Biomechanical Engineering, **131**(8), p. 081006.

[54] Sander, E. A., Barocas, V. H., and Tranquillo, R. T., 2010, "Initial Fiber Alignment Pattern Alters Extracellular Matrix Synthesis in Fibroblast-Populated Fibrin Gel Cruciforms and Correlates with Predicted Tension," Annals of Biomedical Engineering.

[55] Tower, T. T., Neidert, M. R., and Tranquillo, R. T., 2002, "Fiber alignment imaging during mechanical testing of soft tissues," Annals of Biomedical Engineering, **30**(10), pp. 1221–1233.

[56] Baek, S., Valentin, A., and Humphrey, J. D., 2007, "Biochemomechanics of cerebral vasospasm and its resolution: II. Constitutive relations and model simulations," Annals of Biomedical Engineering, **35**(9), pp. 1498–1509.

[57] Lanir, Y., 1983, "Constitutive equations for fibrous connective tissues," Journal of Biomechanics, **16**(1), pp. 1–12.

[58] Lanir, Y., 1982, "Constitutive equations for fibrous connective tissues," Journal of Biomechanics, **18**(1), p. 1.

[59] Pinsky, P. M., van der Heide, D., and Chernyak, D., 2005, "Computational modeling of mechanical anisotropy in the cornea and sclera," Journal of cataract and refractive surgery, **31**(1), pp. 136–145.

[60] Gasser, T. C., Ogden, R. W., and Holzapfel, G. A., 2006, "Hyperelastic Modelling of Arterial Layers With Distributed Collagen Fibre Orientations," Journal of the Royal Society, Interface / the Royal Society, **3**(6), pp. 15–35.

[61] Sacks, M. S., 2003, "Incorporation of experimentally-derived fiber orientation into a structural constitutive model for planar-collagenous tissues," Journal of Biomechanical Engineering, **125**(2), pp. 280–287.

[62] Wagenseil, J. E. and Okamoto, R. J., 2007, "Modeling cell and matrix anisotropy in fibroblast populated collagen vessels," Biomechanics and modeling in mechanobiology, **6**(3), pp. 151–162.

[63] Driessen, N. J., Mol, A., Bouten, C. V., and Baaijens, F. P., 2007, "Modeling the Mechanics of Tissue-Engineered Human Heart Valve Leaflets," Journal of Biomechanics, **40**(2), pp. 325–334.

[64] Bischoff, J. E., Arruda, E. M., and Grosh, K., 2000, "Finite element modeling of human skin using an isotropic, nonlinear elastic constitutive model," Journal of Biomechanics, **33**(6), pp. 645–652.

[65] Kuhl, E., Garikipati, K., Arruda, E. M., and Grosh, K., 2005, "Remodeling of biological tissue: Mechanically induced reorientation of a transversely isotropic chain network," Journal of the Mechanics and Physics of Solids, **53**(7), pp. 1552–1573.

[66] Bowes, L. E., Jimenez, M. C., Hiester, E. D., Sacks, M. S., Brahmatewari, J., Mertz, P., and Eaglstein, W. H., 1999, "Collagen fiber orientation as quantified by small angle light scattering in wounds treated with transforming growth factor-beta(2) and its neutalizing antibody," Wound Repair and Regeneration, **7**(3), pp. 179–186.

[67] Marquez, J. P., 2006, "Fourier analysis and automated measurement of cell and fiber angular orientation distributions," International Journal of Solids and Structures, **43**, pp. 6413–6423.

[68] Sander, E. A. and Barocas, V. H., 2009, "Comparison of 2D fiber network orientation measurement methods," Journal of biomedical materials research.Part A, **88**(2), pp. 322–331.

[69] Press, W. H., 2002, *Numerical recipes in C++ : the art of scientific computing*, Cambridge University Press, Cambridge, UK ; New York.

[70] Novak, V. P., Yin, F. C., and Humphrey, J. D., 1994, "Regional mechanical properties of passive myocardium," Journal of Biomechanics, **27**(4), pp. 403–412.

[71] Sacks, M. S. and Chuong, C. J., 1993, "Biaxial mechanical properties of passive right ventricular free wall myocardium," Journal of Biomechanical Engineering, **115**(2), pp. 202–205.

[72] Emery, J. L., Omens, J. H., and McCulloch, A. D., 1997, "Biaxial mechanics of the passively overstretched left ventricle," The American Journal of Physiology, **272**(5 Pt 2), pp. H2299–305.

[73] Zhang, S., Crow, J. A., Yang, X., Chen, J., Borazjani, A., Mullins, K. B., Chen, W., Cooper, R. C., McLaughlin, R. M., and Liao, J., 2010, "The correlation of 3D DT-MRI fiber disruption with structural and mechanical degeneration in porcine myocardium," Annals of Biomedical Engineering, **38**(10), pp. 3084–3095.

[74] Humphrey, J. D., 2002, *Cardiovascular solid mechanics : cells, tissues, and organs*, Springer, New York.

[75] Chen, J., Song, S. K., Liu, W., McLean, M., Allen, J. S., Tan, J., Wickline, S. A., and Yu, X., 2003, "Remodeling of cardiac fiber structure after infarction in rats quantified with diffusion tensor MRI," American journal of physiology.Heart and circulatory physiology, **285**(3), pp. H946–54.

[76] Bass, E. C., Ashford, F. A., Segal, M. R., and Lotz, J. C., 2004, "Biaxial testing of human annulus fibrosus and its implications for a constitutive formulation," Annals of Biomedical Engineering, **32**(9), pp. 1231–1242.

[77] O'Connell, G. D., Guerin, H. L., and Elliott, D. M., 2009, "Theoretical and Uniaxial Experimental Evaluation of Human Annulus Fibrosus Degeneration," Journal of Biomechanical Engineering, **131**(11), 111007.

[78] Pan, B., Qian, K., Xie, H., and Asundi, A., 2009, "Two-dimensional Digital Image Correlation for In-Plane Displacement and Strain Measurement: A Review," Measurement Science and Technology, **20**.

[79] Sutton, M. A., O., J. J., and Schreier, H. W., 2009, *Image Correlation for Shape, Motion and Deformation Measurements : Basic Concepts, Theory and Applications*, Springer, New York.

[80] Foroosh, H., Zerubia, J., and Berthod, M., 2002, "Extension of Phase Correlation to Subpixel Registration," IEEE Transactions on Image Processing, **11**(3), pp. 188–200.

[81] Bergonnier, S., Hild, F., and Roux, S., 2005, "Digital Image Correlation Used for Mechanical Tests on Crimped Glass Wool Samples," Journal of Strain Analysis for Engineering Design, **40**, pp. 185–197(13).

[82] Kelly, D. J., Azeloglu, E. U., Kochupura, P. V., Sharma, G. S., and Gaudette, G. R., 2007, "Accuracy and Reproducibility of a Subpixel Extended Phase Correlation Method to Determine Micron Level Displacements in the Heart," Medical Engineering and Physics, **29**(1), pp. 154–162.

[83] Bing, P., Hui-min, X., Bo-qin, X., and Fu-long, D., 2006, "Performance of Sub-Pixel Registration Algorithms in Digital Image Correlation," Measurement Science and Technology, **17**(6), pp. 1615–1621.

[84] Pan, B., Asundi, A., Xie, H., and Gao, J., 2009, "Digital image correlation using iterative least squares and pointwise least squares for displacement field and strain field measurements," Optics and Lasers in Engineering, **47**(7-8), pp. 865 – 874.

Appendix A

A.1 Analytical Derivatives of Second Piola-Kirchoff Stress of Nonlinear Fiber-Based Model

We present the final results for partial derivatives of the 2nd Piola Kirchoff stress S_{ij} in the nonlinear fiber-based model of §5.2 with respect to the model parameters A, B, κ and μ. For simplicity, we first present the derivatives of γ and δ.

$$\begin{aligned}
\partial\gamma/\partial B &= \beta\cos 2(\delta-\alpha) && \text{(A.1)}\\
\partial\delta/\partial B &= \tfrac{\beta}{2\gamma}\sin 2(\alpha-\delta) && \text{(A.2)}\\
\partial\gamma/\partial\kappa &= \cos 2(\delta-\mu) && \text{(A.3)}\\
\partial\delta/\partial\kappa &= \tfrac{1}{2\gamma}\sin 2(\mu-\delta) && \text{(A.4)}\\
\partial\gamma/\partial\mu &= 2\kappa\sin 2(\delta-\mu) && \text{(A.5)}\\
\partial\delta/\partial\mu &= \tfrac{\kappa}{\gamma}\cos 2(\delta-\mu) && \text{(A.6)}\\
\partial k_0/\partial B &= k_0(C_1+C_2-2)/2 && \text{(A.7)}
\end{aligned}$$

The derivatives $\partial S_{ij}/\partial A$, $\partial S_{ij}/\partial B$, $\partial S_{ij}/\partial\kappa$, $\partial S_{ij}/\partial\mu$ are:

$$\begin{aligned}
\partial S_{11}/\partial A &= \tfrac{1}{2I_0(\kappa)}\left(\tfrac{k_0}{A}\left(I_0(\gamma)+I_1(\gamma)\cos 2\delta\right)-I_1(\kappa)\cos 2\mu\right)-\tfrac{1}{2} && \text{(A.8)}\\
\partial S_{22}/\partial A &= \tfrac{1}{2I_0(\kappa)}\left(\tfrac{k_0}{A}\left(I_0(\gamma)-I_1(\gamma)\cos 2\delta\right)+I_1(\kappa)\cos 2\mu\right)-\tfrac{1}{2} && \text{(A.9)}\\
\partial S_{12}/\partial A &= \tfrac{1}{2I_0(\kappa)}\left(\tfrac{k_0}{A}I_1(\gamma)\sin 2\delta-I_1(\kappa)\sin 2\mu\right) && \text{(A.10)}
\end{aligned}$$

$$\begin{aligned}
\partial S_{11}/\partial B &= \tfrac{1}{2I_0(\kappa)}\left\{\tfrac{\partial k_0}{\partial B}\left(I_0(\gamma)+I_1(\gamma)\cos 2\delta\right)+k_0 I_1(\gamma)\frac{\partial \gamma}{\partial B}\right. \\
&\quad \left.+\,k_0\frac{\partial \gamma}{\partial B}\cos 2\delta\left[I_0(\gamma)-\tfrac{I_1(\gamma)}{\gamma}\right]-2k_0 I_1(\gamma)\frac{\partial \delta}{\partial B}\sin 2\delta\right\} \qquad \text{(A.11)} \\
\partial S_{22}/\partial B &= \tfrac{1}{2I_0(\kappa)}\left\{\tfrac{\partial k_0}{\partial B}\left(I_0(\gamma)-I_1(\gamma)\cos 2\delta\right)+k_0 I_1(\gamma)\frac{\partial \gamma}{\partial B}\right. \\
&\quad \left.-\,k_0\frac{\partial \gamma}{\partial B}\cos 2\delta\left[I_0(\gamma)-\tfrac{I_1(\gamma)}{\gamma}\right]+2k_0 I_1(\gamma)\frac{\partial \delta}{\partial B}\sin 2\delta\right\} \qquad \text{(A.12)} \\
\partial S_{12}/\partial B &= \tfrac{1}{2I_0(\kappa)}\left\{\tfrac{\partial k_0}{\partial B}I_1(\gamma)\sin 2\delta+2k_0 I_1(\gamma)\frac{\partial \delta}{\partial B}\cos 2\delta\right. \\
&\quad \left.+\,k_0\frac{\partial \gamma}{\partial B}\sin 2\delta\left[I_0(\gamma)-\tfrac{I_1(\gamma)}{\gamma}\right]\right\} \qquad \text{(A.13)}
\end{aligned}$$

$$\begin{aligned}
\partial S_{11}/\partial \kappa &= \tfrac{1}{2I_0(\kappa)}\left\{k_0 I_1(\gamma)\frac{\partial \gamma}{\partial \kappa}+k_0\frac{\partial \gamma}{\partial \kappa}\cos 2\delta\left[I_0(\gamma)-\tfrac{I_1(\gamma)}{\gamma}\right]\right. \\
&\quad \left.-2k_0 I_1(\gamma)\frac{\partial \delta}{\partial \kappa}\sin 2\delta-A\cos 2\mu\left[I_0(\kappa)-\tfrac{I_1(\kappa)}{\kappa}\right]\right\} \\
&\quad -\tfrac{I_1(\kappa)}{2I_0(\kappa)}\left\{k_0\left(I_0(\gamma)+I_1(\gamma)\cos 2\delta\right)-AI_1(\kappa)\cos 2\mu\right\} \qquad \text{(A.14)} \\
\partial S_{22}/\partial \kappa &= \tfrac{1}{2I_0(\kappa)}\left\{k_0 I_1(\gamma)\frac{\partial \gamma}{\partial \kappa}-k_0\frac{\partial \gamma}{\partial \kappa}\cos 2\delta\left[I_0(\gamma)-\tfrac{I_1(\gamma)}{\gamma}\right]\right. \\
&\quad \left.+2k_0 I_1(\gamma)\frac{\partial \delta}{\partial \kappa}\sin 2\delta+A\cos 2\mu\left[I_0(\kappa)-\tfrac{I_1(\kappa)}{\kappa}\right]\right\} \\
&\quad -\tfrac{I_1(\kappa)}{2I_0(\kappa)}\left\{k_0\left(I_0(\gamma)+I_1(\gamma)\cos 2\delta\right)+AI_1(\kappa)\cos 2\mu\right\} \qquad \text{(A.15)} \\
\partial S_{12}/\partial \kappa &= \tfrac{1}{2I_0(\kappa)}\left\{k_0\frac{\partial \gamma}{\partial \kappa}\sin 2\delta\left[I_0(\gamma)-\tfrac{I_1(\gamma)}{\gamma}\right]+2k_0 I_1(\gamma)\frac{\partial \delta}{\partial \kappa}\cos 2\delta\right. \\
&\quad \left.-A\sin 2\mu\left[I_0(\kappa)-\tfrac{I_1(\kappa)}{\kappa}\right]\right\} \\
&\quad -\tfrac{I_1(\kappa)}{2I_0(\kappa)}\left\{k_0 I_1(\gamma)\sin 2\delta-AI_1(\kappa)\sin 2\mu\right\} \qquad \text{(A.16)}
\end{aligned}$$

$$\partial S_{11}/\partial\mu = \frac{1}{2I_0(\kappa)}\left\{k_0 I_1(\gamma)\frac{\partial\gamma}{\partial\mu} + k_0\frac{\partial\gamma}{\partial\mu}\cos 2\delta\left[I_0(\gamma) - \frac{I_1(\gamma)}{\gamma}\right]\right.$$
$$\left. -2k_0 I_1(\gamma)\frac{\partial\delta}{\partial\mu}\sin 2\delta + 2AI_1(\kappa)\sin 2\mu\right\} \quad \text{(A.17)}$$

$$\partial S_{22}/\partial\mu = \frac{1}{2I_0(\kappa)}\left\{k_0 I_1(\gamma)\frac{\partial\gamma}{\partial\mu} - k_0\frac{\partial\gamma}{\partial\mu}\cos 2\delta\left[I_0(\gamma) - \frac{I_1(\gamma)}{\gamma}\right]\right.$$
$$\left. +2k_0 I_1(\gamma)\frac{\partial\delta}{\partial\mu}\sin 2\delta - 2AI_1(\kappa)\sin 2\mu\right\} \quad \text{(A.18)}$$

$$\partial S_{12}/\partial\mu = \frac{1}{2I_0(\kappa)}\left\{k_0\frac{\partial\gamma}{\partial\mu}\sin 2\delta\left[I_0(\gamma) - \frac{I_1(\gamma)}{\gamma}\right] + 2k_0 I_1(\gamma)\frac{\partial\delta}{\partial\mu}\cos 2\delta - 2AI_1(\kappa)\cos 2\mu\right\} \quad \text{(A.19)}$$